# Analysis and Development of a Three Body Heaving Wave Energy Converter

by

**Scott J. Beatty**

BASc, University of British Columbia, 2003

A thesis Submitted in Partial Fulfillment of the
Requirements for the Degree of

**Master of Applied Science**

in the Department of Mechanical Engineering



University of Victoria

**Analysis and Development of a Three Body Heaving Wave Energy Converter**

by

**Scott J. Beatty**

BASc, University of British Columbia, 2003

## Supervisory Committee

---

Dr. B. Buckham, Supervisor (Department of Mechanical Engineering)

---

Dr. P. Wild, Supervisor (Department of Mechanical Engineering)

---

Dr. C. Crawford, Departmental Member (Department of Mechanical Engineering)

---

Dr. Rolf Lueck, Outside Member (School of Earth and Ocean Sciences)

**Supervisory Committee**

---

Dr. B. Buckham, Supervisor (Department of Mechanical Engineering)

---

Dr. P. Wild, Supervisor (Department of Mechanical Engineering)

---

Dr. C. Crawford, Departmental Member (Department of Mechanical Engineering)

---

Dr. Rolf Lueck, Outside Member (School of Earth and Ocean Sciences)

## Abstract

A relative motion based heaving point absorber wave energy converter is being co-developed by researchers at the University of Victoria and SyncWave Systems Inc. To that end—this thesis represents a multi-faceted contribution to the development effort. A small scale two-body prototype wave energy converter was developed and tested in a wave tank. Although experimental problems were encountered, the results compare reasonably well to the output of a two degree of freedom linear dynamics model in the frequency domain.

A two-body wave energy converter design is parameterized as a basis for an optimization and sensitivity study undertaken to illustrate the potential benefits of frequency response tuning. Further, a mechanical system concept for frequency response tuning is presented. The two degree of freedom model is expanded to three degrees of freedom to account for the tuning system. An optimization procedure, utilizing a Sequential Quadratic Programming algorithm, is developed to establish control schedules to maximize power capture as a function of the control variables. A spectral approach is developed to estimate WEC power capture in irregular waves.

Finally, as a case study, the modeling, optimization, and spectral methods are applied to

predict performance for a large scale wave energy converter deployed offshore of a remote Alaskan island. Using archived sea-state data and community electrical load profiles, a wave/diesel hybrid integration with the remote Alaskan community power system is assessed to be technologically feasible.

# Table of Contents

# List of Figures

# Nomenclature

| | |
|---|---|
| $A$ | wave amplitude |
| $A$ | wave amplitude |
| $F_b$ | hydrostatic buoyancy force on floating body $j$ |
| $H$ | regular wave height $H = 2A$ |
| $H(\omega_i)_{1/2}$ | float-spar relative displacement transfer function |
| $H_s$ | significant wave height |
| $H_{\text{design}}$ | WEC design wave height |
| $H_{dir}$ | peak wave direction |
| $J$ | rotational inertia of the frequency response control system |
| $N$ | number of components of the discretized spectrum |
| $\bar{P}$ | mean power capture in irregular waves |
| $P(\omega)$ | WEC power capture in the frequency domain |
| $P_{\text{elec}}(t)$ | electrical power output from the DC power take off generator |
| $P_{\text{mech}}(t)$ | instantaneous generator shaft power |
| $R$ | parametric spar bulb radius |
| $R_{\text{ext}}$ | electrical resistance of the external power take off circuit |
| $S(\omega)$ | wave spectral density |
| $T_j$ | draft (depth of submergence) of body $j$ |
| $T_p$ | peak period |
| $V$ | voltage drop over $R_{\text{ext}}$ |
| $V_j$ | displaced volume of body $j$ |
| $\eta$ | water surface elevation with respect to the mean water level |
| $\hat{a}_{0j}$ | complex amplitude of fluid acceleration at depth $z_{Pj}$ |

| | |
|---|---|
| $\hat{v}_{0j}$ | complex amplitude of fluid velocity at depth $z_{Pj}$ |
| $\lambda$ | wavelength |
| $\mu$ | heave added mass coefficient of body $j$ |
| $\omega$ | wave frequency |
| $\omega_i$ | frequency component $i$ of the discretized spectrum |
| $\omega_j$ | undamped natural frequency of a floating body $j$ |
| $\omega_p$ | peak frequency |
| $\phi$ | angular displacement of rotational system |
| $\rho$ | mass density of water $\approx 1020$ [kg/m$^3$] |
| $\tau(t)$ | instantaneous torque on the power take off generator shaft |
| $\theta$ | direction of wave propagation from the $x$ axis |
| $\dot{\theta}_{\text{gen}}(t)$ | instantaneous rotational speed of the power take off generator shaft |
| $\varepsilon$ | phase constant in wave equation |
| $\hat{\xi}_j$ | complex amplitude of displacement of body $j$ |
| $\xi_j(t)$ | displacement of body $j$ |
| $\hat{\xi}_{1/2}$ | complex amplitude of the float relative to the spar |
| $\xi_{1/2}(t)$ | displacement of the float relative to the spar |
| $a$ | radius of the body parallel to wave propagation |
| $\hat{a}(z)$ | complex amplitude of water particle acceleration at $(x, y) = (0, 0)$ |
| $a(z, t)$ | water particle acceleration at $(x, y) = (0, 0)$ |
| $a_1, a_2, a_3$ | geometric constraint parameters |
| $c_g^*(\omega)$ | optimal generator damping coefficient in the frequency domain |
| $c_j$ | damping coefficient of body $j$ |
| $c_g$ | generator damping coefficient |
| $c_{loss}$ | power take–off losses damping coefficient |
| $\hat{f}_{e,j}$ | complex amplitude of wave excitation force on body $j$ |
| $f_{e,j}(t)$ | wave excitation force on body $j$ |
| $g$ | acceleration due to gravity |
| $h$ | water depth |

| | |
|---|---|
| $h$ | water depth |
| $i$ | imaginary number |
| $i$ | imaginary number |
| $j$ | index of the $j$th floating body |
| $k$ | wave number |
| $k_j$ | hydrostatic stiffness of body $j$ |
| $l$ | ballscrew lead in meters translation per radian rotation |
| $l_{\text{jacket}}$ | parametric spar jacket length |
| $m_4$ | inertial control parameter |
| $m_4^*(\omega)$ | optimal inertial control parameter in the frequency domain |
| $m_j$ | mass of body $j$ |
| $m_{23}$ | combined spar and tuning system mass |
| $r_j$ | water-plane radius of floating body $j$ |
| $t$ | time |
| $\hat{v}(z)$ | complex amplitude of water particle velocity at $(x, y) = (0, 0)$ |
| $v(z, t)$ | water particle velocity at $(x, y) = (0, 0)$ |
| $x, y, z$ | Cartesian axes. $z$ is zero at mean water level, positive upward |
| $z_{Pj}$ | reference depth for body$j$ |
| DOF | degree of freedom |
| NIMBY | "not in my backyard" |
| OTD | over-topping device |
| OWC | oscillating water column |
| PTO | power take-off |
| WAB | wave activated body |
| WEC | wave energy converter |

## Acknowledgements

There are many whom have made this research an incredible experience. Dr. Brad Buckham, a gifted teacher, I thank for his patience and confidence when pushing me into unfamiliar theoretical directions. Dr. Peter Wild has been an ideal mentor who leads by example. Having worked very closely with Nigel Protter, Jim Adamson, Ryan Nicoll and the SyncWave team throughout this research—I thank them not only for their support but also for making the work exciting. Clayton Hiles, I thank for his tireless and enthusiastic contributions, undertaken with eternal pragmatism. As for Jon Zand, I have appreciated his healthy skepticism and sense of humour. Above all, I thank my family and friends for their unconditional support.

*to Shentae*

## Chapter 1

# Introduction

Ocean surface gravity waves, generated by the transfer of wind energy to the ocean surface, are a vast source of clean and renewable energy. The total wave power incident on all of the world's coastlines has been estimated to be 10 TW, the same order of magnitude as the world's total current power demand [1]. As wind energy is transferred to wave energy, the energy density improves. The spatial concentration increases from an average wind power intensity of 0.5 kW per square meter of area perpendicular to the wind direction, at a height of 20 meters above the sea surface, to an average of 2-3 kW per square meter perpendicular to direction of wave propagation just below the sea surface [1].

Canada's average incident wave power has been estimated at 37,000 MW on the West coast and 146,500 MW on the East coast [2] which cumulatively exceed Canada's current electrical demand. Although the magnitude of the wave power incident on Canada's coasts is impressive, it should be obvious that all of the incident wave power potential cannot be captured. First, an endeavor of such scale would interrupt the extremely important ecological processes near the coasts. Second, because wave energy is a distributed and highly variable renewable energy source and much of Canada's coastlines are uninhabited, the cost of extending electrical grids along all coastlines would be astronomical. However, wave energy conversion—similar to wind energy conversion, can offer an environmentally benign, economical, and immediate solution to electricity generation for many locations.

An increased public awareness of environmental and energy issues has stimulated a world-wide increase in support for the development of renewable energy technologies. As a result, a proliferation of wave energy device developers is occurring globally. However,

immediate public acceptance of wave energy has not occurred because wave energy conversion technology and government policy are relatively immature compared to wind energy parallels, and there are no fully commercialized wave energy devices at this time.

A so-called "design-convergence" has not occurred in the wave energy industry whereas the global wind energy industry is said to have "converged" to the horizontal axis wind turbine design. There are many classes of wave energy converters (WEC's) being developed and tested worldwide, each with specific advantages and disadvantages:

1. Classified by location, WEC's are typically separated into shoreline, near-shore, submerged, and offshore devices. Cable costs and incident wave power intensity are competing economic factors because they both decrease with proximity to shore. Although shoreline devices fit well with breakwater structures, they typically require more structural material than floating devices, due to the impact stresses from breaking waves, and suffer from "not-in-my-back-yard" (NIMBY) issues due to the requirement for particularly unattractive structures in coastal locations. Since the kinetic energy part of the wave power transport decays exponentially with water depth, submerged devices are exposed to less incident wave power, and are expected to suffer from complex deployment and maintenance procedures.

2. Classified by operating principle, WEC's can be separated into oscillating water columns (OWC), over-topping devices (OTD), and wave-activated bodies (WAB). OWC devices are afflicted with thermodynamic losses resulting from the pressurization of air, and noise issues with large air turbines. OTD's offer relatively smooth power output but tend to be extremely large devices that require huge capital investments. WAB's, a category that encompasses a diverse range of devices that operate from single modes or combinations of translational and rotational modes, are typically the most compact and efficient devices [3].

3. Classified according to directional characteristics, WEC's are typically separated into point-absorbers, attenuators, and terminators. Point absorbers, attenuators, and terminators, absorb energy from a single point, from a line parallel with the direction of

wave propagation, and from a line perpendicular to the direction of wave propagation respectively.

The point absorber class of WEC offers a relatively low capital investment and high power capture to mass ratio wave energy conversion solution [3]. The scope of this research is limited to a WEC classified as a near-shore-to-offshore, point absorbing, wave activated body. The relative motion based heaving WEC is being co-developed by researchers at the University of Victoria with SyncWave Systems Inc. The device converts reciprocating motion between vertically oscillating bodies into electrical energy.

Since there are no clearly superior heaving point absorber designs to date, this thesis is motivated by the need to expose a further area of the conceptual design space for heaving point absorber systems to critical study. Whereas other self-reacting designs rely on massive damper plates [4, 5], monolithic reacting body structures [6], or power extraction from an internally supported reaction masses [7,8], this thesis explores the SyncWave WEC concept which employs a streamlined surface-piercing reacting body that is not held fixed, like the other designs, but is a tunable heaving body.

## 1.1 Objectives of this Thesis

The overall objective of this thesis is to advance the development of the WEC using experimental and analytical techniques. The first objective is to develop a dynamics model for prediction of WEC power capture and experimentally verify its suitability. The second objective is to extend the model to account for the introduction of a frequency response control system. The extended model is to be setup to allow application of optimization algorithms to maximize the utility of the control system. The last objective is to investigate the technical and economic feasibility of a full scale WEC device integration into a remote island community power system.

The following specific contributions are sought:

1. To develop and validate a dynamics model that can be used to evaluate WEC performance with and without the tuned reacting body.

2. To develop a process, from first principles, for the sizing of an efficient implementation

of the SyncWave WEC.

3. To develop a mechanism for frequency response tuning of the reacting body, so that it can be used in addition to common methods of generator damping control.

4. To utilize the dynamics model to illustrate the power delivery of a large scale WEC implementation in irregular waves with comparison to the electrical needs of a remote coastal community.

## 1.2 Background

The following theory, descriptions, and discussions provide a foundation for the work presented in this thesis. Linear water wave theory, which draws on the field of fluid mechanics is presented first. Second, the spectral approach to ocean waves is introduced. Third, a basic description of the WEC operating concept is presented. Lastly, a discussion on the fundamental point absorbing WEC design parameters is given.

### 1.2.1 Ocean Waves

The temporal and spatial variation of the water surface displacement, $\eta$, about the mean surface elevation, $h$, for a regular, monochromatic ocean wave of amplitude $A$, angular frequency $\omega$, phase constant $\varepsilon$, that is propagating in the positive $x$ and $y$ axes with a direction $\theta$ from the $x$ axis can be expressed by Equation 1.1, where $k$ is the wavenumber defined as $k \equiv \frac{2\pi}{\lambda}$.

$$\eta(x, y, t) = \Re\left\{A \exp(-ikx\cos\theta - iky\sin\theta + i\omega t + \varepsilon)\right\} \tag{1.1}$$

A special case, given by Equation 1.2, results when no phase or directionality are considered ($\varepsilon = 0$ and $\theta = 0$).

$$\eta(x, t) = \Re\left\{A \exp(-ikx + i\omega t)\right\} \tag{1.2}$$

The wavenumber for water waves can be found by an iterative solution to the dispersion relation given by Equation 1.3.

$$\omega^2 = gk\tanh(kh) \tag{1.3}$$

In sufficiently deep water, where $h > 0.3\lambda$, the waves are not influenced by the ocean

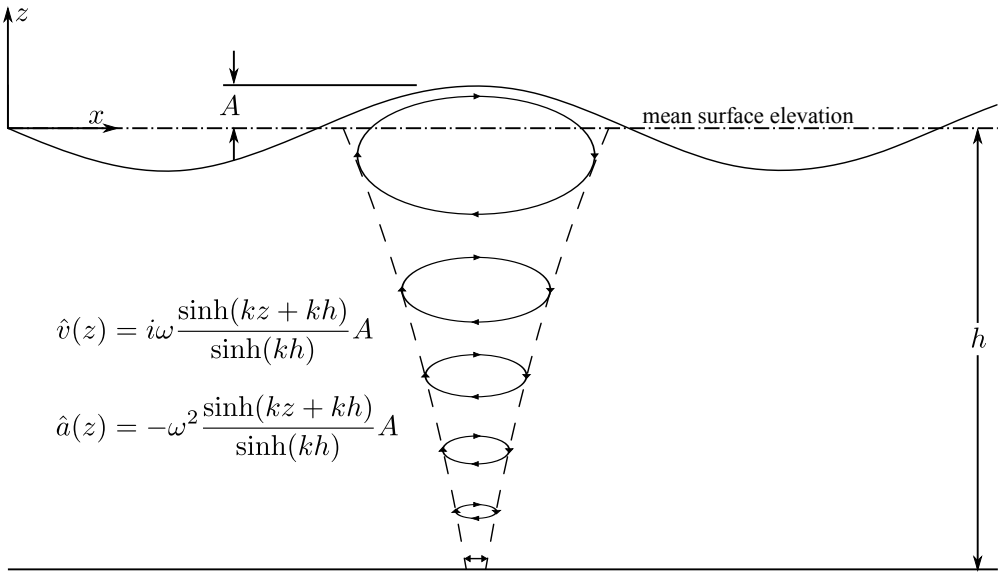


**Figure 1.1:** A diagram of Airy waves. Notice the elliptical particle trajectories as the wave progresses. The time dependent descriptions of the vertical particle velocities and accelerations are $v(z,t) = \Re\left\{\hat{v}(z)e^{i\omega t}\right\}$ and $a(z,t) = \Re\left\{\hat{a}(z)e^{i\omega t}\right\}$ respectively.

floor, so $tanh(kh) \to 1$ and as a result, $k = \frac{\omega^2}{g}$. The WEC is located at $x = 0$ so the water surface elevation is simply $\eta(t) = \Re\{A\mathrm{e}^{i\omega t}\}$.

Linear wave theory, first published by Sir George Biddel Airy, is developed using the Laplace equation for potential flow, with its associated assumptions (the fluid is inviscid, incompressible, and irrotational), to govern the fluid domain. By assuming that wave amplitudes are small, the free surface boundary condition can be linearized, enabling a solution to the boundary value problem on the fluid domain. The water particle velocities and accelerations below the water surface, according to the linear solution, in water of intermediate depth, are functions of wave frequency, wavenumber, depth, and water depth, as shown in Figure 1.1.

### 1.2.2 The Wave Spectrum

By utilizing the assumption that all waves maintain a small amplitude, the principle of superposition can be invoked to describe the surface of a random, irregular sea. Multiple

wave systems, each described by Equation 1.1, of various amplitudes, frequencies, and directions are summed to represent the ocean surface (see Figure 1.2). The spectral density

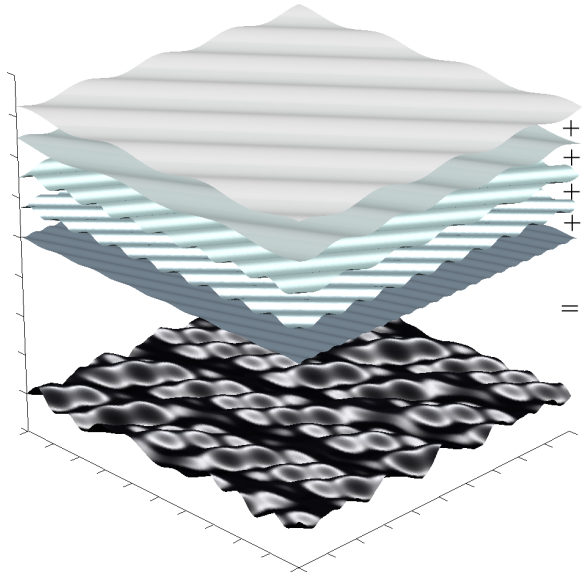


**Figure 1.2:** An illustration of the superposition of ocean waves. Monochromatic propagating waves, shown by the lightly shaded stacked surfaces, of different amplitudes, frequencies, and directions can be superposed to represent the ocean surface shown as the heavily shaded bottom surface.

function, $S(\omega)$, also known as the 'wave spectrum' of a sea-state, is a continuous function that represents the instantaneous distribution of variance in water surface elevation across the frequency range. If the physical constants $\rho g$ are applied (i.e. $\rho g S(\omega)$), the spectral density function represents the distribution of wave energy across the frequency range. The total energy per unit surface area in a sea-state is directly proportional to the area under its spectral density function. Semi-empirical relationships, established from decades of oceanographic study, such as the Pierson–Moscowitz spectral form, describe typical shapes of the spectral density function. These spectral forms are of major importance to marine engineers as they allow the synthesis of statistically representative ocean surfaces, $\eta(t)$, from basic statistical parameters, and they allow the estimation of the probability of occurrence of any sea-state. The pair of parameters, $H_s$ and $T_p$, are commonly used for fitting spectral forms to discrete measured or modeled wave data. Peak frequency, $\omega_p$, and peak period, $T_p$, are the wave frequency and corresponding period at which $S(\omega)$ is a maximum. The total energy per unit surface area in an irregular sea-state is proportional to the square of the significant wave height, $H_s$, in the same way that the energy per unit surface area

in monochromatic wave is proportional to the square of its wave height. Significant wave height, $H_s$, as defined in practice by Equation 1.4 in both the continuous and discrete forms [9], is a fitting parameter based on the area under the spectral density function that is indicative of the intensity of a sea-state.

$$H_s \equiv 4\sqrt{\int_0^\infty S(\omega)d\omega} = 4\sqrt{\sum_i^N S(\omega_i)\Delta\omega} \tag{1.4}$$

The Pierson–Moscowitz spectral form, shown in Figure 1.3 with comparison to spectral

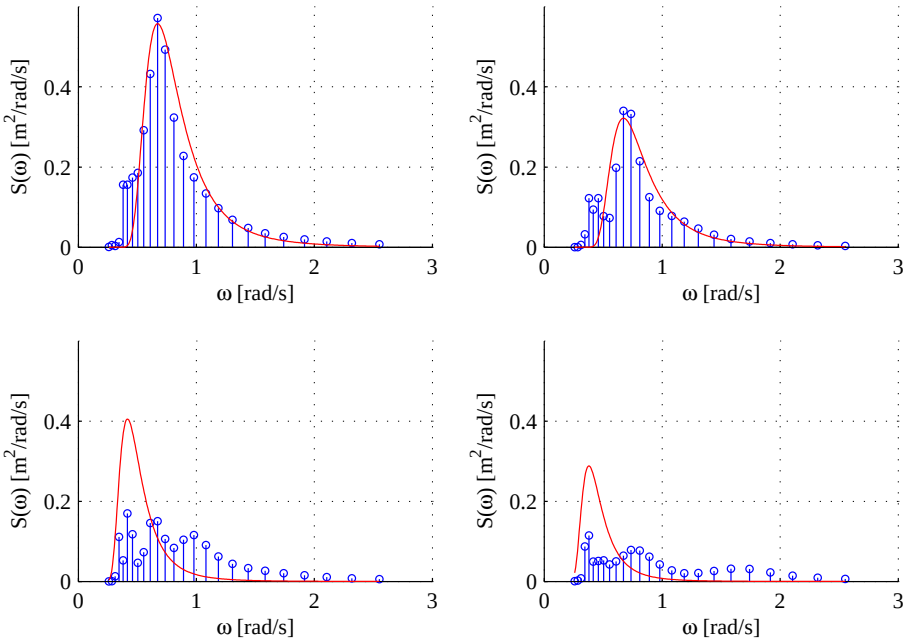


**Figure 1.3:** Four examples of wave spectra. Individual plots show the comparison of NOAA Wavewatch3 hindcast spectral data (indicated by stems) to a fitted Pierson-Moscowitz spectral form indicated by the solid lines. The top left plot shows a particularly good fit, top right shows a reasonable fit, whereas the lower plots are relatively poor fits—showing the limitations of the Pierson-Moscowitz spectral form for broad-banded spectra.

data produced by the NOAA Wavewatch 3 model—a global wave propagation model driven by sattelite-based wind measurements, is synthesized using the pair parameters $H_s$ and $T_p$ in this thesis. The comparisons between the discrete Wavewatch 3 spectra and the Pierson–Moscowitz spectral form shown in Figure 1.3 reveal that, depending on the applicability of the underlying assumptions, the quality of fit can vary.

### 1.2.3 Point Absorbing Wave Energy Conversion

The SyncWave WEC, is classified as an offshore, self-reacting, point absorber. The term self-reacting means that the device captures energy from the relative motion between floating components as opposed to energy capture from motion relative to a fixed reference (the ocean floor). The benefits of a self-reacting WEC, over devices that react against the ocean floor are two-fold:

1. A 'self-reacting' WEC is inherently more capable of surviving storms which produce extreme waves, because the WEC can be adjusted to allow the extreme waves to pass over the device while enduring minimal mechanical stress, similar to a wind turbine fitted with a 'coning' rotor used to minimize mechanical stresses during extreme winds.

2. A 'self-reacting' WEC is expected to experience significantly less mooring and structural contact forces during operation. As a result, it can be manufactured using less material, therefore reducing manufacturing costs and cost of energy [3].

The SyncWave WEC is composed of a float and spar with heave natural frequencies, $\omega_1$ and $\omega_2$ respectively. By design, the float and spar natural frequencies in heave are not equal, $\omega_1 \neq \omega_2$. Consider the frequency response of a classic one degree of freedom (DOF) oscillator that is exposed to a harmonic base excitation of frequency, $\omega$. The ratio of the excitation frequency to the oscillator's natural frequency, $\omega/\omega_j$, will determine the amplitude and phase of the oscillator's response. Assuming the oscillator is under-damped, the amplitude and phase responses are sensitive to the frequency ratio, $\omega/\omega_j$, when the excitation is near the classic criteria for resonance, $\omega/\omega_j \approx 1$. Since the float and spar are exposed to wave excitation of the same frequency, $\omega$, but have unequal natural frequencies, $\omega_1 \neq \omega_2$, it follows that their frequency ratios will not be equal, $\omega/\omega_1 \neq \omega/\omega_2$. Thus, the float and spar will respond with different amplitudes and phases to the wave excitation. So the fundamental operational concept of the SyncWave WEC is as follows:

*For a given wave frequency, there will be some relative motion between the float and spar from which energy can be extracted.*

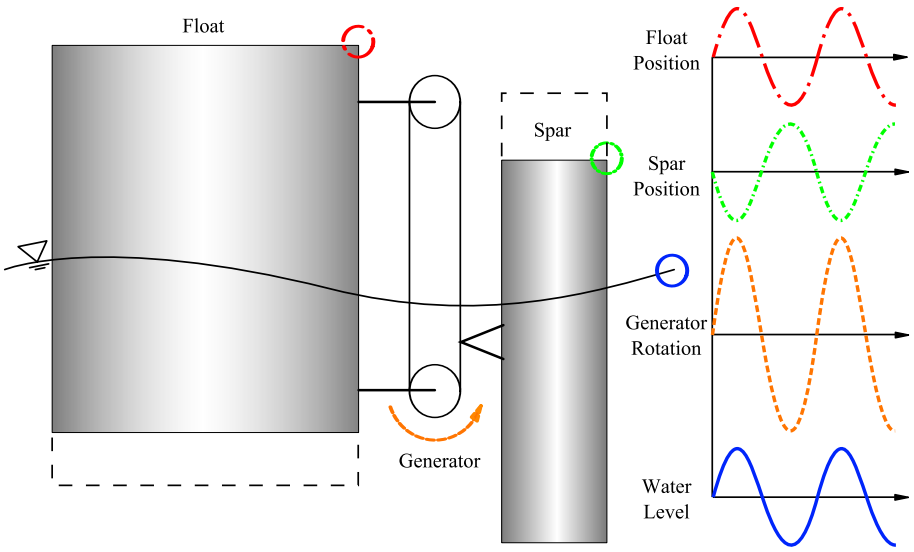


**Figure 1.4:** An idealized schematic of the WEC operation. The float has large water plane diameter and therefore a high hydrostatic stiffness causing it to behave as a "wave-follower." The spar has a small water plane diameter and therefore a relatively low hydrostatic stiffness causing it to move out of phase with the wave. Relative float-spar displacement causes generator rotation. Thus, the superposition of the float and spar motions result in generator rotation. This diagram is idealized because, in actuality, the spar undergoes a smaller displacements and less phase difference with respect to the water surface than is shown here.

As shown by the schematic in Figure 1.4, a power-take-off (PTO) is mounted between the float and spar to extract energy from the relative float-spar motion.

## 1.3 Methods of this Thesis

A two-body scale prototype WEC, dubbed 'Charlotte,' was developed in the months preceding experimental tests performed at the BC Research Ocean Engineering Centre, Vancouver, B.C. in September 2006. The experimental dynamics and power capture results were used to validate results derived from a heave constrained linear dynamics model in the frequency domain.

The experimental results were used to guide a series of recommendations for design improvement. Power capture improvements were expected with the introduction of an internally housed reaction mass coupled to a rotational system with variable inertia. To quantify the potential benefits, the dimensionality of the frequency domain dynamics model was extended to include the effects of the reaction mass and rotational system. The solution to the extended dynamics model was expressed as a smooth analytical function of the

control variables and subsequently used as an objective function for a Sequential Quadratic Programming procedure with nonlinear constraints.

Lastly, a set of specifications of a full-scale WEC design were used in combination with publicly available archived wave data to compare realistic power capture data (obtained using the developed modeling and optimization codes) to the requirements of a remote island community in a wave/diesel hybrid scenario.

## 1.4 Thesis Organization

This thesis describes many aspects of development of the SyncWave WEC, hereafter referred to as 'the WEC'. First, a small scale wave-tank model is designed and tested. The mechanical design and experimental procedure are presented. The test results are compared to the output from a two DOF linear dynamics model, which is developed with all specific and general assumptions stated.

Next, a parametric design of the two body WEC is developed to investigate the effects of spar natural frequency adjustments. This lays the foundation for the presentation of a novel tuning system intended to provide the spar natural frequency adjustments. The two DOF dynamics model is then expanded to three DOF to account for the tuning system. A numerical optimization process, based on the three DOF model, are then presented and used to maximize theoretical power capture.

Further, a spectral representation of ocean waves is applied for estimation of power capture in irregular waves and used to estimate power capture of a full–scale WEC at a case study location using hourly wave statistics. Wave power capture is compared in detail to community electrical power demand. Grid penetration levels are computed to assess the level of technical challenge associated with the integration of the WEC with the community electrical system.

The contributions of this thesis are presented in three papers:

1. Modeling, Design, and Testing of a Two-Body Heaving Wave Energy Converter (BEATTY, S., BUCKHAM, B., and WILD, P., Presented, International Society of Offshore and Polar Engineers, ISOPE, Lisbon, 2007; Submitted, Proc. International Journal of Offshore and Polar Engineering, 2008);

2. Frequency Response Tuning for a Two-Body Heaving Wave Energy Converter
   (BEATTY, S., BUCKHAM, B., and WILD, P., Presented, International Society of Offshore and Polar Engineers, ISOPE, Vancouver, 2008; Submitted, Proc. International Journal of Offshore and Polar Engineering, 2008);

3. Integration of a Wave Energy Converter into the Electricity Supply of a Remote Alaskan Island (BEATTY, S., WILD, P., and BUCKHAM, B., Submitted, Journal of Renewable Energy, 2008);

These papers ore contained in appendices A, B, and C respectively. The body of the thesis contains three chapters, 2 to 4, which describe the papers in the appendices, including the methodology, and a discussion of significant findings. Chapter 5 presents the conclusions of the combined papers, and discusses potential future work.

## 1.5 Other Relevant Publications

During the research, innovative concepts for the frequency response control system were contributed which resulted in the submission of United States and International patent applications. In addition, ongoing work to develop a large-scale WEC within an academic-industrial consortium has led to a conference submission outlining WEC design and analysis methodologies.

1. PCT Patent No. WO 2007/137426 A1 - Wave Energy Converter.
   (PROTTER, N., BEATTY, S., and BUCKHAM, B.J., World Intellectual Property Organization, 2007);

2. Design Synthesis of a Wave Energy Converter
   (BEATTY, S., HILES, C., NICOLL, R., ADAMSON, J., and BUCKHAM, B., Accepted, International Conference on Ocean, Offshore and Arctic Engineering, OMAE, Honolulu, 2009);

# Chapter 2

# Dynamics Modeling and Experimentation

A linearized dynamics model is used to predict the displacements of the WEC floating bodies in the frequency domain. To illustrate the WEC operational concept and validate the dynamics model, a small scale two-body WEC model was designed and constructed from May through September 2006. The model was tested in a wave channel in September 2006. The modeling, design, and testing results are outlined in detail in Appendix A.

## 2.1 Wave Excitation Forces

The wave excitation force on a floating body $j$ due to incident waves, with its geometry defined by Figure 2.1, is based on the assumptions that the floating body undergoes small displacements and that body $j$ is small with respect to the wavelengths in the horizontal plane. The assumption of small displacements enables the application of the principle of superposition. The small body approximation neglects variation of water surface displacement over the body in the horizontal plane. As a result, volume and surface integrals that would normally be required to obtain excitation force from pressure distributions, collapse to simple expressions. Derivation of the approach for an axi-symmetric body is given by Falnes [10] and applications of the approach can be found throughout wave energy literature [11] and in the analysis of offshore structures [12].

The wave excitation force, $f_{e,j}$, is calculated as if the body is held fixed. The force, $f_{e,j}$, is superposed with forces experienced by the body $j$ due to its own motion in the ordinary differential equation that governs the resulting motion of floating body $j$. Assuming steady state oscillations, excitation force can be represented by a complex amplitude multiplied

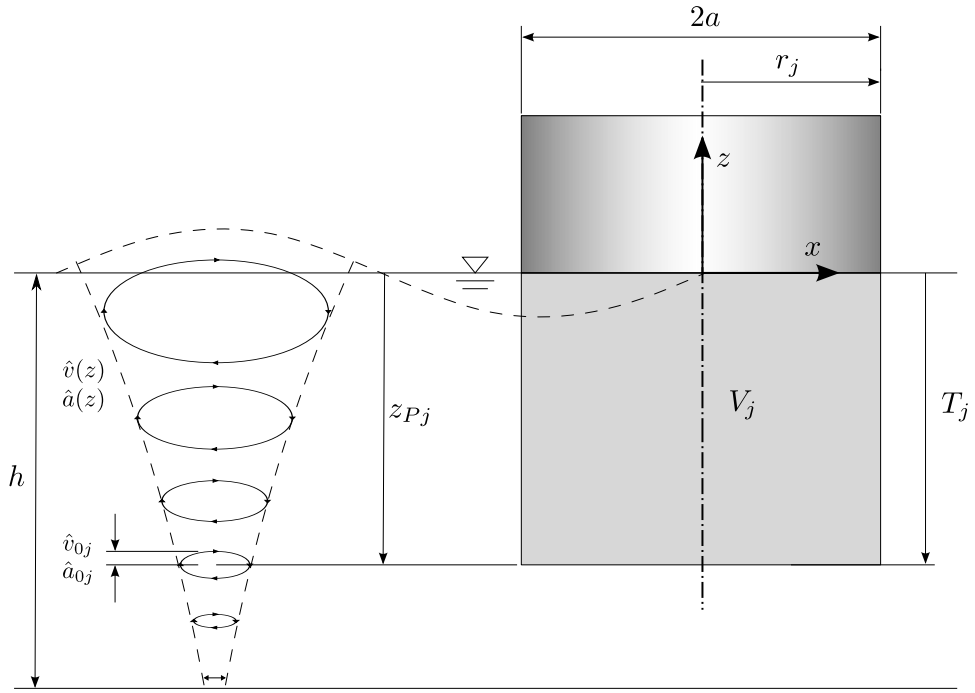


**Figure 2.1:** A cylindrical floating body $j$ in regular Airy waves of amplitude, $A$, in water depth, $h$. Body j is characterized by its radius at the water-plane, $r_j$, draft, $T_j$, and submerged volume, $V_j$. The reference depth, $z_{Pj}$, is the depth at which the vertical velocity and acceleration of the fluid particles is considered to interact with the body. This image is not to scale

by a time dependent oscillatory component as in Equation (2.1).

$$f_{e,j}(t) = \Re\left\{\hat{f}_{e,j}\mathrm{e}^{i\omega t}\right\} \tag{2.1}$$

The complex amplitude of the wave excitation force, represented by Equation (2.2), has three components. On the right hand side of Equation (2.2), the first term accounts for inertial effects due to the acceleration of the fluid, the second term accounts for drag effects due to the velocity of the fluid, and the last term accounts for hydrostatic pressure changes due to the surface displacement of the fluid.

$$\hat{f}_{e,j} = \left[-\omega^2\rho V_j(1+\mu)\frac{\sinh(kz_{Pj}+kh)}{\sinh(kh)}A + i\omega c_j\frac{\sinh(kz_{Pj}+kh)}{\sinh(kh)}A + k_jA\right] \tag{2.2}$$

There are two contributions to the inertial term of Equation (2.2). Falnes [10] attributes the contribution, $\rho V_j$, to the pressure field associated with the undisturbed fluid potential

of the incident wave. Secondly, in the approach of Falnes, the added mass term, $\rho V_j \mu$, is attributed to the effects of diffraction—the fluid potential field from waves scattered by the body $j$ when it is held fixed. In another approach, consistent with Falnes' description of the physical phenomenon, Dean and Dalrymple [13] describe that, "the pressure gradient required to accelerate the fluid exerts a so-called "buoyancy" force on the object, corresponding to the $[\rho V_j]$ term... An additional local pressure gradient occurs to accelerate the neighboring fluid around the cylinder. The force necessary for the acceleration of the fluid around the cylinder yields the added mass term, $[\mu]$."

Falnes [10, 11] neglects the second term in Equation 2.2 representing the force due to the radiation of waves. However, force contributions from viscous drag effects, seen from experiments to be small but not insignificant, have been blended into the second term in Equation (2.2). Thus, in this work, the damping coefficient, $c_j$, includes both wave radiation and viscous damping effects.

The ratios containing the sinh terms account for the depth dependence of the fluid velocity and accelerations, as established from linear wave theory in Section 1.2.1. The fractional sinh terms decay to zero as $z \to -h$ and approach unity as $z \to 0$. Consistent with the approaches of Falnes [10,11] and Clauss [12], the fractional sinh terms are evaluated at a reference depth, $z_{Pj}$ which can be seen in Equations (2.3) and (2.4). The reference depth is the depth at which the vertical fluid velocity and acceleration components interact most strongly with the structure.

$$\hat{a}_{0j} = -\omega^2 \frac{\sinh(kz_{Pj} + kh)}{\sinh(kh)} A \tag{2.3}$$

$$\hat{v}_{0j} = i\omega \frac{\sinh(kz_{Pj} + kh)}{\sinh(kh)} A \tag{2.4}$$

In the case of a cylindrical object, as seen in Figure 2.1, the reference depth is set equal to the draft of the cylinder [12] ($z_{Pj} = T_j$). In the case of a submerged, horizontally aligned, flat plate, the reference depth is set equal to the depth of submergence of the plate [11]. The reference depth for the non-cylindrical spar shape considered in Appendix A is approximated by a weighted average of the protruding areas normal to the heave direction

as described by Equation (21) and Figure 5 of Appendix A.

## 2.2 Fundamental WEC Design Parameters

The WEC is composed of two floating bodies, a wide float and slender spar (sometimes called the pillar), that oscillate in the vertical direction (heave). If body $j$ is displaced in the vertical direction from its equilibrium position by a distance, $\Delta z$, there will be change in the buoyancy force exerted on the body, $\Delta F_b$, that is proportional to the change in the submerged volume. For an object that has a constant cross-sectional area at the water-plane, such as the cylindrical body shown in Figure 2.1, the change in submerged volume depends only on the vertical displacement, as seen in Equation (2.5).

$$\Delta F_b = -\rho g \pi r_j^2 \Delta z = -k_j \Delta z \tag{2.5}$$

$$k_j = -\frac{\Delta F_b}{\Delta z} = \rho g \pi r_j^2 \tag{2.6}$$

The change in hydrostatic force per unit vertical displacement of the body is termed "stiffness" because it is analogous to the stiffness of a mechanical spring (units of N/m). Denoted, $k_j$, the stiffness of body $j$ is given by Equation (2.6).

A single floating body $j$ can be modeled as a classical one DOF oscillator with mass, $m_j$, stiffness, $k_j$, and damping $c_j$. By continuing the analogy with a mechanical oscillator, the undamped heave natural frequency of body $j$ can then be computed using Equation. (2.7).

$$\omega_j = \sqrt{\frac{k_j}{m_j}} = \sqrt{\frac{\rho g \pi r_j^2}{m_j}} \tag{2.7}$$

It should be apparent from Equation. (2.7) that, through design decisions on the diameters and masses of any floating body, the heave natural frequencies can be arbitrarily chosen within physical constraints. For application to the WEC in this thesis, the diameters and masses are specifically chosen so that the float and spar have different heave natural frequencies.

## 2.3 Two Degree of Freedom Dynamics Model

The heave oscillation of the floating bodies in this thesis is modeled using a system of two coupled linear ordinary differential equations with constant coefficients. The excitation of the system is provided by forces induced by the waves. A schematic of the dynamics model is shown in Figure 2.2. The float and spar are indicated as body 1 and 2, respectively. The major assumptions inherent to the modeling approach are:

1. the float and spar oscillate at steady state;
2. the float and spar oscillate in the heave direction only;
3. the float and spar are small with respect to the wavelengths in the horizontal plane so that the bodies do not "bridge" wavelengths;

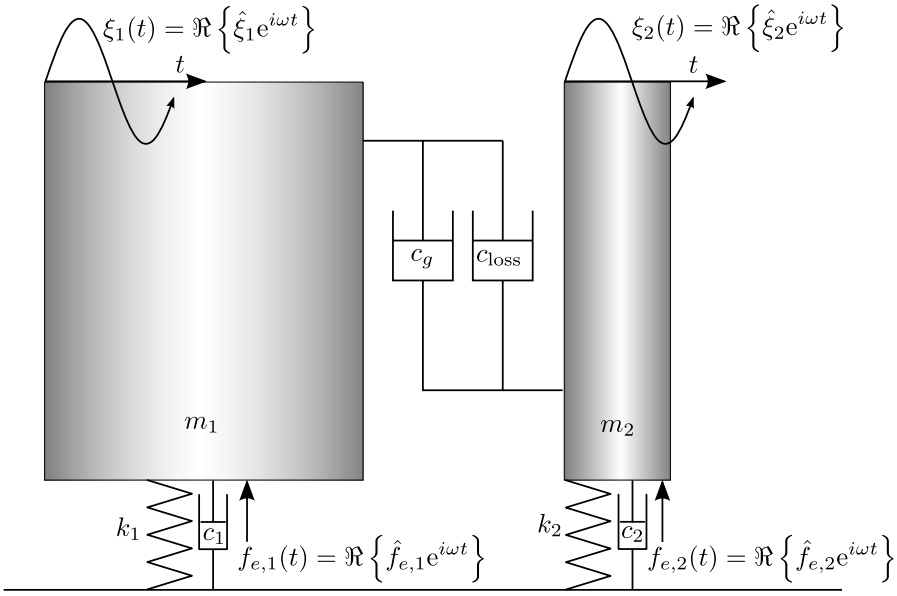


**Figure 2.2:** A schematic of the two DOF dynamics model. The power dissipated through the viscous dashpot, with a damping coefficient of $c_g$, represents the useful power captured by the WEC. Frictional losses are represented here by the dashpot with a damping coefficient, $c_{loss}$.

The solution of the dynamics model at each wave frequency yields the complex amplitudes of the steady state displacements of the float and spar, denoted $\hat{\xi}_1$ and $\hat{\xi}_2$ respectively. Using the relative displacement between the float and spar $\hat{\xi}_{1/2} = \hat{\xi}_1 - \hat{\xi}_2$, the power captured by the WEC in regular waves is found from the average energy dissipated over the

power-take-off damper per cycle, given in Equation (2.8).

$$P(\omega) = \frac{1}{2}\omega^2 c_g |\hat{\xi}_{1/2}|^2 \tag{2.8}$$

## 2.4 Small Scale Prototype Design

The design of the wave tank prototype, shown by the drawings in Figure 2.3, was implemented using readily accessible and machinable materials. Material and component choices were guided by budgetary constraints, material accessibility, and ease of manufacture. As such, the float and spar hulls were made using PVC pipes normally used for municipal drinking water distribution. Primary structural elements were manufactured from aluminium bar, tube, and plate. Some of the design strategies used on this device do not apply to ocean scale devices because the wave tank prototype was intended as a research device to be used in a controlled wave tank environment only. The spar and float components of the proof-of-concept WEC was sized so that the natural frequencies of each floating body fell within the wave frequency range of the wave maker. The draft of the spar was limited by the tank depth and maximum expected heave oscillations. In consideration of pitch stability, it was desirable to maintain a low center of gravity and a high center of buoyancy. As a result, the spar center of gravity was lowered by attaching a ballast 'bulb' filled with lead weights to the bottom of the spar. The center of buoyancy was raised by attaching streamlined foam buoyancy collars to the spar.

A linear guide system, using recirculating ball-bearings running on hardened stainless steel shafts, enabled low friction linear relative motion between the float and spar. The linear relative motion is translated to rotation using a plastic coated cable chain that engages with both a drive sprocket and an idler sprocket on the spar. The driven shaft, sealed using a dynamic O-ring, penetrates through the generator housing which forms the top-most portion of the spar. The driven shaft connects to a DC generator through a toothed belt transmission with a four-to-one drive ratio, as seen in Figure 2.4(b). Specific design details are given in Appendix A. Note that the spar is referred to as the "pillar" in Appendix A. A brush commutated DC generator, modeled as a linear viscous dashpot with damping coefficient $c_g$, was used for the PTO. A series of bench-top tests were performed

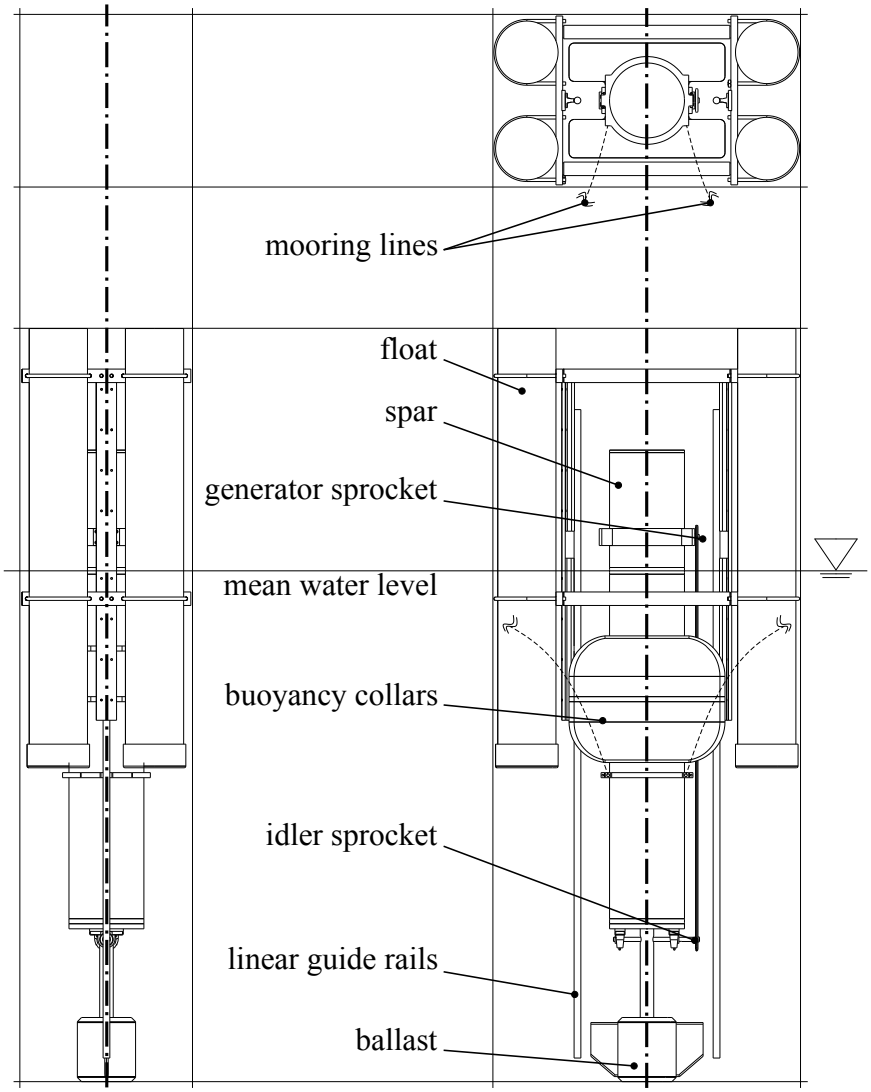


**Figure 2.3:** Orthographic projections of the wave tank prototype WEC with labels of basic features.

to characterize generator specific constants so that the generator damping coefficient could be set by the resistance of an external circuit through Equation (29) of Appendix A.

To facilitate mechanical shaft-power measurements, the PTO system was designed to ensure the input shaft torque could measured using the combination of a force signal from an offset load cell with a rotational position/velocity signal from an optical encoder. The design of the PTO system is shown in Figure 2.4(b). Because the generator shaft rotation is kinematically coupled to the float-spar relative translation through the generator sprocket and belt-drive, the optical encoder signal also enabled measurement of the relative float-spar

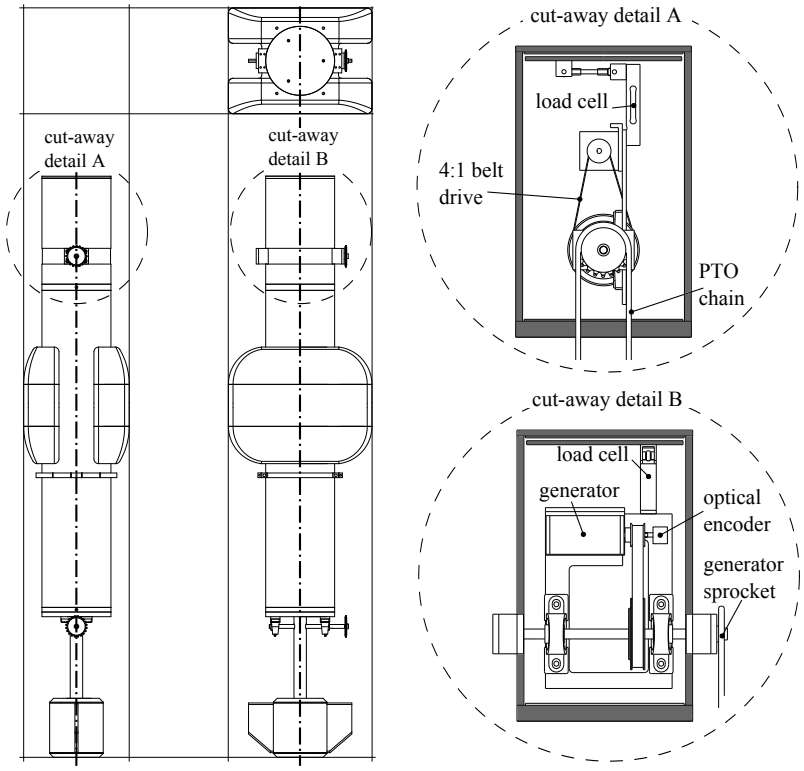


(a) Spar design (b) Generator housing cut-away views

**Figure 2.4:** Orthographic projections of the spar with generator housing cut-away views. The cylindrical spar hull and end caps have been cut-away (sectioned portions indicated by gray shading) to reveal the power take off mechanism within the generator housing.

motion, $\hat{\xi}_{1/2}$.

## 2.5 Wave Tank Testing

The WEC device was tested in September 2006 at the Ocean Engineering Center in Vancouver, British Columbia—at that time operated by Oceanic Consulting Corporation. The WEC can be seen during the testing in Figure 2.5. The testing, as described in detail in Appendix A, was done in a tank of 2.4m depth, 3.6m width, and 100m length and the wave maker was capable of producing regular waves of 25cm maximum height. The testing was done in two phases. In the first phase, 'drop tests' were done for each of the float and spar in the absence of waves. The hydrostatic stiffness values, $k_j$, were easily obtained from the known water plane areas of the float and spar. Accounting for frictional damping from the linear guides, damping coefficients and added mass coefficients for each body were experimentally determined for the float and spar using decaying heave oscillations of each


**Figure 2.5:** A photo of the wave tank prototype during testing September 2006.

body, seen in Figure 6 of Appendix A. The damping coefficients were extracted using the method of logarithmic decrement. The added mass coefficients were obtained by comparing the mass values extracted from the frequencies of experimental heave oscillation via the relationship $m_j = k_j/\omega_j^2$ to the known physical masses of the float and spar.

In the second phase, regular waves of constant height were propagated in the tank while the water elevation, 6 DOF motion, shaft power, and DC electrical power signals were sampled at a rate of 1 kHz using a data acquisition system. Multiple runs were done at various wave frequencies across the wave maker's frequency bandwidth capability. A single capacitance type wave probe was utilized for water surface elevation measurements.

With reference to the steady-state wave tank tests, discussions of the validity of the major assumptions inherent to the dynamics model are given below. The float-spar relative motion signal from the rotational encoder was nearly sinusoidal with zero mean. During data analysis, attention was given to ensuring the measurement window did not contain signals with amplifying and decaying amplitudes, thus for the wave tank tests, the model assumption of steady-state oscillations is considered valid.

The WEC displacements in six DOF were logged using an LED based motion capture

system. By post processing the data using inverse kinematics, the pitch, roll, and yaw rotations about the y, x, and z axes respectively in the coordinate system defined by Figure 2 of Appendix A were extracted. The maximum WEC pitch angle observed was 2.2 degrees from the vertical. The roll and yaw rotations were an order of magnitude lower than pitch rotations. Thus the assumption of pure heave motion, necessary for comparison of experimental power capture to the dynamics model results, was validated.

For the small body approximation to the wave excitation force to hold, the radius of the body parallel to the wave propagation, denoted $a$—labeled in Figure 2 and Figure 4 of Appendix A, is required to be small compared to the wavelength $\lambda$. Formally stated by Falnes [14], the small body approximation is $\max(ka) \ll 1$, where $k$ is the wavenumber. Since the wavenumber is formally defined as $k \equiv 2\pi/\lambda$, the expression can be rewritten as $\max(2\pi a/\lambda) \ll 1$. During the steady-state tests, the highest wave frequency tested was 4.1 rad/s (0.65Hz) and the ratio of the WEC in the direction of wave propagation to the wavelength was approximately 0.23 resulting in $\max(ka) = 0.54$ for the tests. Thus, the lower frequency data is considered to adhere to the small body approximation; However, for the higher frequency data, error due to violation of the small body approximation could be dominant.

## 2.6 Theoretical Power Calculation

Through Equation (2.8), theoretical power capture was computed by supplying the dynamics model with the necessary mass, stiffness, damping, and wave parameters. The PTO damping coefficient was obtained for input to the dynamics model from the bench top generator damping test results. For all experimental runs, the wave height was obtained by taking the primary component of the Fourier transform of the wave elevation signal.

## 2.7 Experimental Power Calculation

The electrical output power of the DC generator could have been obtained from the power dissipated by the resistance in the external circuit, $R_{\text{ext}}$, through the relation $P_{\text{elec}}(t) = V^2/R_{\text{ext}}$. This option was rejected because it is dependent on the losses inherent to the generator's conversion of mechanical to electrical energy. To provide a measurement of gross power extraction, the experimental power signal was established from the instantaneous

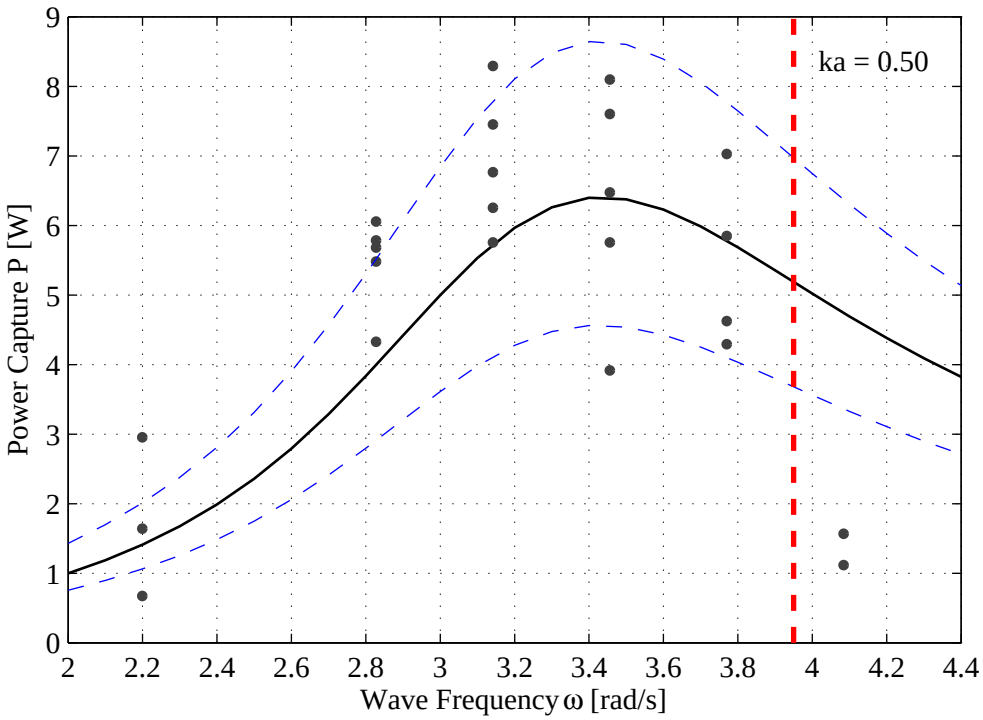


**Figure 2.6:** Experimental vs. dynamics model power capture. Experimental data is indicated by dots. Model data at the mean wave height is indicated by the solid line and model data for +/- one standard deviation in wave height is indicated by dashed lines. The small body approximation is considered valid for wave frequencies below, and invalid above, the indicated $ka = 0.5$ line.

torque, $\tau(t)$, and rotational speed $\dot{\theta}_{\text{gen}}(t)$ signals from the generator shaft. An instantaneous power capture signal through the relation $P_{\text{mech}}(t) = \tau(t)\dot{\theta}_{\text{gen}}(t)$ was computed. Thus, assuming the linear guide and linear to rotational conversion losses are negligible, the shaft power signal was comparable directly to theoretical power dissipation derived from the dynamics model.

## 2.8 Results and Discussion

As a result of the tests, the two body prototype WEC successfully illustrated the self-reacting point absorber concept. Observing Figure 2.6, the experimental data follows the theoretical trend reasonably well at low frequencies, although there exists a high variance in the experimental data about the general trend. The scatter in the experimental power signal is attributed to three main sources, summarized below.

1. Significant wave reflections were experienced by the WEC model after a few seconds of clean incident waves because the wave channel facility was fitted with an ineffective

beach. Thus filtering, using Fourier transforms, of the wave elevation signal was required.

2. The wave maker was not capable of producing waves of consistent nominal height throughout the frequency range. A statistical analysis of the primary wave components for the steady state tests yielded a mean height of 19cm with a standard deviation of 3cm. Since the power transmitted in waves is proportional to the square of the wave height, the standard deviation of 3cm is significant.

3. Backlash in the PTO system resulted in spikes in the torque signal. Even after low pass-filtering the signal, some residual error remained in the mechanical power data.

4. The DC generator was undersized for the application. As a result, lack of precision in the setting of the PTO external circuit resistance, $R_{ext}$, resulted in errors in the generator damping level experienced by the WEC.

The divergence of the experimental data from the dynamics model, as seen in Figure 2.6, at roughly 4.1 rad/s (the highest frequency tested) is attributed to a violation of the previously discussed small body approximation. At this frequency, the float was observed to 'bridge' wavelengths, thereby mitigating the pure excitation forces felt in waves of lower frequency and longer wavelength.

## 2.9 Summary

This chapter summarized the manuscript contribution in Appendix A. A two DOF dynamics model was developed to predict the displacements of the WEC floating bodies in the frequency domain. An account of the design, construction, and testing of a proof-of-concept two body WEC model was given. Although experimental problems were encountered, the test results provided reasonable confidence in the dynamics model from the validation of trends in Figure 2.6. The dynamics model is the vehicle for the investigations of the next chapter. The next section of the thesis introduces a frequency response tuning system to maximize power capture of a more current, ocean-representative device.

# Chapter 3

# Frequency Response Tuning

This chapter summarizes the development of a frequency response tuning system, discussed in detail in Appendix B, using the dynamics model produced in Chapter 2. The frequency response tuning research was conducted in the context of the design of a small scale device suited for the wave tank size and wave making capabilities of the National Research Council Institute for Ocean Technology (IOT), located in St. John's, Newfoundland. Testing at the IOT is considered the next step in the WEC technology development process. Since the relationships between WEC geometry and WEC performance are complex, a model-based design methodology is developed and applied to the small scale WEC in this chapter.

First, a parametric description of the WEC is developed that translates a desired natural frequency into a hull geometry and mass. Considering a family of WEC's derived from the parametric design philosophy, an optimization and sensitivity study was undertaken to understand what benefits may be available if the natural frequency of the spar could be adjusted. Next, the internal frequency response tuning system is presented as a feasible means to create the desired natural frequency adjustments and a three degree of freedom dynamics model, extended from previous work, is used to evaluate the performance of a single WEC geometry that employs the internal tuning system.

## 3.1 Parametric Spar Hull Design

Since the power capture of the WEC is directly related to the frequency responses of the individual WEC components, the natural frequencies associated with the oscillating bodies are seen as fundamental design parameters. For a single floating body $j$, the undamped

heave natural frequency is expressed, as for any one DOF oscillating system by Equation (2.7).

According to Archimedes [15], "If a body which is lighter than a fluid is placed in the fluid, it will be immersed to such an extent that a volume of fluid which is equal to the volume of the part of the body immersed has the same weight as the whole body." In other words, the mass of a floating body must be equal to the mass of water it displaces. For a cylindrical floating body, volume displaced by the body is the product of its draft, $T_j$ and its cross-sectional area at the water-plane, $\pi r_j^2$.

$$m_j = \rho V_j \tag{3.1}$$

$$V_j = \pi r_j^2 T_j \tag{3.2}$$

Subsequently, the heave natural frequency of a cylindrical body can be represented by Equation (3.3). The resulting Equation (3.3) indicates that, for a cylindrical body, the natural frequency is a function of only the body's draft.

$$\omega_j = \sqrt{\frac{\rho g \pi r_j^2}{\rho \pi r_j^2 T_j}} = \sqrt{\frac{g}{T_j}} \tag{3.3}$$

Since the float is very stiff in heave ($k_1$ is large), its response is that of a "wave-follower"—meaning the float responds in phase with the wave. To achieve relative displacement with the float, the spar must have a response out of phase with the wave excitation. Further, to maximize the relative response, $\hat{\xi}_{1/2}$, and therefore power capture of the WEC, a relatively low spar natural frequency is desirable.

Consider sizing a cylindrical spar so that its natural frequency is in the range of common peak frequencies seen in the ocean (take the range $0.35 \leq \omega \leq 0.75$ rad/s observing the example wave spectra in Figure 1.3). By substituting the range of $\omega_2 = \omega$ into Equation (3.3) and solving for $T_2$, the draft of the cylindrical spar must be in the range $23.0 \leq T_2 \leq 157$ m. This result suggests, if the spar design is kept cylindrical, an extremely deep spar draft is required to achieve a low enough heave natural frequency for the operation of the WEC. To decrease the draft of the spar while maintaining a low spar natural frequency, it was

decided that the spar should deviate from an extruded cylindrical geometry below the water surface. Therefore a "bulb" structure, consisting of a tapered section, a larger diameter cylindrical section and a hemispherical portion provides an increase to the submerged volume while holding the water plane area constant. The resulting strategy enables a spar design of reasonable draft, while minimizing the ratio $k_2/m_2$.

A schematic, showing the parametric design of the WEC with a cylindrical float and non-cylindrical spar, is given in Figure 3.1. The spar hull shape resembles a baseball bat, similar to the design of the Scripps Institution of Oceanography's Floating Instrument Platform (FLIP) [16]. Since the spar considered here must support the mass of the internal tuning system in addition to its own mass, the bulb is sized to maintain static equilibrium of the spar/tuning system combination.

## 3.2 Sensitivity to Spar Natural Frequency

After choices of $H_{\text{design}}, a_1, a_2, a_3$ are made, based on mechanical design and site constraints, the parametric spar geometry, given by Equations (2-8) of Appendix B, enables a choice of spar natural frequency to completely define the spar geometry. Since the spar, of mass, $m_2$, must support the tuning system mass, $m_3$, the combined spar and tuning system mass has been labeled $m_{23} = m_2 + m_3$ which allows for later comparisons to a "mass-equivalent" WEC where the tuning system mass is locked to the spar and considered as ballast rather than an active control system. Using the two degree of freedom dynamics model developed in the previous chapter, the sensitivity of power capture to changes in spar design, defined by the natural frequency of the spar, was investigated. For the sensitivity study conducted here, the power calculations were done using an optimization of the generator damping coefficient, as is commonplace in wave energy literature [17–19]. The float was designed to have the highest natural frequency possible without bridging wavelengths (a violation of the small body approximation).

The results of the sensitivity and natural frequency optimizations show power capture benefits of up to 25% over the lowest frequency fixed natural frequency spar, shown in Figure 5 and 8 of Appendix B from 1.2 rad/s to 2.8 rad/s—a substantial portion of the frequency range, available if the spar natural frequency could be adjusted.

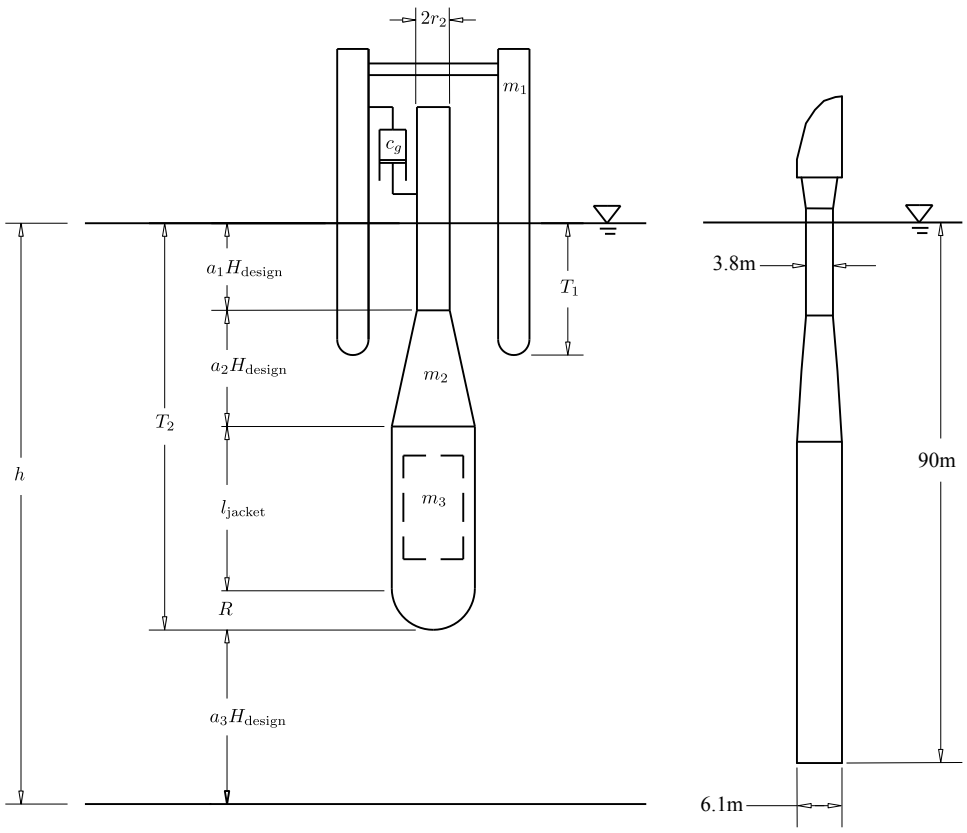


(a) Parameterized WEC geometry (b) FLIP

**Figure 3.1:** Schematic of the parameterized WEC geometry (a). In this schematic, $H_{\text{design}}$ is design wave height, $a1, a2, a3$ are geometric constants, $l_{\text{jacket}}$ is the jacket length, $R$ is the bulb radius, and $h$ is the water depth. The Scripps Floating Instrument Platform (b). The bulb design afforded an increase of the natural heave period from 19sec to 27sec (decrease of natural frequency from 0.33rad/s to 0.23rad/s) compared to a cylindrical spar of the same draft [16].

## 3.3 A Mechanical Tuning System

Rather than realize the heaving natural frequency adjustments through spar hull geometry changes, which is not practical, an internal mechanical tuning system mounted inside the spar will be exploited. The tuning system has mass $m_3$ labeled in Figure 3.1.

A schematic of the mechanical system, designed to enable additional frequency response tuning in addition to generator damping control, is shown in Figure 3.2. A spring supported reaction-mass, $m_3$,of mass comparable to the spar mass, is housed within the spar. The reaction-mass is constrained to oscillate along the vertical axis inside the spar. The oscillating reaction-mass is kinematically coupled to a rotational system with variable inertia.

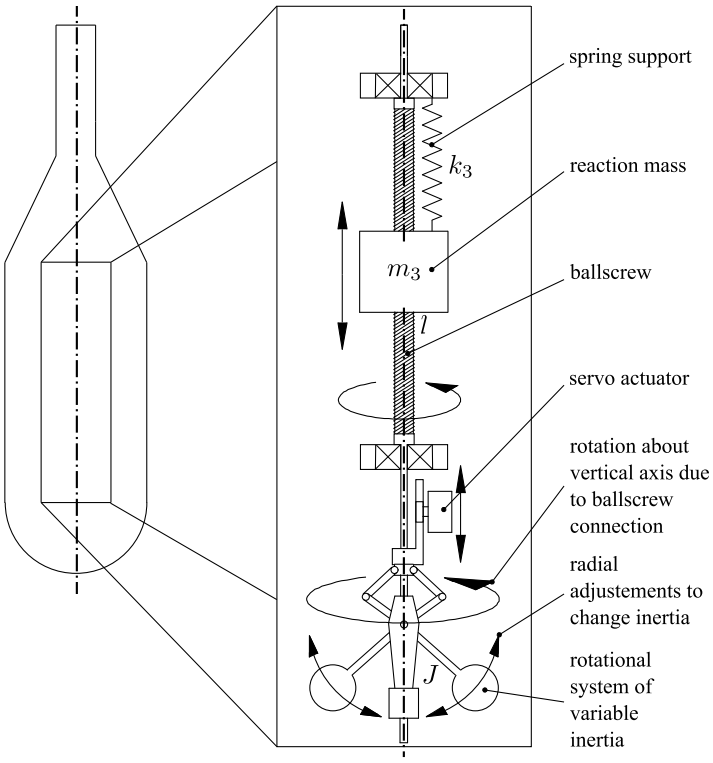


**Figure 3.2:** Schematic of the frequency response tuning system composed of an internal reaction-mass of mass $m_3$, ball screw of lead $l$, spring support of stiffness $k_3$, and rotational system with adjustable inertia, $J$ all housed within the spar. Gyroscopic effects due to the angular momentum about the vertical axis will tend to stabilize the WEC in pitch and roll.

The implementation shown in Figure 3.2 uses a ball screw to convert linear displacement of the reaction-mass to angular displacement of the rotational system. The inertia, $J$, of the rotational system can be adjusted by changing the radial distribution of mass of the rotational system through a 'flyball' apparatus using a hydraulic or electric servo, as shown in Figure 3.2.

## 3.4 Three Degree of Freedom Dynamics Model

In addition to the design frequencies of the spar and float, the heaving oscillations of the coupled three-body WEC(spar, float, and reaction-mass) are also dependent on the reaction mass, $m_3$, the support stiffness, $k_3$ and most importantly the rotational inertia, $J$.

Of the new variables introduced to the WEC model, $m_3, k_3$ and $J$, the rotational inertia, $J$, is the premier control variable for the three body WEC. It is conceivable to adjust the spar mass $m_2$ or reaction mass $m_3$ through a water ballast pump system, but a water

pumping system offers very slow frequency response tuning. Further, the support stiffness $k_3$ represents a possible control variable but an efficient system to provide sufficient stiffness range for frequency response tuning has yet to be invented. Lastly, since the inertia of a rotating system is proportional to the square of the radial position of the flyball masses, the flyball type inertial control offers fast, continuous, and efficient adjustments. Thus frequency response tuning by means of rotational inertia adjustment, using the concept shown in Figure 3.2, has been chosen for further investigation.

An inertial control parameter has been introduced to simplify the resulting dynamics equations and eliminate the need to choose a specific ball screw lead, $l$. Denoted, $m_4$, the inertial control parameter has units of kilograms and is related to the rotational inertia, $J$ and ball screw lead, $l$, by Equation (3.4).

$$m_4 \equiv \frac{J}{l^2} \tag{3.4}$$

Since there are three coupled oscillating bodies, the expanded dynamics model is a system of three coupled linear ordinary differential equations. A schematic of the three DOF mathematical model is shown in Figure 3.3. A detailed derivation of the extended equation system is given by Equations (21-30) in Appendix B and the final set of three body WEC system matrices are stated in Appendix B by Equations (34-36).

## 3.5 Scheduling the Control Variables

The control of the conceptual WEC is facilitated by coordinated adjustments of the generator damping level, $c_g$, and the inertial control parameter of the rotational system, $m_4$.

There are two primary strategies for tuning WEC's that are defined by their time-scale. The first, called a 'slow tuning' method, is to make control adjustments on a 10 to 30 minute basis. A slow-tuned WEC is controlled to optimize power capture as the general sea-state changes. The second, called 'fast tuning' or 'wave-to-wave control', is to make control adjustments on a one to five second basis—responding to individual incident wave shapes. Although fast tuning of WEC's is known to significantly increase the theoretical energy capture efficiency [1], a successful implementation of fast tuning could require orders

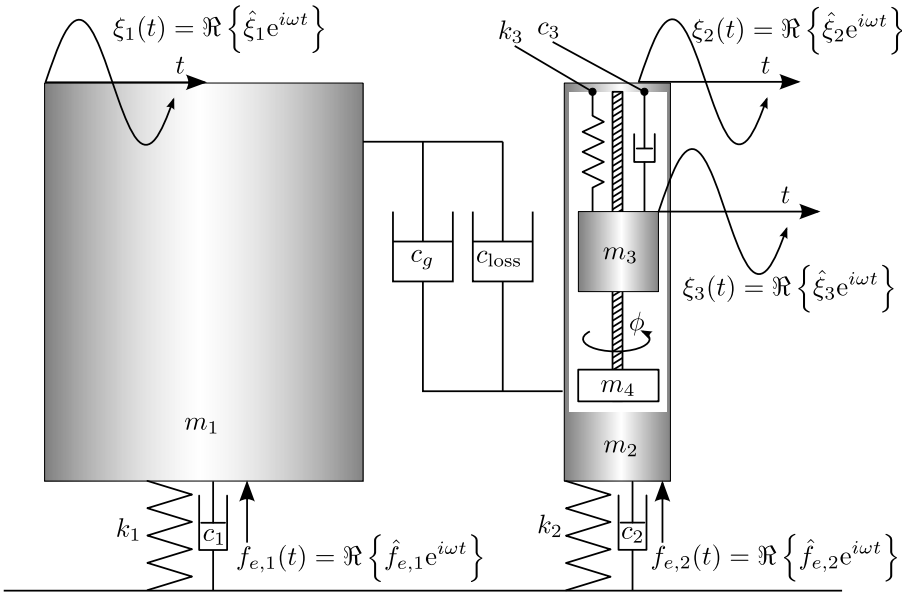


**Figure 3.3:** A schematic of the three DOF dynamics model.

of magnitude increases of forecasted wave data, provided by on-site sensors, than for slow-tuned WEC's. Wave measurements, data management, and optimization for 'fast-tuning' are currently subjects of world-wide research [20–23].

However, to develop base-line performance estimates of the WEC, this thesis proceeds by implementing a slow-tuning system for the three body WEC intended as a back-drop for future research into the implementation of a fast-tuning scenario utilizing the frequency response tuning mechanism shown in Figure 3.2.

For the 'slow-tuning' method used here, the omni-directional sea-sate is defined by its peak period, $T_p$, and significant wave height, $H_s$. For a typical wave spectrum, the most energetic wave components occur at the peak period, $T_p$. As a result, the WEC is optimized for the most energetic wave component, namely the peak period. The sea-state parameters are gathered either from accelerometer-based wave-buoy measurements or wind-data driven wave forecast models. Data quality and specifics on derivation of sea-state parameters from raw wave data are important issues, but outside the scope of this thesis. Regardless of spectral assumptions and sea-state parameter choices, the 'slow-tuning' methodology presented here is applicable. The maximization of power capture as a function of $c_g$ and $m_4$ can be viewed as a classic optimization problem.

The section titled "A Complete Three-Body System" beginning on page 7 of Appendix B describes how a set of optimization codes, built on the Sequential Quadratic Programming algorithm provided by Matlab, were developed during the course of this research to search for a schedule of optimal generator damping-rotational inertia pairings across the frequency domain. The code development was done using the following basic steps. First, a parametric solution to the heave constrained dynamics model in the frequency domain was obtained using the analytical mathematics package Maple. By manipulating the analytical solution, an expression for power capture in terms of fixed WEC specifications and the control variables $c_g$ and $m_4$ was obtained.

Next, the optimization was setup to maximize the power capture expression, given by Equation (20) of Appendix B, as a function of the control variables. To ensure relative displacements between the float and spar as well as between the reaction-mass and spar are always kept within feasible limits, nonlinear constraints were included in the optimization problem. These constraints, sometimes referred to as "end-stop" limits, are extremely important considerations for the survivability of WECs. Maple was used to find the analytical gradients of the objective function with respect to control variables and nonlinear constraints. When supplied to the optimization algorithm, the analytical gradient expressions significantly improved the speed and accuracy of convergence.

Since the optimization algorithm is applied to maximize power at a single wave frequency, the process is iterated over the range of wave frequencies of interest. After convergence has been achieved at all wave frequencies, the outputs are the optimized power capture as a function frequency (given by Figure 3.4) and a set of optimal control schedules (given by Figure 3.5) which specify the optimal value of each control variable at each wave frequency, $c_g^*(\omega)$ and $m_4^*(\omega)$.

## 3.6 Results and Discussion

The power capture improvement afforded by the frequency response tuning system is shown in Figure 3.4 to approach a maximum of 80% at 1.5 rad/s when compared to a two body system of equivalent mass. The benefits in power capture illustrated by Figure 3.4 made possible by the control scheduling summarized in Figure 3.5 are subject to the following

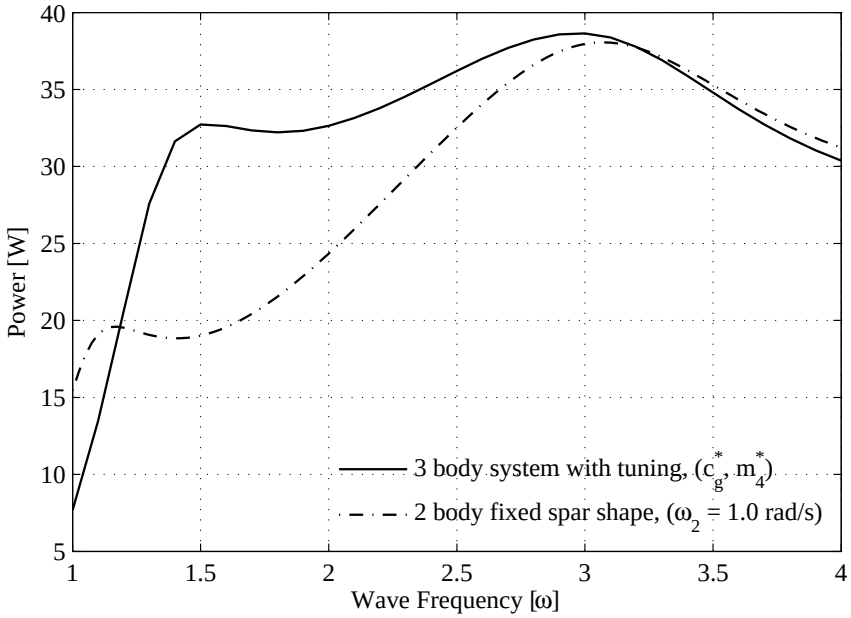


**Figure 3.4:** Power capture comparison for two WEC examples. 3-Body WEC with optimized generator damping, $c_g^*(\omega)$, and inertial control parameter $m_4^*(\omega)$ vs. 2-Body WEC with optimal $c_g^*(\omega)$ only. The 3-Body WEC is mass-equivalent to the 2-Body WEC.

two design constraints. First, the float diameter, and therefore its hydrostatic stiffness, $k_1$, was set for the wave tank (IOT) wave frequency range to not violate the small body approximation at the highest wave frequencies. However, at ocean scale, where wavelengths are from 100-500 meters, the small body approximation is not as critical. Increasing the float natural frequency relative to the spar natural frequency enables greater power capture by increasing the relative float-spar response, $\hat{\xi}_{1/2}$. Second, motivated out of caution to represent realistic results, the inertia control range in the work of Appendix B was limited arbitrarily at the high end. However, as a result of recent mechanical design activities [24] investigating possible ranges with feasible mechanical design techniques, the upper limit of the inertia control range was increased. In Figure 3.5, the optimized inertial control parameter is seen to be at its upper limit for much of the frequency domain—indicating that relaxing the upper inertial control limit would allow the optimization to converge on a more optimal objective.

Although not explicitly discussed in Appendix C, the two design constraints (float natural frequency and inertial control upper limits) have been modified in the WEC design and control for the next chapter of this thesis.

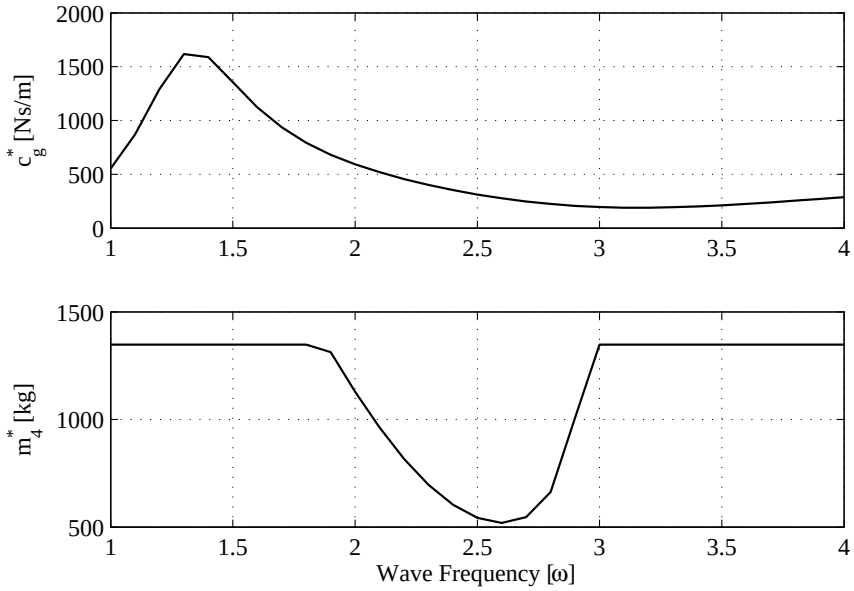


**Figure 3.5:** Example optimal control variables from a wave tank specific WEC design.

## 3.7 Summary

The parametric design approach undertaken in Appendix B distills the physical design of the spar into parametric expressions in terms of desired heave natural frequency. A sensitivity study shows spar natural frequency adjustments yielded distinct benefits, but these spar frequency adjustments were affected by physically impossible hull geometry changes. An internal tuning system was used to synthesize the frequency adjustments while keeping the hull geometry constant, and large power capture benefits at the low end of the frequency range are seen when inertial tuning system is used in combination with generator tuning. The next chapter applies the modeling and control techniques developed here for the frequency response tuning system to estimate power capture of a large scale WEC.

## Chapter 4

# A Full Scale Wave Energy Converter

This chapter summarizes the integration of a WEC in an isolated electric gird. The details of this work are reported in a manuscript included as Appendix C. The goal of this study is to evaluate the feasibility of providing electricity from a large scale WEC to a remote Alaskan community. The community, located on St. George Island, which is located roughly 500 kilometers North of the Aleutian island chain in the Bering Sea, has approximately 100 inhabitants and is reliant on diesel generators for electricity. Known in the past for its commercial fur seal harvest, St. George Island is now host to predominantly commercial fishing and eco-tourism activities.

To meet the study goal, a resource assessment was done using archived US National Oceanographic and Atmospheric Administration's (NOAA) Wavewatch3 Alaskan Waters model [25] parameter data. To evaluate the power capture of the WEC in irregular waves, additional relationships were used to allow the dynamics model and control methodology, as developed in the previous chapters, to handle realistic sea states with multiple wave frequencies and directions. The assumptions made in applying control schedules derived for regular waves to the irregular wave field are discussed. The island's electrical system, driven by diesel-electric generators, is described. Lastly, the feasibility of integrating the WEC into the island electrical system is assessed in terms of grid penetration measures and estimated fuel savings.

## 4.1 Wave Resource Assessment

Since the most logical deployment location, for reasons discussed in Section 2.1 of Appendix C, is to the South-West of the island, the island itself would "shelter" the WEC from waves approaching from the North-East. However, the NOAA Watchwatch3 model grid does not resolve the effects of small land masses such as St. George Island. Therefore, as a crude method of accounting for the blockage effects due to the island, the hourly records of significant wave height, $H_s$, peak period, $T_p$, and peak direction, $H_{dir}$, from the NOAA Wavewatch3 were post-processed to attenuate sea states with primary directions that fall in the directional range indicated by Figure 2 of Appendix C. Although the number of attenuated records comprises 37% of the dataset, the most frequently occuring and energetic seas remained unaffected by postprocessing, as indicated by Figure 3 of Appendix C.

In this integration study, the Pierson-Moscowitz spectrum, which is completely defined by the $H_s$ and $T_p$ pair, was chosen. The sea is assumed to be fully developed, the WEC is assumed to be in deep water, and the sea-state is assumed stationary over the hour for which Wavewatch3 parameters were recorded. The WEC is assumed to be directionally independent so an omni-directional spectrum can be used. The prevailing sea state, as identified by the joint probability contour plot in Figure 4 of Appendix C, is $(H_s, T_p) = (1.1\text{m}, 6.1\text{sec})$. The mean incident wave power over three years of directionally screened data, calculated by Equation (7) of Appendix C, is estimated to be between 26 kW/m and 28 kW/m for the deployment site.

## 4.2 Large Scale WEC Design

Recent full-scale WEC development activities [24] have resulted in design changes to the WEC. First, to raise the natural frequency of the float as high as possible, the float has been modified. Previously composed of a series of vertical cylinders, the float is now a toroidal shape. Second, a hydraulic PTO system has been chosen—enabling power smoothing with gas accumulators. Third, the design work on the frequency response tuning system has defined the upper and lower limits in the inertial control. A drawing of the latest WEC design is shown in Figure 4.1. Specifications for the full scale WEC device used in the study given by Appendix C, taken from recent full-scale development activities [24], are

summarized in Table 4.1. The specifications were used in the three DOF dynamics model

**Table 4.1:** Summary specifications of the large scale WEC

| Parameter | Value |
|---|---|
| Mass of structure | 166,000 kg |
| Outer diameter | 5 m |
| Draft | 30 m |
| Capacity | 100 kW |

and control optimization developed in Chapter 3 of this thesis to produce generator and rotational inertia control schedules with non-linear 'end-stop' constraints enabled. Application of the constraints ensures that power capture results do not reflect scenarios where the relative displacements between heaving bodies violate mechanical design limitations. One important limitation is the maximum stroke length for the hydraulic PTO pistons which is established from the consideration of potential buckling failure in the piston rods.

## 4.3 WEC Power Capture in Irregular Waves

The three DOF frequency domain model has been used to predict and optimize power capture assuming regular sinusoidal waves. A more realistic approximation to the ocean surface uses a superposition of multiple wave components—a spectral approach. The following additional steps to the three DOF frequency domain model and optimization routines were made to accommodate a spectral representation of the incident waves.

1. A two dimensional gridded 'sea state' space was setup, ranging over $0.5 \leq H_s \leq 8.5$ meters of significant wave height and ranging over $0.393 \leq \omega_p \leq 1.26$ rad/s of peak frequency which corresponds to $5 \leq T_p \leq 16$ seconds in peak period.

2. Optimal control schedules, $c_g^*(H, \omega), m_4^*(H, \omega)$, were interpolated at each $(H_s, \omega_p)$ pairing, yielding the control decisions for each sea-state, $c_g^*(H_s, \omega_p), m_4^*(H_s, \omega_p)$.

3. For calculation of the relative float-spar response to irregular waves of multiple frequency components, a spectral frequency domain was setup. The chosen number of frequency components was $N = 256$ and the chosen range was $0 < \omega_i \leq 3.2$ rad/s.

4. By applying control decisions $c_g^*(H_s, \omega_p), m_4^*(H_s, \omega_p)$, the relative float-spar response $\hat{\xi}_{1/2}(\omega, c_g^*(H_s, \omega_p), m_4^*(H,\omega_p))$ to a wave of unit amplitude is obtained from the dy-

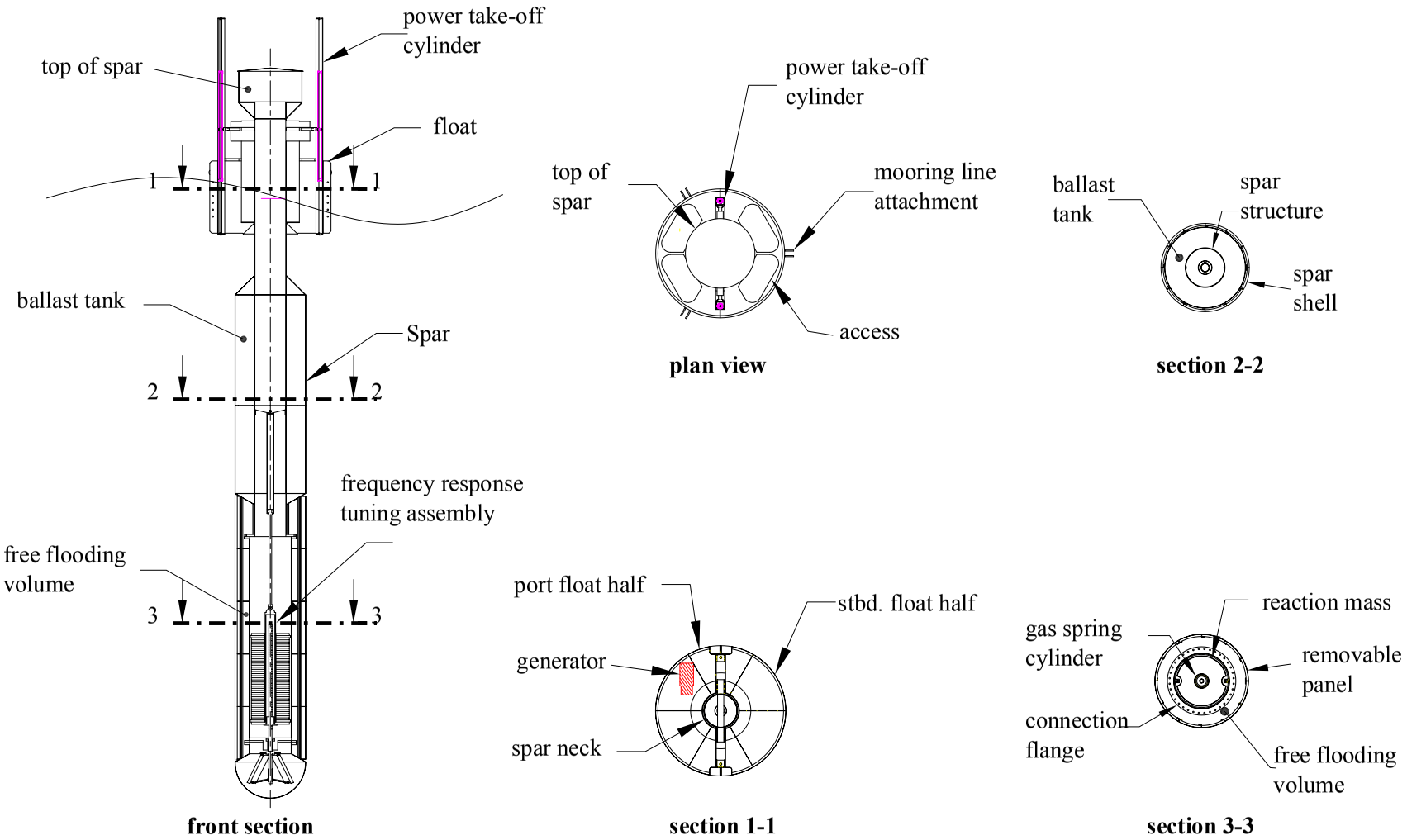


**Figure 4.1:** A drawing of the full scale WEC design (adapted from [24] with permission from Jim Adamson). Note the double acting hydraulic cylinders used for power take-off and the toroidal float shape represent the main advancements from previous iterations of the WEC design.

namics model solution over the spectral frequency domain. Referred to as a Response Amplitude Operator (RAO), $\frac{\hat{\xi}_{1/2}(\omega_i)}{A}$ or $H(\omega_i)_{1/2}$ is a linear transfer function between an incident wave component of frequency, $\omega_i$, and amplitude, $A$, and the float-spar relative displacement.

Inherent to the dynamics model is the assumption of heave displacements of small amplitude so that the principle of linear superposition applies. Consistent with previous assumptions, linear superposition is applied so that the power associated with each of the $N$ wave components is summed. The resulting equation for the mean power in irregular waves is given by Equation (4.1)

$$\bar{P} = \frac{1}{2} c_g \sum_{i=1}^{N} \omega_i^2 |H(\omega_i)_{1/2}|^2 2S(\omega_i)\Delta\omega \tag{4.1}$$

Using Equation (4.1), power capture is calculated over ranges of both significant wave height and peak period. The WEC control system is assumed to have access to information about the incident wave spectrum. As discussed in Section 4.3 of Appendix C, The generator damping, $c_g$, and rotational inertia, $J$, are adjusted by interpolating optimal control schedules in the frequency domain at the peak frequency, $\omega_p$, of the incident waves. When the power capture is plotted as a colour contour surface or matrix (as given in Figure 8 of Appendix C ), it is commonly called a 'production matrix,' and is used by WEC device developers to report the performance of their device. Any set of archived wave data in the form of time series of $H_s(t)$ and $T_p(t)$ can the be used to form an estimate of the power capture by interpolating the production matrix.

## 4.4 Comparison of WEC power delivery to St. George Island Demand

The island of St. George, which is endowed with a plentiful wave resource relies on diesel electric generators with a total capacity of 900kW. The island's community electrical demand reaches its peak, about 300kW, in the dead of winter. Because of their wave resource, the flexibility of diesel generation, and their high cost of diesel fuel, the St. George Island community was deemed a great candidate for a feasibility study on the electrical integration of a full scale WEC. The case study is presented in detail in Appendix C.

Hourly sea state parameter data from the NOAA Wavewatch3 Alaskan Waters model over three years starting January 2004 was used to interpolate the WEC production matrix to yield an hourly estimate of wave power capture. Next, the WEC power capture was compared in detail with an estimated hourly community load calculator [26].

Power penetration, as defined by Equation (4.2), was computed hourly and shown in Figure 4.2 for the three year data set.

$$\text{Power penetration} = \frac{\text{Instantaneous power delivered by WEC [kW]}}{\text{Instantaneous power demand [kW]}} \tag{4.2}$$

The highest penetration ratios of each year are shown by Figure 4.2 to be from 100%

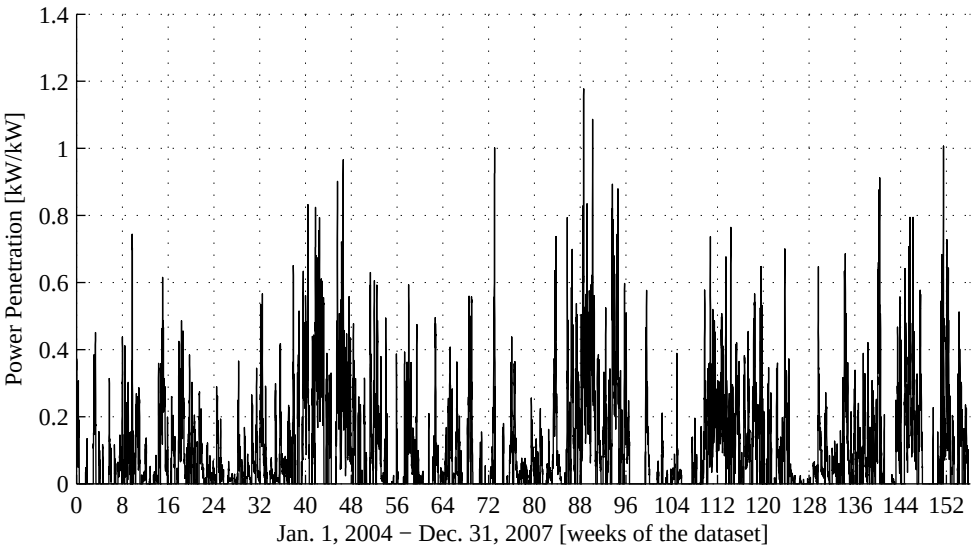


**Figure 4.2:** Hourly power penetration—the ratio of the WEC power delivery to community electrical power demand for the case study of Appendix C.

to 120%. The highest penetration ratios occur in the fall seasons where the WEC power capture is at a maximum due to large swell from fall storms, but the electrical power demand has not yet reached its peak of the season. Further discussions on grid penetration are given in Section 6.3 of Appendix C. Assuming that WEC power can simply offset diesel generation at all times, the average yearly wave energy delivered to the grid is 122MWh and the estimated fuel savings is 61,800 litres. Using the 2007 diesel fuel cost to St. George island, the approximate yearly fuel cost savings is estimated at 81,600 US dollars.

## 4.5 Summary

This chapter summarized the feasibility study of the electrical integration of a full-scale WEC design with the island of St. George, given by the manuscript in Appendix C. First, a resource assessment was done using archived Wavewatch3 parameter data. A spectral approach was utilized to enable the calculation of power capture in irregular waves using the frequency domain dynamics model and control methodology from Chapter 3. Comparison of the estimated *in situ* WEC power delivery to the St. George Island electrical demand reveal patterns in the seasonal behavior of grid penetration levels as well as estimates of the magnitudes of penetration levels. Using a simplified power management strategy, estimated yearly fuel savings and fuel cost savings offer some indication of the economic constraints of the project.

## Chapter 5

# Conclusions

The goal of the research presented was to advance the development of a 'self-reacting' point absorber WEC. An experimental two body prototype was designed and tested in a wave tank. Although the power capture test results contained significant scatter, they compare reasonably well to power estimates using a two DOF linear model in the frequency domain. A parametric spar model was developed to completely define the external geometry of the spar by its natural frequency. Further, to investigate the potential benefits to frequency response tuning, the parametric spar model was used for a sensitivity of power capture to spar natural frequency. Results of the sensitivity study indicated distinct benefits if the spar natural frequency could be tuned. Subsequently conceptual design of a novel mechanism for spar frequency response tuning system was presented. The two DOF linear model was then expanded to represent the WEC with frequency response tuning as a three DOF system. An optimization algorithm was used to compute recommended schedules for the adjustment of the available control parameters to maximize power capture. The theory of floating body motions in irregular waves was applied to the three DOF frequency domain model with optimal control in order to estimate power capture of an example large scale WEC design at a remote Alaskan location using archived Wavewatch3 model data. Lastly the results from the case study on the integration of a full scale WEC with the remote island electrical system indicated that high grid penetration levels due to the variability of wave power generation could be technically managed using strategies from the field of wind-diesel hybridization. Lastly, substantial diesel fuel cost savings were estimated based on a simplified power management scheme.

## 5.1 Conclusions

1. A heave constrained linear dynamics model in the frequency domain can be used with reasonable accuracy to estimate power capture in regular waves of the WEC.

2. Analytical solutions to linear dynamics models enable the efficient use of Sequential Quadratic Programming algorithms to maximize power capture of WEC's with non-linear travel constraints.

3. An internally housed, spring supported reaction mass coupled to a rotational system with variable inertia can be effectively used to tune the frequency response of a heaving body. In the case of the heaving point absorber WEC in this thesis, significant power capture improvements are expected with the use of the tuning system.

4. A single full-scale WEC could represent a technically and economically feasible solution offset diesel generated electricity for St. George Island and other remote coastal communities.

## 5.2 Future Work

There are many areas to continue and enhance the research presented here:

1. Improve the fidelity of the hydrodynamic coefficients of the WEC in the existing dynamics model, including hydrodynamic cross-coupling effects, so that changes in hydrodynamic coefficients due to external geometry changes can be effectively modeled for future design optimization exercises.

2. Investigate the implementation of a 'fast-tuning' or 'wave-to-wave' control of the inertia and generator damping using accurate wave field and/or WEC dynamics information to maximize power capture to a much higher degree.

3. Design and test a second WEC model in a wave tank in both regular and irregular wave conditions. The WEC would be fitted with a working frequency response control system. A full suite of design features, learned from wave tank testing experience gained in this thesis, to improve experimentation work would be implemented.

4. Develop a multiple objective design optimization procedure. Increase the utility of the design parameterization by including pitch and roll stability constraints which would have effects on the distribution of mass of the WEC. Design variables would be critical parameters such as the undamped natural frequencies of the float and spar. Stochastic based optimization methods such as Genetic Algorithms or Simulated Annealing might be best suited to the problem because the objective function is expected to not be a smooth function of the design variables.

5. The frequency response tuning system is sensitive not only to the inertial control parameter, $m_4$, but also the spring support stiffness, $k_3$. If a suitable variable stiffness mechanism could be obtained or designed, the addition of $k_3$ as a third control variable holds promise of significant control leverage and associated increases of power capture. A further project could be initiated to evaluate the feasibility and performance benefits of variable-stiffness mechanisms.

6. Implement a time-domain power system model of the St. George Island integration case. This would allow a more accurate evaluation of the energy and fuel savings by including diesel generator minimum loads, maximum ramp rates, and optimal power management strategies in the analysis.

# Bibliography

[1] J. Falnes, "A review of wave-energy extraction," *Marine Structures*, vol. 20, pp. 185–201, Oct. 2007.

[2] A. Cornett, "Inventory of canada's marine renewable energy resources," Tech. Rep. CHC-TR-041, National Research Council - Canadian Hydraulics Centre, Ottawa, K1A 0R6, Canada, April 2006.

[3] M. French, "On the difficulty of inventing an economical sea wave energy converter: a personal view," *Proceedings of the I MECH E Part M Journal of Engineering for the Maritime Environment*, vol. 220, no. 3, pp. 149–155, 2006.

[4] A. Weinstein, G. Fredrikson, L. Claeson, J. Forsberg, M. J. Parks, K. Nielsen, M. S. Jenses, K. Zandiyeh, P. Frigaard, M. Kramer, and T. L. Andersen, "Aquabuoy - the offshore wave energy converter numerical modeling and optimization," in *Oceans Conference Record (IEEE)*, vol. 4, (San Diego, CA., United states), pp. 1988–1995, Institute of Electrical and Electronics Engineers Inc., 2003.

[5] M. Draper, "More than just a ripple: Ocean power technologies sets its sights high," *Refocus*, vol. 7, no. 1, pp. 54–56, 2006.

[6] R. Taghipour and T. Moan, "Efficient frequency-domain analysis of dynamic response for the multi-body wave energy converter in multi-directional waves," in *Proceedings of the Eighteenth (2008) International Offshore and Polar Engineering Conference, Vancouver, BC, Canada*, July 2008.

[7] R. H. Bracewell, *Frog and PS Frog: A Study of Two Reactionless Ocean Wave Energy Converters*. PhD thesis, Lancaster University, September 1990.

[8] A. Babarit, A. Clement, J. Ruer, and C. Tartivel, "SEAREV : A fully integrated wave energy converter," in *Proceedings of the 2006 Offshore Wind And Other Marine Renewable Energies In Mediterranean And European Seas*, Offshore Wind And Other Marine Renewable Energies In Mediterranean And European Seas, OWEMES, April 2006.

[9] M. Tucker and E. Pitt, *Waves in ocean engineering*, vol. 5 of *Elsevier ocean engineering book series*. Amsterdam, New York: Elsevier, 1st ed., 2001.

[10] J. Falnes, *Ocean Waves and Oscillating Systems: Linear Interactions including Wave Energy Extraction*, ch. 5.6 The Froude Krylov Force and the Small-Body Approximation, pp. 160–167. Cambridge University Press, 2002.

[11] J. Falnes, "Wave-energy conversion through relative motion between two single-mode oscillating bodies," *Journal of Offshore Mechanics and Arctic Engineering*, vol. 121, no. 1, pp. 32–38, 1999.

[12] G. Clauss, E. Lehmann, and C. Ostergaard, *Offshore Structures - Conceptual design and hydromechanics*, vol. 1. Springer-Verlag, 1992.

[13] R. G. Dean and R. A. Dalrymple, *Water wave mechanics for engineers and scientists*, vol. 2 of *Advanced Series in Ocean Engineering*, book 8 Wave Forces, p. 218. World Scientific, 1991.

[14] J. Falnes, *Ocean Waves and Oscillating Systems: Linear Interactions including Wave Energy Extraction*. Cambridge University Press, 2002.

[15] R. Dugas and J. R. Maddox, *A History of Mechanics*. Courier Dover Publications, illustrated ed., 1988.

[16] P. Rudnick, "FLIP: An oceanographic buoy," *Science*, vol. 146, no. 3649, pp. 1268–1273, 1964.

[17] G. A. Nolan, J. V. Ringwood, W. E. Leithead, and S. Butler, "Optimal damping profiles for a heaving buoy wave energy converter," *15th International Offrshore and*

*Polar Engineering Conference, ISOPE-2005, Jun 19-24 2005*, vol. 2005, pp. 477–484, 2005.

[18] G. Duclos, A. Babarit, and A. H. Clement, "Optimizing the power take off of a wave energy converter with regard to the wave climate," *Transactions of the ASME. Journal of Offshore Mechanics and Arctic Engineering*, vol. 128, no. 1, pp. 56–64, 2006.

[19] DeBacker, V. Banasiak, Beels, and D. Rouck, "Numerical modelling of wave energy absorption by a floating point absorber system," in *Proceedings of the Sixteenth (2007) International Offshore and Polar Engineering Conference Lisbon, Portugal, July 1–6, 2007*, ISOPE, 2007.

[20] A. Babarit, G. Duclos, and A. Clement, "Comparison of latching control strategies for a heaving wave energy device in random sea," *Applied Ocean Research*, vol. 26, pp. 227–238, July 2004.

[21] T. Mundon, A. Murray, J. Hallam, and L. Patel, *Causal Neural Control of a Latching Ocean Wave Point Absorber*, vol. 3697/2005 of *Lecture Notes in Computer Science*, pp. 423–429. Springer Berlin / Heidelberg, 2005.

[22] A. Babarit and A. Clement, "Optimal latching control of a wave energy device in regular and irregular waves," *Applied Ocean Research*, vol. 28, pp. 77–91, Apr. 2006.

[23] F. Tedd, "Short term wave forecasting, using digital filters, for improved control of wave energy converters," in *Proceedings of the Sixteenth (2007) International Offshore and Polar Engineering Conference Lisbon, Portugal, July 1-6, 2007*, ISOPE, 2007.

[24] S. Beatty, C. Hiles, R. Nicoll, J. Adamson, and B. J. Buckham, "Design synthesis of a wave energy converter," in *28th International Offshore Mechanics and Artic Engineering Conference*, (Honolulu Hawaii), May-June 2009. In Review.

[25] "National Oceanic and Atmospheric Administration WaveWatch III." `http://polar.ncep.noaa.gov/waves/index2.shtml`, Accessed May 5th, 2008.

[26] M. Devine and E. Baring-Gould, "The Alaska Village Electric Load Calculator," Tech. Rep. NREL/TP-500-36824, U.S. Department of Energy, National Renewable Energy Laboratory, Golden, Colorado, October 2004.

# Appendix A

# Modeling, Design and Testing of a Two-Body Heaving Wave Energy Converter

# Modeling, Design and Testing of a Two-Body Heaving Wave Energy Converter

*Scott J. Beatty, Bradley J. Buckham, Peter Wild*
Department of Mechanical Engineering, University of Victoria.
Victoria, B.C., Canada

ABSTRACT

**A small scale point absorber was constructed and tested in September 2006. The tests were aimed at performance characterization and validation of a linear dynamics model in the frequency domain. The coefficients used in the model are obtained through a combination of bench-top and tank-side experiments. The device produced an average of 5.5 W from waves of 19 cm height and frequencies between 0.35 and 0.65 Hz. The experimental results compare reasonably well with the frequency domain dynamics model. However, there is a significant amount of scatter in the experimental values which was attributed to various sources.**

KEY WORDS: Wave energy; point absorber; heaving buoy

NOMENCLATURE

| | |
|---|---|
| $a$ | prototype half-length in wave propagation direction |
| $a_{gen}$, $b_{gen}$ | generator constants |
| $\hat{a}_{0j}$ | fluid acceleration due to incident wave at $z_{pj}$ |
| $b_{jj}$ | radiation damping coefficient for body j |
| $c_{gen}^{\xi}$ | generator damping coefficient based on $\dot{\xi}_{1/2}$ |
| $c_{gen}^{\theta}$ | generator damping coefficient based on $\dot{\theta}_{gen}$ |
| $c_j$ | total damping coefficient of body j |
| $c_{loss}$ | damping coefficient due to frictional losses |
| $c_{vj}$ | viscous damping coefficient of body j |
| $d$ | half-width normal to wave propagation direction |
| $\vec{f}_e$ | wave excitation force |
| $h$ | tank depth |
| $k$ | wave number |
| $k_j$ | buoyancy stiffness of body j |
| $m_j$ | physical mass of body j |
| $m_{jtot}$ | total mass of body j |
| $m_{11}$, $m_{22}$ | added mass coefficients |
| $\hat{v}_{0j}$ | fluid velocity due to incident wave at $z_{pj}$ |
| $x$, $y$, $z$ | body fixed Cartesian coordinates (see Fig. 1) |
| $x_{Pj}$, $y_{Pj}$, $z_{Pj}$ | reference point location of body j |
| $A$ | incident wave amplitude |
| $A_i$ | pillar cross sectional area at station i |
| $I_{PTO}$ | rotational inertia of the PTO system |
| $L$ | distance from float to tank wall |
| $P(t)$, $P(\omega)$ | mechanical power absorbed |
| $R_{int}$ | armature resistance of generator |
| $R_{ext}$ | external load resistance on generator |
| $T_j$ | draft of body j |
| $\varepsilon_j$ | phase angle of body j |
| $\eta(x,t)$ | incident wave elevation |
| $\theta_{gen}$ | angular position of generator shaft |
| $\xi_j$ | heave displacement of body j |
| $\xi_{1/2}$ | displacement of body 1 relative to body 2 |
| $\tau(t)$ | torque applied to generator shaft |
| $\omega$ | wave frequency |
| $\omega_{nj}$ | natural frequency of body j |

## INTRODUCTION

Experiments with resonating "point absorbers" date back to Budal and Falnes (1975). In the numerical and experimental studies since that time, body geometries and kinematics have been adjusted to maximize the kinetic energy of the WEC that is subsequently harvested by some form of energy generator. The choice to work in multiple degrees of freedom, or use multiple bodies working in single degrees of freedom has been guided by theoretical work defining the response of floating bodies to wave forces. Srokosz and Evans (1979) considered the tuning of two independent oscillating bodies in regular sinusoidal waves. In their concept, a separate power take-off (PTO) is attached to

each body. By considering radiation, scattering, and hydrodynamic cross-coupling effects, they determined a capture width ratio of one. Bjarte-Larsson and Falnes (2006) studied control of point absorbers using a "latching" strategy consisting of an actively controlled nonlinear power take-off driven by oscillations of a single body. Falnes (1999) and Eidsmoen (1995) discussed modeling and control of a two-body point absorber - one submerged and one surface piercing. Weinstein et al. (2004) and Bracewell (1990) both developed concepts of a heaving point absorber utilizing a second body mounted inside a surface piercing housing. In this design variation, the power take-off is positioned between the internal oscillating body and its external housing.

The prototype two-body device being studied at the University of Victoria is shown schematically in Fig. 1. This device is similar to the device outlined schematically by Falnes (1999) except both bodies are surface piercing. The prototype is being used as a test-bed for the development of an internal tuning mechanism that can be used for two purposes: to broaden the useful bandwidth of an ocean going instantiation of the device, and to compensate for any non-ideal contributions to the wave excitation forces caused by design and operational constraints. In this work, the testing and characterization of the early prototype, affectionately known as Charlotte, is presented. The objectives of the experimental work presented are to establish Charlotte's baseline performance and to validate the numerical models being used in the design of the tuning system.

Fig. 1. The WEC prototype at the wave tank facility, Sept. 2006.

## WEC DESIGN CONCEPT

"Slack-mooring" has distinct advantages relative to tight mooring including enhanced ocean survivability, through minimization of stresses on mechanical components during extreme sea states, and natural tidal compensation. We have chosen to maintain slack mooring by extracting energy from the relative motion between two heaving bodies. To optimize this relative motion, and the resulting WEC output, each body is sized and shaped such that: resonance develops at targeted wave frequencies, good phase separation exists between the two bodies when forced at the predominant wave frequency, and/or the wave excitation forces for the two bodies are out of phase. The WEC considered in this work has two surface-piercing heaving bodies with the PTO placed between them (see Fig. 2). The current prototype is intended as a base-line system for validation of theoretical models, and thus the body geometries are kept as simple cylinders to simplify the parameter identification procedure. Charlotte is comprised of a central pillar surrounded by an arrangement of four cylinders referred to as the float. The power take-off is housed within the portion of the central pillar that pierces the free surface. In an initial design strategy, the diameters and masses of the pillar and float are chosen so that a resonant condition is achieved at both ends of the wave frequency range, thus ensuring that large relative motions, whether driven by one body or the other, are induced over the full frequency range. For Charlotte, the central pillar diameter and mass are set to yield a natural frequency at the low end of the wave tank capabilities (0.35 Hz) and the float is sized to yield a natural frequency at the high end (0.55 Hz). This *a priori* tuning of the device is to be complemented by the in-situ tuning step which seeks to optimize the phase separation of the pillar and float.

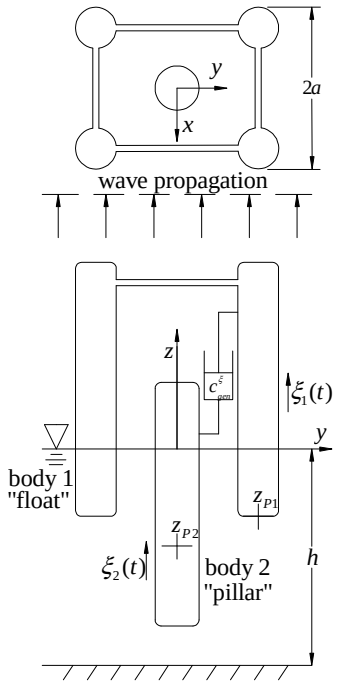


Fig. 2. The WEC with two separate heaving bodies generating energy by relative motion. Body 1 consists of four rigidly connected vertical cylinders. The power take-off is modeled as a linear dashpot.

### Design Constraints

The prototype design constraints were largely driven by the physical constraints of the planned test location given in Table 1. For the small body approximation to be applicable in the wave tank frequency range,

$$\max(ka) \ll 1 \quad (1)$$

Therefore length, parallel to the direction of wave propagation, *2a*, was chosen to be as small as possible while maintaining a pillar diameter that could accommodate the off-the-shelf power take off components and instrumentation. Given the tank depth and frequencies listed in Table 1, the range of wave numbers (from the dispersion relation at

finite depth) is,

$$0.56 \text{ m}^{-1} \le k \le 2.26 \text{ m}^{-1} \quad (2)$$

The final design yields,

$$\max(ka) \le 0.54 \quad (3)$$

Table 1. Wave Tank Parameters

| Physical Parameter | Value |
|---|---|
| Depth (h) | 2.438 m |
| Width | 3.658 m |
| Wave Frequency Range ( $\omega/2\pi$ ) | 0.35 Hz $\le f \le$ 0.65 Hz |
| Wavelengths ( $2\pi/k$ ) | 2.78 m $\le \lambda \le$ 11.2 m |
| Maximum Wave Height (2*A*) | 0.254 m |

To keep the length 2*a* small with respect to the shortest wavelength, a directional geometry was used rather than an axisymmetric design. As shown in Fig. 4, the float spacing is smaller in the direction of the wave propagation. This non-axisymmetric float design was expected to cause some yaw instability or "weather-vaning" and so a two point mooring was attached to the outside of the pillar hull at a depth near the device center of gravity to constrain yaw rotation. Light weight nylon mooring lines (shown as dotted lines in Fig. 4) were tied off to a tank bridge located approximately 3m ahead of the model so that drift forces would be taken up by tension in the lines. The directional float geometry is not intended for future ocean going units. As the system is sized to an ocean environment the relative sizes of suitable power take-off components will decrease with respect to ocean scale wavelengths. This will allow for an axisymmetric float plan-form that easily satisfies Eq. 1.

The stability of Charlotte was improved using a mass extension at the bottom of the central pillar to increase the righting buoyant moment. Also, the center of the submerged volume was raised by using external buoyancy 'collars' to redistribute the submerged volume while maintaining the desired equilibrium draft. To ensure a linear buoyancy stiffness, the 'collars' were placed so as not to pierce the water surface during expected heave motion. The flotation collars, seen just below the waterline in Fig. 1 and more clearly in the schematic of Fig. 4, had significant effects on the hydrodynamic properties of the pillar, as will be discussed in the following sections.

**Charlotte Design**

The final design is summarized in Table 3 and shown in Figs. 3 and 4. The mass extension, visible at the bottom of the device, cleared the tank bottom by less than 0.5 m. The flotation collar is the bulbous attachment on the pillar located at the same draft as the float. Stainless steel rails, mounted on flexures, guide the float travel along the pillar.

**Power Take off and Instrumentation**

To provide a nominal capability to produce electricity, a simple brush-commutated DC generator was chosen as the PTO damper. The generator is mounted on a plate inside the dry section of the pillar assembly. The generator is belt driven by the shaft of the top sprocket of an external chain drive such that linear motion of the float along the pillar causes rotation of the generator shaft. This relative travel is kinematically related to the generator rotation by:

$$\dot{\xi}_{1/2}(t) = \frac{r_{spr}}{4}\dot{\theta}_{gen}(t) \quad (4)$$

As shown in Fig. 3, a load cell is used to support the vertical mounting plate as the driving torque is applied by the top sprocket shaft. The relative motion of the float along the pillar, $\dot{\xi}_{1/2}(t)$, was captured using a rotational encoder on the generator shaft, $\dot{\theta}_{gen}(t)$.

Table 3. WEC Prototype Design Parameters

| Physical Parameter | Value |
|---|---|
| Prototype horizontal width (2d) | 1.120 m |
| Prototype horizontal length (2a) | 0.636 m |
| Float Buoyancy Stiffness ($k_1$) | 1479 N/m |
| Float Draft ($T_1$) | 0.762 m |
| Float Mass ($m_{1\text{tot}}$) | 128.5 kg |
| Float Damping ($c_1$) | 120.6 Ns/m |
| Float Natural Frequency ($\omega_{n1}$) | 0.540 Hz |
| Pillar Buoyancy Stiffness ($k_2$) | 612.4 N/m |
| Pillar Draft ($T_2$) | 1.97 m |
| Pillar Mass ($m_{2\text{tot}}$) | 179.5 kg |
| Pillar Damping ($c_2$) | 270.1 Ns/m |
| Pillar Natural Frequency ($\omega_{n2}$) | 0.294 Hz |
| Generator Damping ($c_{\text{gen}}$) | ~115 Ns/m |

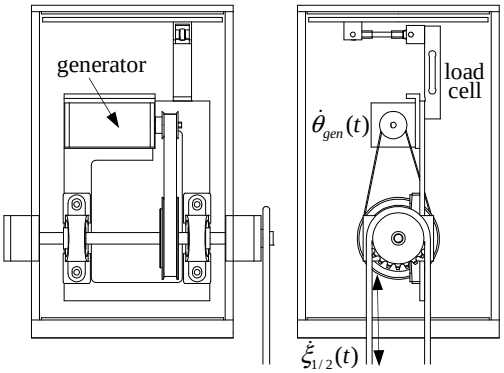


Fig. 3. Two views of the power take off unit. The dynamometer assembly, which measures the generator reaction forces using a load cell, is also shown.

As shown by Graves (2000), a simple DC generator can be modeled as a rotational dashpot with inductive torque linearly proportional to angular velocity. Using this model, the driving torque delivered by the input shaft is related to the load cell measurement through a single degree of freedom differential equation:

$$\tau(t) = I_{PTO}\ddot{\theta}_{gen}(t) + c^{\theta}_{gen}\dot{\theta}_{gen}(t) \quad (5)$$

As described in the following sections, the inertia $I_{PTO}$, of the power take off assembly is very small and can be neglected in the calculation of the driving torque and hence:

$$\tau(t) \simeq c^{\theta}_{gen}\dot{\theta}_{gen}(t) \quad (6)$$

## MODELLING

A simplified dynamics modeling strategy is currently being used in the development of the in-situ tuning mechanism for Charlotte. Each body is modeled as a linearized single degree of freedom system in heave. Consistent with an ideal wave tank environment, a regular sinusoidal wave excitation is considered.

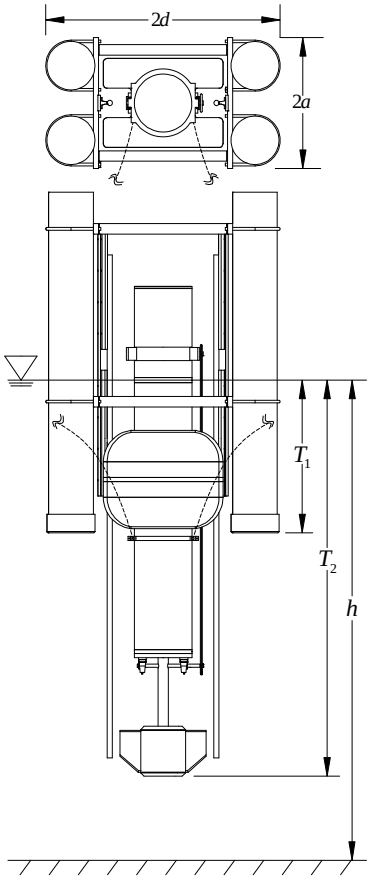


Fig. 4. The WEC prototype design.

**Dynamics Equations**

The Charlotte model is a system of two coupled ordinary differential equations with constant coefficients assembled in matrix form.

$$\underline{M}\ddot{\vec{x}} + \underline{C}\dot{\vec{x}} + \underline{K}\vec{x} = \vec{f}_e \tag{7}$$

The mass matrix, damping matrix, stiffness matrix, and the system displacement vector are given in Eqs. 8 through 11 respectively. The heave displacement of each body is given by $\vec{x}$. The wave excitation term is denoted by $\vec{f}_e$. The equations are coupled by the damping coefficient, $c_{gen}^{\xi}$, defining the viscous effects of the power take off generator and an additional viscous coefficient, $c_{loss}$, that quantifies the mechanical losses of the chain drive. The damping coefficient, $c_{gen}^{\xi}$, is related to the generator damping coefficient presented in Eq. 12 by the kinematics of the chain drive and the PTO assembly. To summarize:

$$\underline{M} = \begin{bmatrix} m_{1tot} & 0 \\ 0 & m_{2tot} \end{bmatrix} \tag{8}$$

$$\underline{C} = \begin{bmatrix} c_1 + c_{gen}^{\xi} + c_{loss} & -c_{gen}^{\xi} - c_{loss} \\ -c_{gen}^{\xi} - c_{loss} & c_2 + c_{gen}^{\xi} + c_{loss} \end{bmatrix} \tag{9}$$

$$\underline{K} = \begin{bmatrix} k_1 & 0 \\ 0 & k_2 \end{bmatrix} \tag{10}$$

$$\vec{x} = \begin{Bmatrix} \xi_1 \\ \xi_2 \end{Bmatrix} \tag{11}$$

$$c_{gen}^{\xi} = \frac{4}{r_{spr}^2} c_{gen}^{\theta} \tag{12}$$

The frequency dependence of the added mass and radiation damping terms has been neglected. In addition, the $c_1$ and $c_2$ values within the damping matrix are lumped coefficients that define the radiation damping experienced by the body in the presence of the other. We do not consider radiation forces induced on either body from motion of the other, and so

$$c_1 \approx c_{v1} + b_{11}(\omega_{n1}) \tag{13}$$

$$c_2 \approx c_{v2} + b_{22}(\omega_{n2}) \tag{14}$$

$$m_{1tot} \approx m_1 + m_{11}(\omega_{n1}) \tag{15}$$

$$m_{2tot} \approx m_2 + m_{22}(\omega_{n2}) \tag{16}$$

Where $c_{vj}$ is a viscous coefficient for body $j$ approximating hydrodynamic drag and $b_{jj}$ is the actual frequency dependent radiation coefficient for body $j$.

**Wave Excitation Force Model**

For a forward propagating sinusoidal plane wave with amplitude $A$, the complex representation of the wave elevation can be expressed as follows,

$$\eta(x,t) = Ae^{-ikx}e^{i\omega t} \tag{17}$$

An approach utilizing the 'small body' or 'long wavelength' approximation, suggested by Falnes, Johannes (2002), is used for the heave excitation force model. Since the effects of variations in fluid potential over the width of both components are neglected, the fluid velocities and accelerations are evaluated at a single reference point for each body. In the local level plane, these reference points are located at:

$$x_{P1} = x_{P2} = 0 \tag{18}$$

$$y_{P1} = y_{P2} = 0 \tag{19}$$

Hence, the wave elevation used to calculate the excitation is:

$$\eta(x,t) = Ae^{i\omega t} \tag{20}$$

To complete the reference point definitions for the float and pillar a reference depth for each body is required. The reference depth for the float is chosen as the bottom surface, $z_{P1} = T_1$, since it is the only exposed area perpendicular to the heave direction. As shown in Fig. 5, there are many horizontal areas on the pillar that interact with the vertical fluid motions of the incident waves. The pillar reference depth, $z_{P2}$, was determined as a weighted average of the depths of all protruding surface areas perpendicular to the heave direction:

$$z_{P2} = \frac{\sum_{i=1}^{7}\left(\frac{A_i}{A_0}\right) z_i}{\sum_{i=1}^{7}\left(\frac{A_i}{A_0}\right)} \tag{21}$$

where the station depths, $z_i$, and area ratios used are given in Table 2

and shown in Fig. 5. The final reference depth values used are $z_{P1} = 0.762\text{m}$ and $z_{P2} = 0.846\text{m}$.

Table 2. Geometry of body two used to determine reference depth.

| (i) | Station depth ($z_i$) | Area ratio ($A_i/A_0$) |
|---|---|---|
| 0 | 0.00 m | 1.00 |
| 1 | -0.29 m | 0.47 |
| 2 | -0.44 m | 2.32 |
| 3 | -0.62 m | 2.32 |
| 4 | -0.77 m | 0.47 |
| 5 | -1.39 m | 1.00 |
| 6 | -1.73 m | 0.60 |
| 7 | -1.97 m | 0.60 |

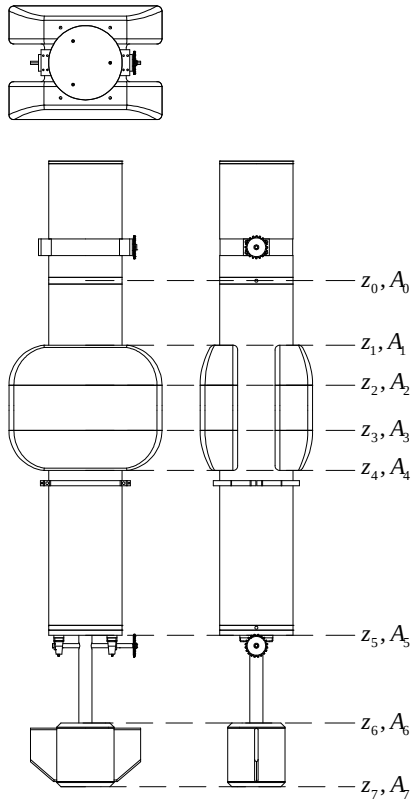


Fig. 5. The depth stations and cross sectional areas used to determine body 2 (pillar) reference depth.

The complex amplitudes of the fluid accelerations and velocities, evaluated at the reference locations for each body are expressed in Eq. 22 and Eq. 23, respectively. Given the shallow depth of the tank, the hyperbolic envelope on the water particle trajectories was applied.

$$\hat{a}_{0j} = -\omega^2 \frac{\sinh(kz_{Pj} + kh)}{\sinh(kh)} A \tag{22}$$

$$\hat{v}_{0j} = i\omega \frac{\sinh(kz_{Pj} + kh)}{\sinh(kh)} A \tag{23}$$

The excitation force in Eq. 7 becomes

$$\vec{f}_e = \left[ \begin{pmatrix} m_{1tot}\hat{a}_{01} \\ m_{2tot}\hat{a}_{02} \end{pmatrix} + \begin{pmatrix} c_1\hat{v}_{01} \\ c_2\hat{v}_{02} \end{pmatrix} + \begin{pmatrix} k_1 \\ k_2 \end{pmatrix} A \right] e^{i\omega t} \tag{24}$$

**Power Estimation**

The heave displacements of the Charlotte pillar and float are defined using complex representation. Assuming a steady field of incident waves, the body motions, well removed from the start of the test, should follow:

$$\xi_j(t) = \text{Re}\{\hat{\xi}_j e^{i\omega t}\} \tag{25}$$

where $\hat{\xi}_j$ is the complex amplitude of the oscillations and includes magnitude and phase information. Inserting Eqs. 22 - 24 into Eq. 7, Charlotte's frequency response function can be calculated:

$$[-\omega^2 \underline{M} + i\omega \underline{C} + \underline{K}] \begin{Bmatrix} \hat{\xi}_1 \\ \hat{\xi}_2 \end{Bmatrix} = \left[ \begin{pmatrix} m_{1tot}\hat{a}_{01} \\ m_{2tot}\hat{a}_{02} \end{pmatrix} \frac{1}{A} + \begin{pmatrix} c_1\hat{v}_{01} \\ c_2\hat{v}_{02} \end{pmatrix} \frac{1}{A} + \begin{pmatrix} k_1 \\ k_2 \end{pmatrix} \right] A \tag{26}$$

Given a incident wave frequency and amplitude, Eq. 26 is solved for the pillar and float magnitude and phase. The predicted mechanical input into the power take off assembly, or average power as a function of frequency is:

$$P(\omega) = \frac{1}{2}\omega^2 c_{gen} \left| \hat{\xi}_{1/2} \right|^2 \tag{27}$$

where,

$$\hat{\xi}_{1/2}(\omega) = \hat{\xi}_1(\omega) - \hat{\xi}_2(\omega) \tag{28}$$

## PARAMETER IDENTIFICATION

The physical model parameters were estimated using motion data collected during free oscillation of the prototype device in undisturbed water, and during bench-top operation of the power take off assembly.

**Hydrodynamic Coefficients**

In the still water tests, the float and pillar were subjected to initial deflections and released. In each test, the other body was clamped in place to isolate the radiation effects strictly due to each body's own motion. Referring to Eq. 7, if the other body is held fixed and the water is still ( $A = 0$ ), the predicted motion of the float, or pillar, reduces to a under-damped second order response. As shown in Fig. 6, the response of each body to an initial heave deflection follows this prediction, and approximate values of the total body mass (including added mass) and the viscous coefficient can be extracted using a classic log-decrement technique.

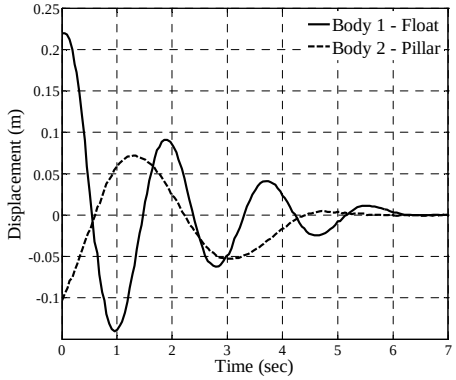


Fig. 6. Transient responses of the float and pillar during still water tests

(both with the power take-off disconnected).

Several tests were conducted for the float to determine the hydrodynamic effects, the generator damping and the mechanical losses. In the first test, the chain drive was disconnected to isolate the contribution of $c_1$. In the second test, the chain drive and power take off were connected, but the generator circuit was opened. These tests isolated the viscous effects due to $c_1$ and $c_{loss}$, respectively, and the coefficient $c_{loss}$ could, as a result, be determined. Holding the float stationary and displacing the pillar, the coefficient $c_2$ was calculated. Given that the frequency variation of the $c_1$ and $c_2$ coefficients was neglected, no external springs or masses were added to the pillar or float to vary the frequency of the decaying oscillations, as was done by Bracewell (1990). The flotation collars produced a significantly larger damping coefficient for the pillar than for the float, and the observed frequency of pillar vibration was 0.3 Hz.

**Power Take-Off Characterization**

Eq. 12 relates the generator damping, $c_{gen}^{\theta}$, to the damping of float travel along the pillar, $c_{gen}^{\xi}$. Regardless of the coefficient chosen, Graves (2000) showed that the generator damping coefficient for a simple DC generator has an inverse relationship with external load resistance, of the form,

$$c_{gen}^{\xi}(R_{ext}) = \frac{a_{gen}}{(R_{int} + R_{ext})} + b_{gen} \tag{29}$$

The constants, $a_{gen}$, and, $b_{gen}$, depend on the motion variable in terms of which the damping effect is defined. We choose to work with, $c_{gen}^{\xi}$, to be consistent with Eq. 1. Additional float decay tests were conducted in which the generator circuit was closed using various field resistances. However, the rheostat used as the field resistance was not well matched to the chosen DC generator: the full scale resistance was 5 kΩ and the useful range of resistance values was found to be $0\Omega \le R_{ext} \le 200\Omega$. Values above $R_{ext} = 200\Omega$ were found to produce overall damping behavior that matched the tests in which the generator was disconnected. This indicated that, $a_{gen}$, was small and that the DC generator was undersized.

A bench-top experiment, the setup of which is shown in Fig. 7, was built to more accurately quantify the generator damping as a function of external resistance. The experiment consisted of the Charlotte power take-off module with the input shaft coupled to a torsion spring, in place of the chain drive. A rotational encoder provided generator shaft rotation data during a series of transient response tests at various external resistances. The generator response traversed from under-damped to over-damped as external resistance decreased. Various methods of damping quantification including logarithmic decrement, settling time, and percent overshoot methods were applied.

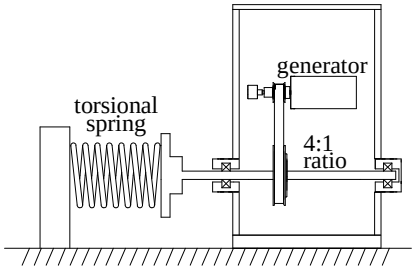


Fig. 7. Bench experiment to quantify generator damping. Shows the PTO input shaft coupled to a torsion spring.

The data from all methods are plotted and a least squares fit of the form of Eq. 29 is shown in Fig. 8. and the coefficient values are given in Table 3. During the bench-top tests, the power take-off inertia was found to be small, thus validating the removal of $I_{PTO}$ from Eq. 5. At low resistances, reasonable agreement with the hypothesis of Graves (2000) was achieved.

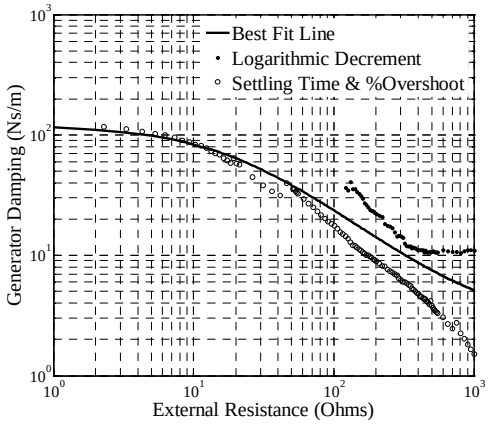


Fig. 8. Generator Damping vs. External Load Resistance.

From Fig. 8, it is apparent that the generator damping is extremely sensitive to small changes in external load resistance, especially at small resistance values. During the tank trials generator damping was set at its maximum value (i.e. smallest resistance – approximately 1Ω) in an attempt to maximize the power output. However, due to the lack of resolution of the 5 kΩ rheostat, the actual generator damping may have varied significantly.

Table 3. Generator Parameters from best fit of $c_{gen}^{\xi}$.

| Physical Parameter | Value |
|---|---|
| Generator Constant ($a_{gen}$) | 2556 NsΩ/m |
| Generator Offset ($b_{gen}$) | 3.658 Ns/m |
| External Resistance used for wave testing ($R_{ext}$) | 1 Ω |
| Armature Resistance ($R_{int}$) | 21.7 Ω |

## RESULTS

Mean wave-height and the wave frequency for each trial run were obtained using the Fourier transform of a wave probe signal. The wave amplitude used in the model based predictions, *A*, was the magnitude of the dominant peak. This technique was used to filter out high frequency components due to wave reflections. Wave reflections were

more pronounced at lower frequencies. In the Fourier transform plots, the second largest peak magnitudes were, at most, 25% of the dominant peak magnitudes.

Three dimensional motion capture data was converted, through inverse kinematics relationships, to time series plots of pitch, roll, and yaw motions. Statistics for these results are given in Table 4. The mean pitch and roll angles are very low with maximum values of 2.2 degrees and 0.38 degrees respectively, thereby validating the assumption of a pure heave response inherent to the dynamics modeling given by Eqs. 7-28. The yaw displacement was always less than 5 degrees.

Table 4. Test Statistics

| Physical Parameter | Max | Mean | Std. Deviation |
|---|---|---|---|
| Pitch | 2.183 $^o$ | 1.732 $^o$ | 0.280 $^o$ |
| Roll | 0.384 $^o$ | 0.223 $^o$ | 0.095$^o$ |
| Yaw | 4.416 $^o$ | 2.177 $^o$ | 1.347$^o$ |
| Wave Height (2*A*) | 0.243 m | 0.194 m | 0.032 m |

At first glance, the Charlotte prototype appears that it could be subject to significant excitation effects due to near trapping of waves. McIver and McIver (2006) discussed how freely floating structures experience "motion trapping" using a 1-DOF heaving dynamics model. The frequency domain analysis of that work suggested that for any value of $k$, there exists a structure capable of motion trapping. However, if a trapped or near–trapped mode existed during the tests, significant magnification of the free surface elevation between the float/pillar bodies would have occured. By contrast, observations of the free surface elevation between the cylinders during testing showed no significant magnifications. Actually, significant attenuations in the free surface displacements were observed due to a considerable amount of dissipative structural interference.

As suggested by McIver (2002) and Bracewell (1990), significant wave interactions with the tank walls are predicted to occur if,

$$kL = n\pi \,, \tag{30}$$

where $L$ is the distance between the sides of the float and the tank walls and $n$ is a positive integer. The free surface between the sides of the float and the tank walls is un-obstructed, and is the only location where standing waves due to tank reflections are feasible. For our testing: $kL \le 2.2 < \pi$. Therefore, throughout the entire test frequency range, standing wave interactions between the float and the tank walls should not occur.

Mechanical power delivered to the generator was measured using the onboard dynamometer. The onboard dynamometer was based on time varying measurement of the reaction torque developed on the base of the PTO generator multiplied by an encoder angular velocity signal at the generator shaft.

$$P(t) = \tau(t)\dot{\theta}_{gen}(t) \tag{31}$$

An average power output was calculated for each test by taking the mean of the mechanical power time series. This is equivalent and directly comparable to the predicted power value given by Eq. 27. The WEC was tested over the frequency range of (0.35-0.65Hz) at regular wave heights of 19 cm average. Time series plots of torque, generator shaft speed, and mechanical power are shown in Figs. 9~11. These correspond to a single data point in Fig. 11 ($ka$ = .39, P = 6.5W).

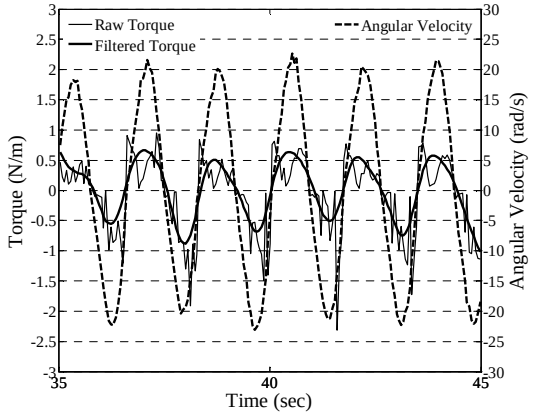


Fig. 9. Time-series plot of mechanical torque and generator shaft angular velocity corresponding to ($ka$ = .39, P = 6.5W) in Fig. 11.

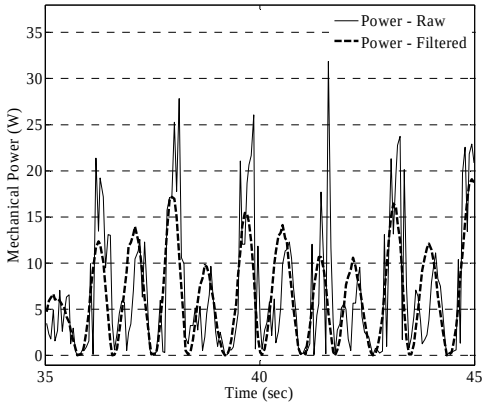


Fig. 10. Time-series plot of mechanical power corresponding to (ka = .39, P = 6.5W) in Fig. 11.

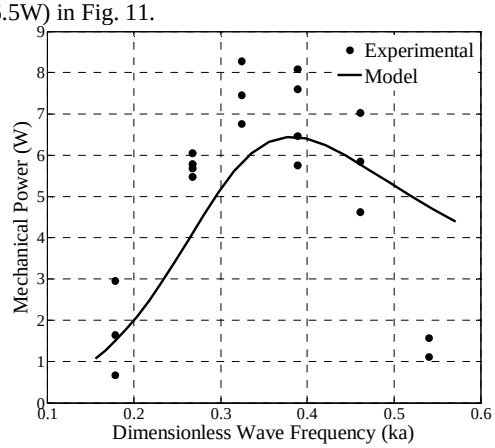


Fig. 11. Mechanical power vs. wave frequency.

The spikes in the raw torque and mechanical power signals can be associated with mechanical backlash observed in the PTO system. As the direction of shaft rotation changes, an impact due to the backlash is felt by the load cell. The generator shaft velocity signal, shown in Fig. 9, is a near steady sinusoidal oscillation with zero mean, indicating that our assumption of steady state oscillations is valid. A comparison of the experimental power to model power is shown in Fig. 11. From dimensionless frequency $ka$ of 0.15 to 0.45, the model (run at a mean wave-height of .194 m) line is very near a mean line of the

experimental data. At high frequencies the model diverges from the experimental data points. The divergence may be due to a breakdown of the small body approximation because *ka* is approaching unity.

The high variance in the experimental data can be attributed principally to three sources. First, the testing was performed using an un-calibrated wave tank; Hence, the mean wave heights of the time series at each frequency varied significantly from the desired nominal wave height as shown in the last row of Table 4.

Secondly, there was a large degradation of wave quality due to the superposition of reflected waves from the end of the tank, a notable limitation of the wave tank facility. Thirdly, the power take-off generator did not behave as a reliable damper. The coefficient $c_{gen}$ varied between 10 Ns/m to 100 Ns/m. This we can generally attribute to the nature of Eq. 29, because, at low resistances, the generator damping coefficient is extremely sensitive to small error in load resistance. Since the power absorbed is linearly dependent on $c_{gen}$, this error propagates into the power calculation.

The Charlotte model has been scaled up to approximate the power output of an ocean going system. The chosen scaling procedure is to bound the observed wave frequency range by the float and pillar natural frequencies on the high and low sides respectively. To date, wave data taken at Amphitrite Pt. near Ucluelet BC between 2002 and 2004 has been used to guide this scale up procedure. The wave periods generally fall between 6 and 10 s and, applying deepwater conditions, this translates to wavelengths between 56 m and 156m. As such the small body approximation is more applicable, and hence the accuracy of the dynamics model should improve. The predicted power absorbed by the ocean going unit was calculated by using the dynamics model of the scaled up geometry to calculate the hourly response subject to the hourly Amphitrite wave conditions. The scaled up device produces an annual average of 1.61 kW with float and pillar masses of 13,115 kg and 18,733kg, and effective float and pillar diameters of 1.54 m and 0.97 m respectively. In the winter months the device produces 16 kW when 6 m waves are experienced. The annual average is dropped because of extended periods of small waves (~1.0 m) in the summer months. The Amphitrite Pt. location is very near shore and is surrounded y shallows. Currently, a wave buoy is being redeployed by UVic researchers in a search for a more suitable location.

## CONCLUSIONS

The design methodology was presented for a small two-body heaving point absorber. A heave-constrained linear model was developed, utilizing the small body approximation in radius and depth. Depth reference points were chosen logically in order to calculate a single reference depth for both components of the WEC. This facilitated a lumped representation of the fluid-body interactions, and a constant parameter model of the body excitation forces. The use of a simple DC generator modeled as a linear dashpot controlled by an external load resistance is presented and shows reasonable agreement with theoretical behavior. However, the generator chosen for the tank tests was found to be undersized and hence the generator damping was very sensitive to the field resistance. The model is shown to provide a reasonable prediction of steady state power output given the assumption of linear heaving dynamics and the high variance in the experimental power data.

Further work on the device is planned. First, a time domain simulation of the device using the wave-probe signal as an input is to be completed to check the effects of the reflected waves on the body motions and serve as another indicator of average power. Second, the problem of high variance in the generator damping is to be mitigated in future wave tank testing by replacing the DC generator with a calibrated rotational viscous dashpot. In addition, the power benefits of the addition of an internal oscillating mass will be modeled and compared to data from future wave tank tests.

## ACKNOWLEDGEMENTS

This work was supported by SyncWave Energy Inc., Mathematics of Information Technology and Complex Systems (MITACS) Internship program and the Natural Sciences and Engineering Research Council (NSERC).

## REFERENCES

Bjarte-Larsson, T and Falnes, J (2006). "Laboratory experiment on heaving body with hydraulic power take-off and latching control," *Ocean Engineering*, Vol 33, pp847-77

Bracewell, RH (1990). "*Frog and PS Frog: A Study of Two Reactionless Ocean Wave Energy Converters*," Lancaster University, http://www-edc.eng.cam.ac.uk/~rhb24/rhbthes.pdf

Budal, K and Falnes, J (1975). " A resonant point absorber of ocean-wave power," *Nature*, Vol 256, pp 478-9

Eidsmoen, H (1995). "Simulation of a slack-moored heaving-buoy wave energy converter with phase control," *2nd European Wave Power Conference*, Lisbon

Falnes, J (1999). "Wave-energy conversion through relative motion between two single-mode oscillating bodies," *Journal of Offshore Mechanics and Arctic Engineering*, Vol 121, pp32-8

Falnes, Johannes. Ocean waves and Oscillating Systems. Cambridge University Press; 2002.

Graves, EK (2000). "*Electromagnetic Energy Regenerative Vibration Damping*," Swinburne University of Technology, http://adt.lib.swin.edu.au/public/adt-VSWT20060307.120939/index.html

McIver, P (2002). "Wave interaction with arrays of structures," *Applied Ocean Research*, Vol 24, pp121-6

McIver, P and McIver, M (2006). "Trapped modes in the water-wave problem for a freely floating structure," *Journal of Fluid Mechanics*, Vol 558, pp53-67

Srokosz, MA and Evans, DV (1979). "A theory for wave-power absorption by two independently oscillating bodies," *Journal of Fluid Mechanics*, Vol 90, pp337-62

Weinstein, A, Fredrikson, G, Parks, MJ, and Nielsen, K (2004). "AquaBuOY - the offshore wave energy converter numerical modeling and optimization," *MTS/IEEE TECHNO-OCEAN '04*

# Appendix B

# Frequency Response Tuning for a Two-Body Heaving Wave Energy Converter

# Frequency Response Tuning for a Two-Body Heaving Wave Energy Converter

*Scott J. Beatty, Bradley J. Buckham, Peter Wild*
Department of Mechanical Engineering
University of Victoria, BC, Canada

## ABSTRACT

**This study investigates frequency response tuning for a two-body heaving wave energy converter. The device presented is a 'spar-float' configuration scale model for wave-tank testing to validate a tuning mechanism which enables spar natural frequency adjustment. Numerical optimization is used to demonstrate the utility of this tuning mechanism. Analytical solutions to a frequency domain dynamics model are used to establish objective functions. For a range of wave frequencies, optimal spar natural frequencies are computed. The results show that significant power absorption benefits are possible using spar frequency response tuning.**

KEY WORDS: Wave energy conversion; point absorber; heaving buoy; parametric design; optimization; control system

## INTRODUCTION

The concept of an internally housed, oscillating reaction mass for the purpose of frequency response tuning is not new. However, the suggested implementations to date require complex control schemes and/or energy intensive actuators. French and Bracewell developed a heaving point absorber with latching control of an internal reaction mass (Bracewell (1990)). Called "Frog," the device absorbs energy from the relative motion between the reaction mass and the hull, but latching control requires excellent knowledge of the wave regime on a prohibitively short time scale. Korde presents a tuning system that utilizes a ship heave compensator (Korde (1999)), similar to those typically used to minimize TLP motions (Alves and Batista (1999)), as a vibration absorber to maintain a fixed reference against which a heaving body can react. These systems require continuous operation of an actuator to provide frequency response adjustments. Avoiding such energy intensive control adjustments saves valuable converted electrical energy. A two-body heaving WEC that utilizes a novel frequency response tuning system is under development at the University of Victoria. The tuning system uses an internal reaction mass to generate the frequency response adjustments. Gerber (2007) describes a theoretical variable spring stiffness control over a fixed reaction mass. In contrast to that concept, the current work complements variable spring stiffness with inertial adjustments to affect changes in the frequency response of the spar. The adjustments are completed in a short time to capitalize on the predominant wave components and no energy is consumed between adjustments. In contrast to the methods of Bracewell (1990) and Korde (1999), the tuning system proposed in this work requires neither large control forces nor latching control to operate. In this work, the need for frequency response tuning is established using optimization methods to quantify ideal variations in the two-body WEC's spar frequency response. These variations are compared to those achievable using a novel electro-mechanical tuning mechanism.

This work follows the philosophy of Bjarte-Larsson and Falnes (2001): a simplified wave-body dynamics model is used to explore the potential benefits from, and justification of, this type of tuning system in a wave-tank specific design scenario. In addition, a methodology is developed for the synthesis of relative motion based heaving WEC designs. The first section establishes parametric design laws for the structure of the two-body WEC prototype. The second section describes the simplified wave-body dynamics model. In the third section, the model is then applied to investigate the frequency response behavior of the WEC with no generator. The fourth section builds on the previous section by applying a generator of optimal intensity. In the fifth section, a fixed spar shape is maintained while the frequency response is explored. Finally, in the last section, the novel frequency response tuning concept is introduced.

## WEC STRUCTURE

### Design Constraints

The most important parameter that drives the design of a heaving body is the natural frequency of the body $\omega_j = \sqrt{k_j/m_j}$. The hydrostatic stiffness of the body is proportional to the water plane area i.e. $k_j = \rho g \pi r_j^2$ and the mass of the body, by static force balance and Archimedes law, is proportional to the submerged volume i.e. $m_j = \rho V_j$. If the body is cylindrical, $m_j = \rho \pi r_j^2 T$, where $T$ is the draft of the cylinder, then:

$$\omega_j = \sqrt{\frac{\rho g \pi r_j^2}{\rho \pi r_j^2 T}} = \sqrt{\frac{g}{T}} \tag{1}$$

Eq. (1) is a strict design constraint for heaving cylinders. Notice that if $\omega_j$ is chosen, the draft of the cylinder has been implicitly chosen. As a

result, a low frequency heaving cylinder must have a very deep draft. For example, a cylinder designed to resonate to waves of 14 second period (0.45 rad/s) will have a draft of 49 m. An obvious way to avoid the deep draft problem is to deviate from a cylindrical geometry. To set the device size, the radius at the water-plane, $r_j$, can be chosen, hence $k_j$ is fixed. Below the water surface, the diameter can vary as required so that the submerged volume (displacement) satisfies the static vertical force balance. For realistically shaped WEC components, it is expected that a deviation from the cylindrical shape will be required achieve the low natural frequencies to required to approach a resonant response in the more energetic ocean waves.

## Parametric Design

For this study, the design wave height, $H$, is chosen to be 0.5m to best utilize the wave tank capabilities. The float geometry is fixed as a cylindrical body with natural frequency $\omega_1$ set to 3.13 rad/s for a draft of $T_1 = 2H = 1$ m. The spar has a parameterized, non-cylindrical geometry as shown in Fig. 1. The spar bulb radius is free to vary as necessary with the spar natural frequency within the range $1.0 \leq \omega_2 \leq 2.0$ rad/s. A semi-spherical bottom and conical section were chosen for simplicity as well as to minimize viscous damping effects due to vortex formation. The water plane cylindrical section of radius $r_2$, the tapered section, and the clearance between the WEC and tank bottom all have been parameterized with respect to $H$. Notice that the spar (body 2 in Fig. 1) contains a sub-system of mass $m_3$ which is the tuning module to be discussed later. The spar bulb shape is parameterized in

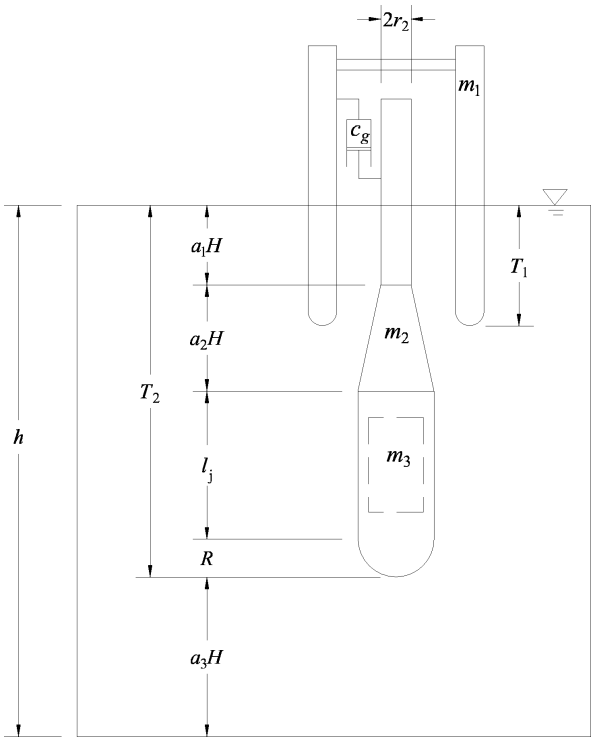


Fig. 1. Parameterized Spar and Tank Geometry

terms of $H$ and arbitrary geometric constants $a_1$, $a_2$, $a_3$, and $a_4$. To maintain a linear hydrostatic stiffness throughout the spar motion, the total length of the constant cross section of radius $r_2$ ($a_1 H$) is chosen. $a_2$ is chosen to define a gradually tapered section so that a low heave damping can be maintained. $a_3$ specifies the clearance between the tank bottom and the spar bottom to prevent impact with the floor. The ratio

Table 1. Wave Tank and design constraint parameters

| Parameter | Symbol | Value |
|---|---|---|
| Tank depth | $h$ | 7.0 m |
| Design wave height | $H$ | 0.5 m |
| Wave frequency range | $\omega$ | $1 \rightarrow 4$ rad/s |
| Bottle neck constraint | $a_1$ | 1.5 |
| Taper portions constraint | $a_2$ | 2.0 |
| Draft constraint | $a_3$ | 3.0 |
| Spar to reaction mass ratio | $a_4$ | 1.8 |
| Body 1 natural frequency | $\omega_1$ | 3.13 rad/s |
| Body 1 hydrost. stiffness | $k_1$ | 1491 N/m |
| Body 2 natural frequency | $\omega_2$ | $1.0 \rightarrow 2.0$ rad/s |
| Body 2 hydrost. stiffness | $k_2$ | 613 N/m |
| Float damping ratio | $\zeta_1$ | 0.2 |
| Spar damping ratio | $\zeta_2$ | 0.3 |
| Reaction mass damping ratio | $\zeta_3$ | 0.3 |

of the reaction mass to the spar mass, represented by $a_4$, relates to the effectiveness of the tuning module. As $a_4$ increases, the effectiveness of the tuning module improves, however the practical feasibility of the system decreases. For this study, we have approached the limit of practicality by setting $a_4 = 1.8$. Using this geometrical formulation, a desired spar draft $(h - a_3 H)$, stiffness $k_2$, and natural frequency $\omega_2$ can be defined. Table 1 shows the Institute for Ocean Technology wave tank parameters and the chosen parametric spar design parameters. Since this work is focused on design synthesis using a simplified model, tank width effects and detailed hydrodynamics have been neglected. The submerged volume of the parameterized spar can be expressed as:

$$V_2 = \pi(a_1 H r_2^2 + \frac{1}{3} a_2 H (R^2 + R r_2 + r_2^2) + l_j R^2 + \frac{2}{3} R^3) \tag{2}$$

where $l_j$ is,

$$l_j = h - (a_1 + a_2 + a_3)H - R \tag{3}$$

To account for the tuning module of mass $m_3$ to be housed inside the spar (body 2), the total mass of the system comprising the both the spar and tuning module is as follows,

$$m_{23} = m_2 + m_3 = (1 + a_4) m_2 \tag{4}$$

where $a_4 = \frac{m_3}{m_2}$. We define the natural frequency of the system comprising the both the spar and tuning module as,

$$\omega_{23} \equiv \sqrt{\frac{k_2}{m_2 + m_3}} = \frac{\omega_2}{\sqrt{1 + a_4}} \tag{5}$$

Using the Archimedes principle:

$$m_{23} = (1 + a_4) m_2 = \rho V_2 \tag{6}$$

and substituting in the hydrostatic stiffness, $k_2 = \rho g \pi r_2^2$, and mass $m_{23} = \frac{k_2}{\omega_{23}^2}$ of body 2 into Eq. (2), the result is a cubic equation in $R$:

$$R^3 + A_1 R^2 + A_2 R^3 + A_3 = 0 \tag{7}$$

where,

$$A_1 = -3a_1 H - 2a_2 H - 3a_3 H + 3h \tag{8a}$$

$$A_2 = a_2 H r \tag{8b}$$

$$A_3 = 3a_1 H r^2 + a_2 H r^2 - 3\frac{g r^2}{\omega_{23}^2} \tag{8c}$$

Solutions of Eq. 7 give $R$ as a function of $\omega_{23}$ (which can easily be expressed in terms of $\omega_2$ using Eq. 5) and so the spar geometry is successfully parameterized in terms of desired size and natural frequency. The resulting relationship between spar natural frequency and spar geometry has been obtained and plotted for a relevant range of $\omega_2$ given by Fig. 2. Notice the transition point at $\omega_2 = 2.2$ rad/s. This represents the transition to a cylindrical geometry from a non-cylindrical (bulbous) geometry. This arises because, as the spar natural frequency $\omega_2$ increases, the bulbous hull shape is no longer required to supply added submerged volume to maintain a vertical force balance and adhere to the maximum draft constraint. From $\omega_2 = 2.2$ rad/s on, the spar geometry is cylindrical with decreasing draft, as governed by Eq. 1. At the low end of the

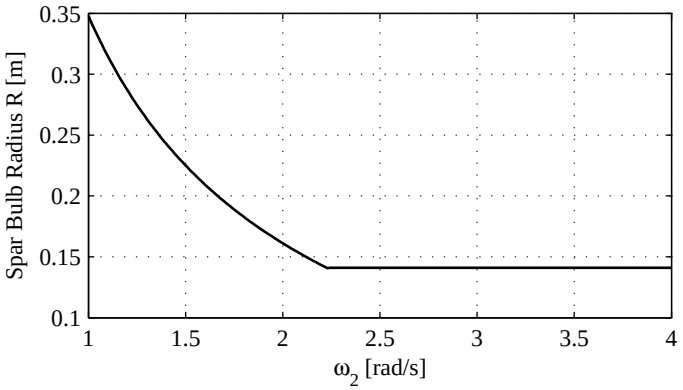


Fig. 2. Variation of $R$ with body 2 natural frequency $\omega_2$

frequency range, Fig. 2 shows that extremely large $R$ is required for $\omega_2 < 1.0$ rad/s. For large values of R, the spar would most likely violate the assumption of a low heave damping coefficient. Hence the lower spar frequency limit was arbitrarily chosen as $\omega_2 = 1.0$ rad/s to maintain a reasonable hull aspect ratio. The upper limit was chosen to be consistent with the expected capability of the tuning system to be presented later. As a result, the chosen range of the spar natural frequency is $1.0 \leq \omega_2 \leq 2.0$ rad/s. Through Eq. 5, this range can be converted to the range $0.6 \leq \omega_{23} \leq 1.2$ rad/s given the chosen spar to reaction mass ratio $a_4$ given in Table 1.

## SMALL BODY DYNAMICS MODELING

In the preceding section, we arbitrarily set the float natural frequency to a relatively high value $\omega_1 = 3.13$ rad/s and parameterized the spar so that $\omega_2$ completely specifies its geometry. In this section, the dynamics model is used to predict the performance given an arbitrary choice of $\omega_1$ and $\omega_2$. The model is a 2 degree-of-freedom system of linear ODE's with constant coefficients, as described in Beatty et al. (2007). This model can be used to approximate the steady state response of the WEC to regular waves. The model employs the "long wavelength approximation" to the wave excitation forces, under the assumption that $\max(ka) \ll 1$, where the water surface amplitude is evaluated at the vertical axis of symmetry of the WEC. Since the waves are assumed regular, the complex amplitudes of the body displacements, $\hat{\xi}_j$, can be found in the frequency domain.

### Excitation Force

For a given wave amplitude, $A = \frac{H}{2}$, the wave excitation force on each body is modeled by Eq. 9.

$$\boldsymbol{f}_{e12} = \left[ \begin{pmatrix} m_1 \hat{a}_{01} \\ m_2 \hat{a}_{02} \end{pmatrix} \frac{1}{A} + \begin{pmatrix} c_1 \hat{v}_{01} \\ c_2 \hat{v}_{02} \end{pmatrix} \frac{1}{A} + \begin{pmatrix} k_1 \\ k_2 \end{pmatrix} \right] A \tag{9}$$

The fluid velocity and accelerations, $\hat{v}_{0j}$ in Eq. 11 and $\hat{a}_{0j}$ in Eq. 10 respectively, are evaluated at a "reference depth" $z_{Pj}$ as described by Falnes (2002) and Clauss et al. (1992) for application to the design of offshore structures. The wavenumber, $k$, is obtained from an iterative solution to the dispersion relation.

$$\hat{a}_{0j} = -\omega^2 \frac{\sinh(kz_{Pj} + kh)}{\sinh(kh)} A \tag{10}$$

$$\hat{v}_{0j} = i\omega \frac{\sinh(kz_{Pj} + kh)}{\sinh(kh)} A \tag{11}$$

The reference depth for any cylindrical body is assumed to be equal to its draft; However, the reference depth for a composite shape, such as the spar design given by Fig. 1, is approximated by a weighted average depth where the weighting is based on the protruding areas normal to the heave direction as outlined by Beatty et al. (2007). The reference depths used for the float and spar, are given by Eq. 12 and Eq. 13 respectively, where $T_{max}$ is the draft constraint defined by $T_{max} = h - a_3 H$.

$$z_{P1} = \frac{g}{\omega_1^2} \tag{12}$$

$$z_{P2} = \begin{cases} \frac{\left((a_1+a_2)H(R^2-r^2)+((a_1+a_2)H+l_j)R^2\right)}{(2R^2-r^2)} & \text{if } T_2 \geq T_{max}, \\ \frac{(1+a_4)g}{\omega_2^2} & \text{if } T_2 < T_{max} \end{cases} \tag{13}$$

### Governing Dynamics Equations

The vector of displacements for this "spar-float" two-body system is defined by Eq. 14, and the governing differential equation can be arranged in matrix form (Eq. 15).

$$\boldsymbol{x} = \Re \left\{ \begin{bmatrix} \hat{\xi}_1 \\ \hat{\xi}_2 \end{bmatrix} e^{i\omega t} \right\} \tag{14}$$

$$\underline{M}\ddot{\boldsymbol{x}} + \underline{C}\dot{\boldsymbol{x}} + \underline{K}\boldsymbol{x} = \boldsymbol{f}_e \tag{15}$$

For the two body system comprising body 1 and body 2, the mass, stiffness, and damping matrices are given by Eq. 16, Eq. 17, and Eq. 18 respectively. The model employs a linear viscous dashpot with coefficient $c_g$ to represent the power take off generator. The damping matrix includes the coupling effect of the generator damping, but for simplicity, no hydrodynamic cross-coupling terms are included.

$$\underline{M}_{12} = \begin{bmatrix} m_1 & 0 \\ 0 & m_2 + m_3 \end{bmatrix} = \begin{bmatrix} \frac{k_1}{\omega_1^2} & 0 \\ 0 & (1+a_4)\frac{k_2}{\omega_2^2} \end{bmatrix} \tag{16}$$

$$\underline{K}_{12} = \begin{bmatrix} k_1 & 0 \\ 0 & \rho g \pi r_2^2 \end{bmatrix} \tag{17}$$

$$\underline{C}_{12} = \begin{bmatrix} c_1 + c_g & -c_g \\ -c_g & c_2 + c_g \end{bmatrix} \tag{18}$$

$$\begin{aligned} &[-\omega^2 \underline{M}_{12} + i\omega \underline{C}_{12} + \underline{K}_{12}] \begin{bmatrix} \hat{\xi}_1 \\ \hat{\xi}_2 \end{bmatrix} = \\ &\left[ \begin{pmatrix} m_1 \hat{a}_{01} \\ m_2 \hat{a}_{02} \end{pmatrix} \frac{1}{A} + \begin{pmatrix} c_1 \hat{v}_{01} \\ c_2 \hat{v}_{02} \end{pmatrix} \frac{1}{A} + \begin{pmatrix} k_1 \\ k_2 \end{pmatrix} \right] A \end{aligned} \tag{19}$$

The solution, in terms of the complex amplitudes of the heaving displacements is found by matrix inversion of the combined dynamic matrix on the LHS of Eq. 19 multiplied by the RHS. This operation is done analytically to obtain closed form expressions for $\hat{\xi}_1(\omega)$, $\hat{\xi}_2(\omega)$, and $\hat{\xi}_{1/2}(\omega)$, where $\hat{\xi}_{1/2}(\omega) = \hat{\xi}_1(\omega) - \hat{\xi}_2(\omega)$. The power absorbed by the power take off damper is given by Eq. 20.

$$P(\omega) = \frac{1}{2}\omega^2 c_g |\hat{\xi}_{1/2}(\omega)|^2 \tag{20}$$

## RELATIVE MOTION ANALYSIS

In this section, the intent is to find the spar hull geometry that maximizes relative motion between the spar and the float at each wave frequency. This optimization has been done for $c_g = 0$ in Eq. 18. The design variable is the natural frequency of the spar ($1.0 \leq \omega_2 \leq 2.0$ rad/s). Since this is a 1D optimization, the objective function can be viewed and the maximum found by inspection. Convergence to any accuracy is quickly achieved using a Sequential Quadratic Programming algorithm. Observing Fig. 3, it is notable that the optimal body 2 natural frequency,

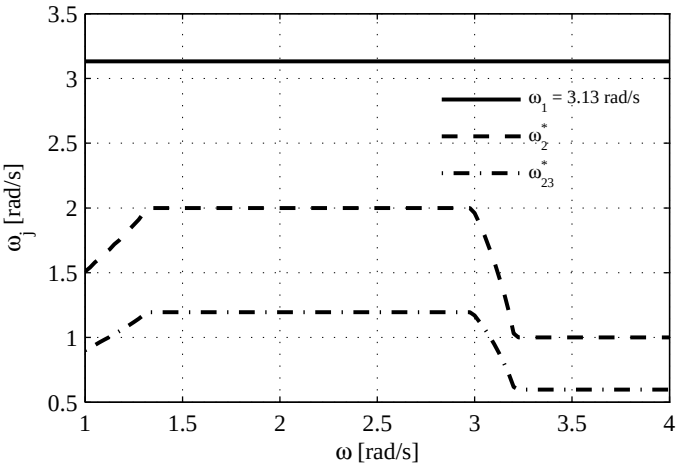


Fig. 3. Constrained optimal $\omega_2^*$ and $\omega_{23}^*$ with $c_g = 0$.

$\omega_2^*$, increases nearly one-to-one with wave frequency and then quickly reaches the upper allowable limit of $\omega_2$. Because $\omega_2^*$ is at the upper limit from $\omega$ =1.3-3.0 rad/s, the corresponding optimal relative motion curve in Fig. 4 only provides an envelope to the relative motion curves computed using fixed $\omega_2$ values at extreme low and high frequencies. For the maximization of relative motion on this system, the chosen range spar natural frequency range ($1.0 \leq \omega_2 \leq 2.0$ rad/s) is not well suited. It is expected that, if the range could be relaxed, more significant improvements in terms of relative motion could be gained. While relative motion is used as an objective here as a guide in the selection of the spar frequency, the final task is to optimize the power production which also depends on the generator damping level. In the next section, we will examine the potential benefits of frequency response tuning within the chosen range for a more realistic 2-body system coupled by a generator when $c_g \neq 0$.

## MAXIMUM POWER WITH SPAR SHAPE VARIATION

To convert relative motion to useful energy, we must couple the float (body 1) and the spar (body 2) with a generator. Specifically, a non-zero value of $c_g$ is substituted into the damping matrix of Eq. 18. An optimization is employed to choose the generator damping as a function of wave frequency $c_g^*(\omega)$. The optimization is set up to maximize power extraction $P(\omega)$ with the design variables being $c_g(\omega)$ and $\omega_2(\omega)$. Optimal and non-optimal(for fixed $\omega_2$) power absorption are shown as a function of wave frequency in Fig. 5. The results show that the allowable range of $\omega_2$ is more suited to a generator coupled system. The optimal design variables, $c_g^*$ and $\omega_2^*$, are plotted in Fig. 6 and Fig. 7 respectively. It appears that significant benefits at the low wave frequencies could be obtained from this prototype WEC design where the spar hull shape varies optimally with wave frequency.

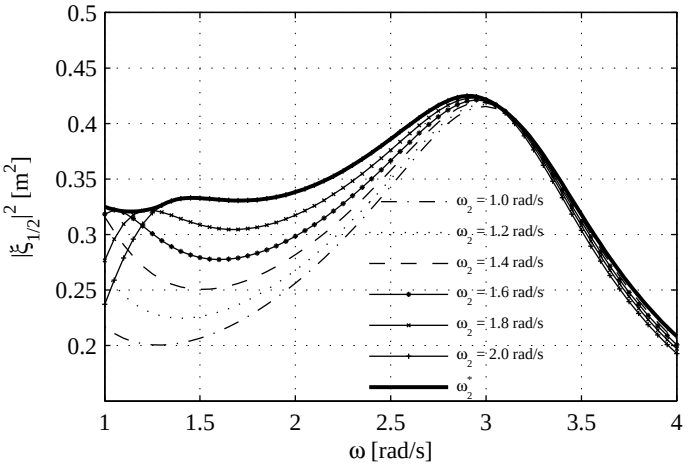


Fig. 4. Relative motion for optimal, $\omega_2^*$, and non-optimal $\omega_2$ with $c_g = 0$.

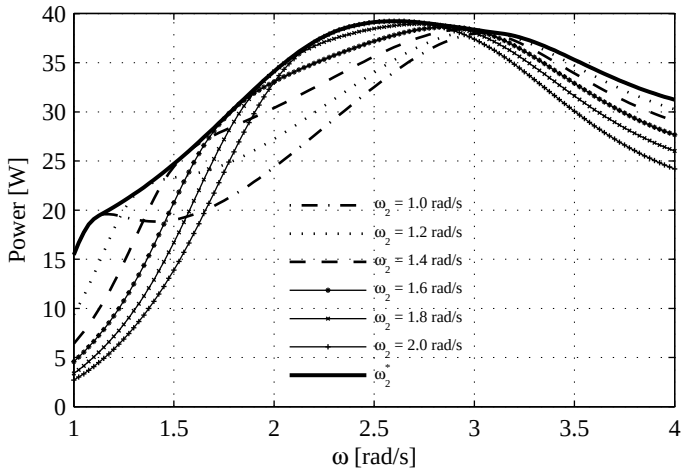


Fig. 5. Power capture for optimal, $\omega_2^*$, and non-optimal cases for the variable spar shape, $c_g \neq 0$ system.

## MAXIMUM POWER WITH FIXED SPAR SHAPE

In this section, we fix the geometry of the spar to its lowest frequency limit (i.e. $\omega_2 = 1.00$ rad/s). Hence $R = 0.35$m (from Fig. 2) and $z_{P2} \simeq 3.5$m from Eq. 13. We assume that it is possible to adjust the spar natural frequency in the range $1.0 \leq \omega_2 \leq 2.0$ rad/s without affecting the external geometry. Observing Fig. 8, the power results are extremely similar to the results of Fig. 5. Fig. 8 shows that, for a fixed spar geometry, significant benefits in power absorption (up to 25%) could be attained in the lower part of the frequency range, if frequency reponse adjustments in the range $1.0 \leq \omega_2 \leq 2.0$ rad/s could be made. The optimal control parameters are near identical to the results of the previous section and are plotted along with those results in Fig. 6 and Fig. 7. This analysis shows that the power benefits produced by changes in the spar frequency are not due to the changing wave excitation force caused by a changing spar geometry. Rather, the power output increases are due to changes in the dynamic response to a consistent wave excitation.

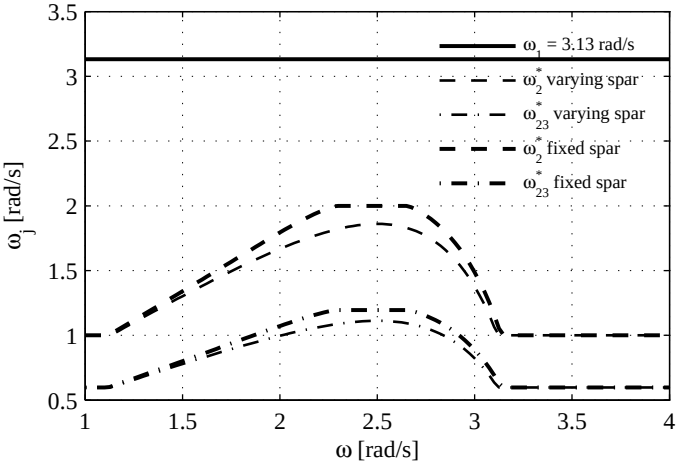


Fig. 6. Constrained optimal $\omega_2^*$, for the variable spar shape, $c_g \neq 0$ system.

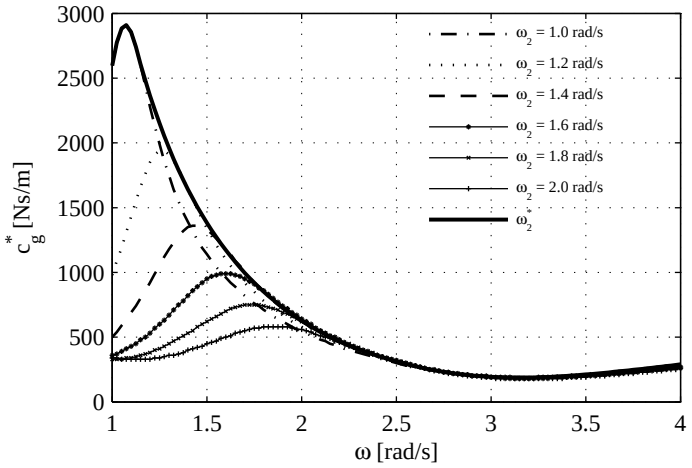


Fig. 7. Constrained optimal $c_g^*$ for the variable spar shape, $c_g \neq 0$ system.

## FREQUENCY RESPONSE TUNING

In the preceding sections, it was shown that the $\omega_2^*$ variations have a positive influence on the prototype two-body WEC energy conversion. In addition, significant energy improvements are still available while maintaining a fixed spar hull shape. In this section, a novel way of maintaining a fixed spar hull shape while still providing frequency response tuning to the optimal spar natural frequency, $\omega_2^*$, is presented.

### A Novel Tuning Mechanism

The mechanical implementation of the tuning mechanism housed within the spar, as described in Protter et al. (2007) and shown in Fig. 9, utilizes a spring mounted reaction mass. Through the use of a ballscrew assembly, the reaction mass is kinematically coupled to a rotational system. Mounted to the ballscrew shaft is a rotating assembly that can be varied geometrically so as to provide a variable moment of inertia ($J$). The operation of this device is essentially a "fly-ball governor" driven in reverse.

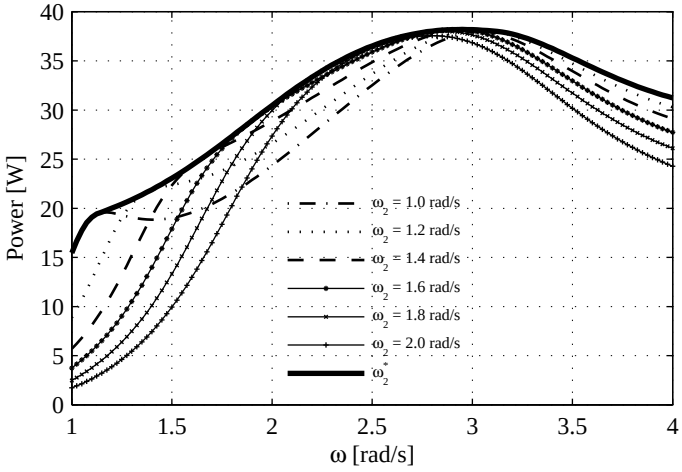


Fig. 8. Power capture for optimal, $\omega_2^*$, and non-optimal cases for the fixed spar shape, $c_g \neq 0$ system.

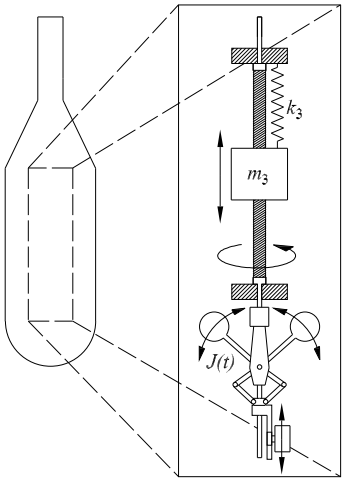


Fig. 9. Conceptual schematic of the frequency response tuning system

### Dynamics Model

In order to investigate the capability of the proposed tuning system, a dynamics model of the two-body system consisting of the spar (body 2), reaction mass (body 3), and the rotational system with moment of inertia, $J$, will now be adapted from the previous two-body model. For the spar, the same excitation force model of Eq. 9 is used, however the reaction mass has no excitation due to waves. Forces are induced on the reaction mass only by relative motion between it and the spar. For any heave translation of the reaction mass, the rotational system must rotate according to the ballscrew lead $l$ (units are m/rad). Specifically, the angular displacement of the rotational system, $\theta$, is related to the relative motion between the spar and reaction mass by:

$$\theta = \frac{\xi_3 - \xi_2}{l}, \dot{\theta} = \frac{\dot{\xi}_3 - \dot{\xi}_2}{l}, \ddot{\theta} = \frac{\ddot{\xi}_3 - \ddot{\xi}_2}{l} \tag{21}$$

For now, we assume a ballscrew of perfect efficiency so that torque, $\tau$, can completely be converted to thrust force, $F_t$, related by the ballscrew lead. By applying Newton's 2nd Law to the rotational system we have,

$$\tau = F_t l = J\ddot{\theta} \tag{22}$$

Therefore,

$$F_t = \frac{J\ddot{\theta}}{l} \tag{23}$$

By substituting the kinematic coupling relationship of Eq. 21 into Eq. 23, a final expression for the thrust force on the reaction mass due to the rotational inertia is obtained.

$$F_t = \frac{J}{l^2}(\ddot{\xi}_3 - \ddot{\xi}_2) \tag{24}$$

By applying Newton's law (observing the free body diagrams given by

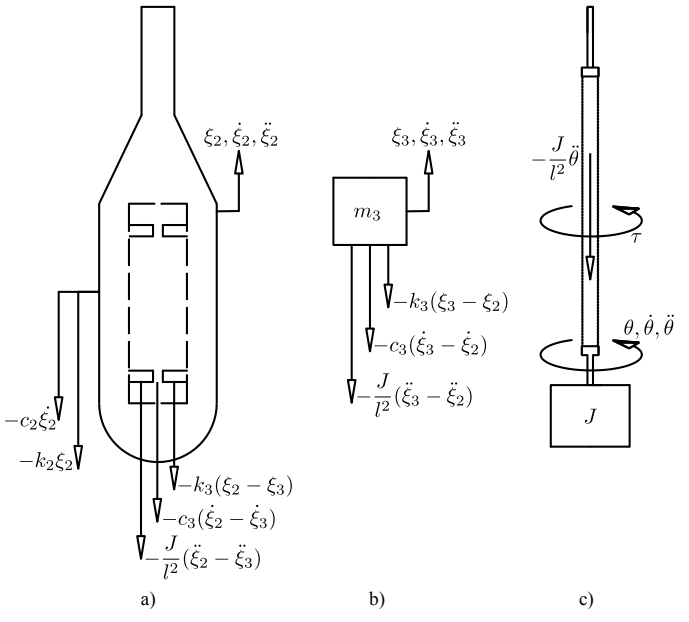


Fig. 10. (a) Free body diagram of the spar (body 2). (b) Free body diagram of the reaction mass (body 3). (c) Free body diagram of the rotational system.

Fig. 10) in the vertical direction, the governing differential equations for the spar and reaction mass are derived in Eq. 25 and Eq. 26 respectively.

$$\left(m_2 + \frac{J}{l^2}\right)\ddot{\xi}_2 - \left(\frac{J}{l^2}\right)\ddot{\xi}_3 + (c_2 + c_3)(\dot{\xi}_2 - \dot{\xi}_3) - c_3\dot{\xi}_3 + (k_2 + k_3)\xi_2 - k_3\xi_3 = f_{e2} \tag{25}$$

$$\left(m_3 + \frac{J}{l^2}\right)\ddot{\xi}_3 - \left(\frac{J}{l^2}\right)\ddot{\xi}_2 + c_3(\dot{\xi}_3 - \dot{\xi}_2) + k_3(\xi_3 - \xi_2) = 0 \tag{26}$$

Next, we choose to represent the terms proportional to the reaction mass acceleration as a function of the ratio of effective mass due to rotation, $\frac{J}{l^2}$, to the total mass defined as:

$$\eta \equiv \frac{\frac{J}{l^2}}{\frac{J}{l^2} + m_3} \tag{27}$$

The mass, stiffness, and damping and matrices are formed in Eq. 28, Eq. 29 and Eq. 30. By manipulating Eq. 27 and substituting in to the mass matrix, a conversion can be made to express the entries in the mass matrix as a function of the inertial control parameter, $\eta$, and the reaction mass, $m_3$.

$$\begin{aligned}\underline{M}_{23} &= \begin{bmatrix} \frac{J}{l^2} + m_2 & -\frac{J}{l^2} \\ -\frac{J}{l^2} & \frac{J}{l^2} + m_3 \end{bmatrix} \\ &= \begin{bmatrix} \frac{\eta}{1-\eta}m_3 + m_2 & -\frac{\eta}{1-\eta}m_3 \\ -\frac{\eta}{1-\eta}m_3 & \frac{1}{1-\eta}m_3 \end{bmatrix}\end{aligned} \tag{28}$$

$$\underline{K}_{23} = \begin{bmatrix} k_2 + k_3 & -k_3 \\ -k_3 & k_3 \end{bmatrix} \tag{29}$$

$$\underline{C}_{23} = \begin{bmatrix} c_2 + c_3 & -c_3 \\ -c_3 & c_3 \end{bmatrix} \tag{30}$$

The excitation force vector for the system comprising the spar and the reaction-mass, given by Eq. 31 is similar to Eq. 9, but the entries related to the reaction mass are zero because it has no external forcing.

$$\boldsymbol{f}_{e23} = \left[\begin{pmatrix} m_2\hat{a}_{01} \\ 0 \end{pmatrix}\frac{1}{A} + \begin{pmatrix} c_2\hat{v}_{01} \\ 0 \end{pmatrix}\frac{1}{A} + \begin{pmatrix} k_2 \\ 0 \end{pmatrix}\right] A \tag{31}$$

## Un-Damped Natural Frequencies

Introducing the reaction mass (body 3) to the spar (body 2) causes the system to have two natural frequencies; one above and one below the original natural frequency of the spar-reaction mass system ($\omega_{23}$ given by Eq. 5). These two natural frequencies can be found as the square roots of the eigenvalues $\lambda_i$ associated with mode shape vectors $X_i$ of the dynamic matrix, $\underline{D}$, formed using Eq. 28 and Eq. 29.

$$\underline{D} = \underline{M}_{23}^{-1}\underline{K}_{23} \tag{32}$$

We assemble a modal matrix from each mode shape vector as follows,

$$\underline{X} = \begin{bmatrix} X_1 & X_2 \end{bmatrix} \tag{33}$$

However, for this 2-body (spar-reaction mass) system, the distribution of damping, due to hydrodynamics and the viscous effects within the reaction mass assembly, is not proportional. For a non-proportionally damped system, the total response of the system may not be a linear combination of each mode. Hence, further analysis must be done to approximate the contributions of each natural mode to the steady state solution. As a result, Fig. 11 can only be used as a rough guide to the understanding of the 3-body steady state dynamics. Observing Fig. 12,

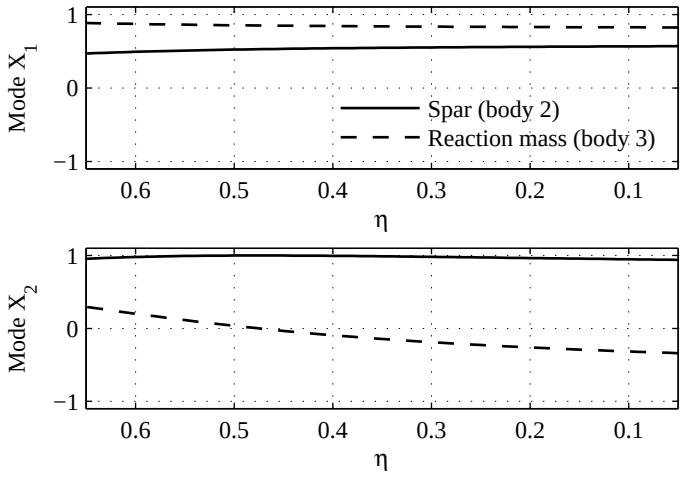


Fig. 11. Normalized natural mode shapes $X_1$ and $X_2$ as a function of control parameter $\eta$

the wave frequency range is always above $\sqrt{\lambda_1}$, but it is possible that mode $X_1$ could provide some contribution to the spar motion and thus to the power generation. The natural frequencies ($\sqrt{\lambda_i}$) are plotted as a surface against $\eta$ and $k_3$ in Fig. 13. We observe in Fig. 13 that variations of both $\eta$ and $k_3$ can be used to affect changes in the natural frequencies $\sqrt{\lambda_i}$, and therefore must provide some changes to the steady state solution. The operating point of the control system would be such

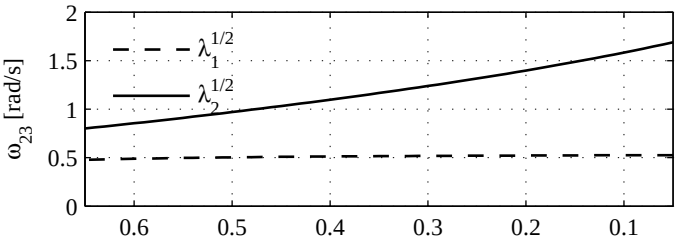


Fig. 12. A slice of the $\sqrt{\lambda_i}$ natural frequency surface for $k_3 = 1000$ N/m

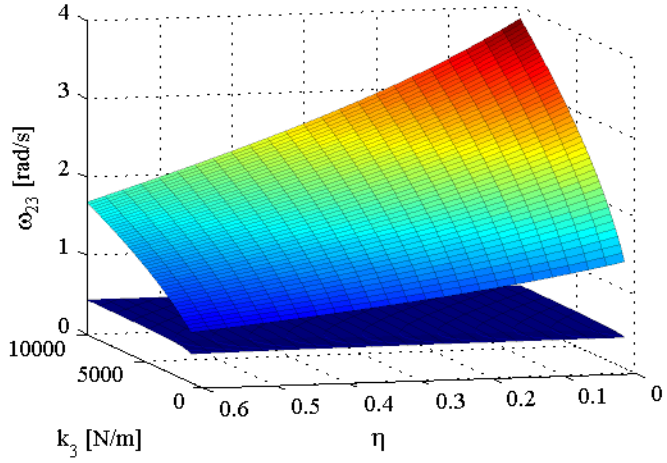


Fig. 13. The $\sqrt{\lambda_i}$ natural frequency surface

that, by making adjustments in $\eta$ (using a servo-motor to adjust the inertia $J(t)$ of Fig. 9), the adjustments would be made to the natural frequencies of the spar-reaction mass system, $\omega_{23}$. In turn this would allow a limited, medium-time scale optimization of power absorption to the predominant swell period as it changes with time.

## COMPLETE THREE-BODY SYSTEM

The previous section provides an un-damped vibration analysis of the spar, and shows that $\omega_{23}$ variations might be obtained with adjustments to the inertial control parameter $\eta$. In this section, we assemble and analyze the complete 3 body system composed of the float, spar, and the novel tuning system housed withing the spar. The mass, stiffness, and damping matrices are given by:

$$\underline{M}_{3body} = \begin{bmatrix} m_1 & 0 & 0 \\ 0 & \frac{J}{l^2} + m_2 & -\frac{J}{l^2} \\ 0 & -\frac{J}{l^2} & \frac{J}{l^2} + m_3 \end{bmatrix} = \begin{bmatrix} m_1 & 0 & 0 \\ 0 & \frac{\eta}{1-\eta} m_3 + m_2 & -\frac{\eta}{1-\eta} m_3 \\ 0 & -\frac{\eta}{1-\eta} m_3 & \frac{1}{1-\eta} m_3 \end{bmatrix} \quad (34)$$

$$\underline{K}_{3body} = \begin{bmatrix} k1 & 0 & 0 \\ 0 & k_2 + k_3 & -k_3 \\ 0 & -k_3 & k_3 \end{bmatrix} \quad (35)$$

$$\underline{C}_{3body} = \begin{bmatrix} c_1 + c_g & -c_g & 0 \\ -c_g & c_2 + c_g + c_3 & -c_3 \\ 0 & -c_3 & c_3 \end{bmatrix} \quad (36)$$

Using an inertial control parameter range of $0.05 \leq \eta \leq 0.55$, a generator damping range of $50 \leq c_g \leq 3000$ Ns/m, and a spring stiffness $k_3 = 1000$N/m, power at each frequency is found by solving a 2D optimization problem maximizing power where the control variables are $c_g$ and $\eta$. The plot given by Fig. 14, compares power capture between fixed spar designs with and without a fictitious tuning system to the steady state dynamics solution of the 3-body system represented by Eqs. 34-36 with optimal generator damping and inertial control settings (given by Fig. 15). The power plot of Fig. 14 indicates that the optimal

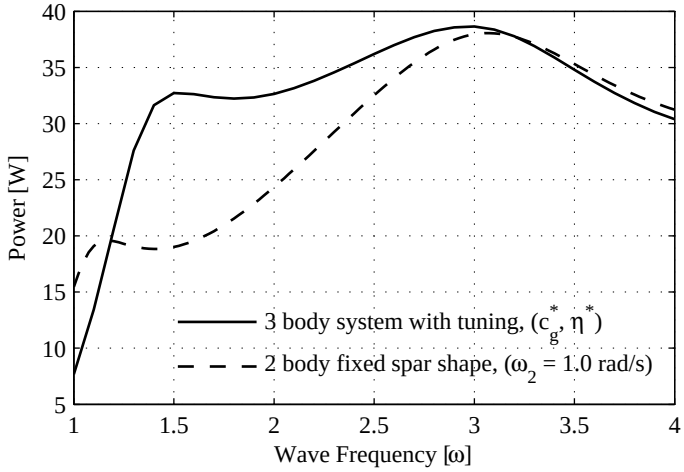


Fig. 14. Power for the tuned 3-body vs. the fixed spar shape 2-body

frequency response expected from previous sections can be achieved over most of the frequency range. At most frequencies, improved power capture can be achieved over a 2-body design of the same total mass with no tuning. However; at the extreme low end of the frequency range, the 2-body equivalent-mass system out performs the tuned 3 body system. The response amplitudes of the tuned 3-body system given in Fig. 16

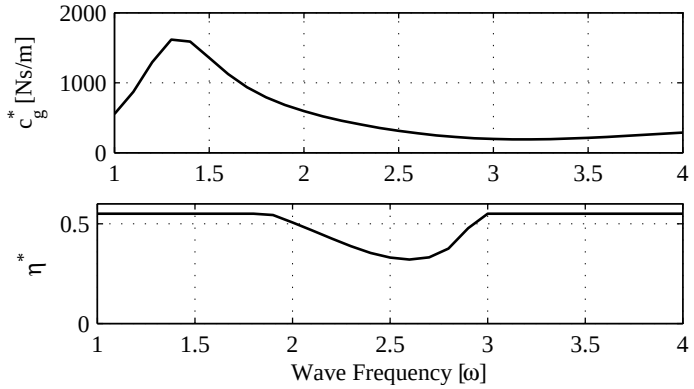


Fig. 15. Optimal control parameters for the tuned 3-body

show the that all responses are less than the wave height. The reaction mass motion is about 1/5 of the wave height which is far less than the space available for it to safely oscillate inside the spar. These response amplitudes will be used for mechanical design purposes in the future. Further, the phase responses are given by Fig. 17. The plot shows that the float leads the spar between 25 and 90 degrees over the frequency range, and the reaction mass phase is always very close to the spar. Specifically, a large power benefit is attainable in the lower half of the frequency range with a peak at 1.5 rad/s. The power benefit could be attributed to a greater

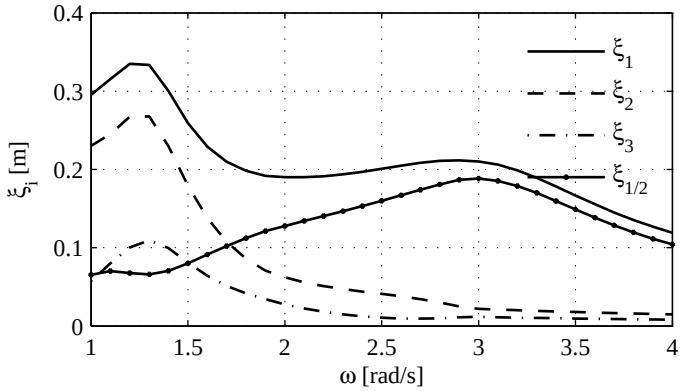


Fig. 16. Tuned 3-body response amplitudes (wave height $H = 0.5$m)

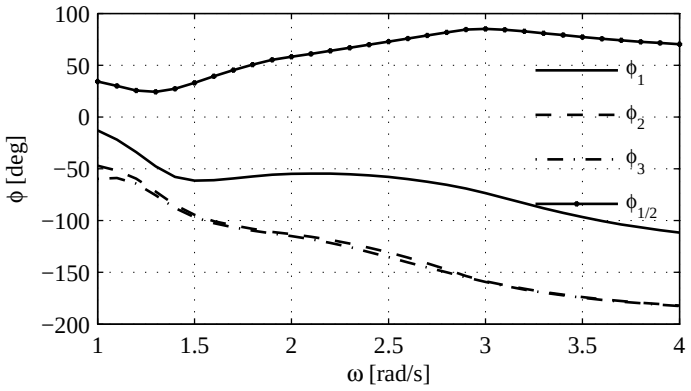


Fig. 17. Tuned 3-body response phases

contribution of mode $X_1$ associated with eigenvalue $\lambda_1$, to the steady state heave displacement solution. This performance benefit would have a drastic effect on the overall performance of a full-scale device since these waves correspond to much more energetic ocean waves. The design and tuning methodology presented allows an *a priori* selection of the spar and float shapes and sizes to target higher frequency waves that normally occur in the summer months and then rely on frequency response tuning to capture more energy energy from the lower frequency waves which normally occur in the winter months.

## CONCLUSIONS

The effects of natural frequency adjustment of the spar of a two-body "spar-float" heaving point absorber have been investigated using a simplified heaving dynamics model. The results have been shown in terms of relative motion for an un-coupled WEC, and power absorption for a coupled WEC. The output of an optimization has provided the choice for both the spar natural frequency and viscous power take-off damping coefficient. Results from this design study indicate that significant power absorption improvements at low frequencies could be derived (over an un-controlled WEC of the same mass) if a system could be developed to alter the frequency response of the spar. Subsequently, a description and analysis of a novel mechanical system for use with a reaction mass to provide frequency response tuning capability was given which is predicted provide power absorption improvements of upto 80% in a critical area of the wave frequency range.

## ACKNOWLEDGMENTS

This work was funded by Mathematics of Information Technology and Complex Systems (MITACS) under an ACCELERATE BC Internship program, the National Science and Engineering Research Council (NSERC), and SyncWave Energy Inc.

## REFERENCES

Alves, RM, and Batista, RC (1999). "Active/passive control of heave motion for TLP type offshore platform," *Proceedings of the International Offshore and Polar Engineering Conference*, vol. 1, pp. 332–338.

Beatty, SJ, Buckham, B, and Wild, P (2007). "Modeling, Design and Testing of a Two-Body Heaving Wave Energy Converter," *in Proceedings of the International Society of Offshore and Polar Engineers, ISOPE 2007, Lisbon Portugal*.

Bjarte-Larsson, T, and Falnes, J (2001). "Long-wavelength approximation of wave force on two-body axisymmetric system," *in Proceedings of the International Offshore and Polar Engineering Conference*, Stavanger, Norway, vol. 3, pp. 244–249.

Bracewell, RH (1990). *Frog and PS Frog: A Study of Two Reactionless Ocean Wave Energy Converters*, Ph.D. thesis, Lancaster University.

Clauss, G, Lehmann, E, and Ostergaard, C (1992). *Offshore Structures - Conceptual design and hydromechanics*, vol. 1, Springer-Verlag.

Falnes, J (2002). *Ocean Waves and Oscillating Systems: Linear Interactions including Wave Energy Extraction*, Cambridge University Press.

Gerber, J (2007). "United States Patent Application No. US 2007/0068153 A1 - Tunable Wave Energy Converter," USPTO.

Korde, UA (1999). "On providing a reaction for efficient wave energy absorption by floating devices," *Applied Ocean Research*, vol. 21, no. 5, pp. 235–248.

Protter, N, Beatty, SJ, and Buckham, BJ (2007). "PCT PATENT NO. WO 2007/137426 A1 - Wave Energy Converter," World Intellectual Property Organization.

## Appendix C

# Integration of a Wave Energy Converter into the Electricity Supply of a Remote Alaskan Island

# Integration of a wave energy converter into the electricity supply of a remote Alaskan island

Scott J. Beatty[a,*], Peter Wild[a], Bradley J. Buckham[a]

[a] *University of Victoria, Department of Mechanical Engineering, PO Box 3055, Stn. CSC, Victoria, BC, V8W 3P6, Canada*

**Abstract**

The electrical power integration of a heaving point absorber wave energy converter to a remote island community of population 100 is investigated. A wave resource assessment, taking into account the local geography, is completed. The operational concept and specifications of the wave energy converter are presented. A detailed description of the frequency domain modelling and control approach used to estimate *in situ* performance of the wave energy converter is given. Time series comparisons are made between wave power capture and community electrical demand. Analyses of electrical grid penetration ratios suggest that a deployment of a single offshore wave energy converter of 100kW capacity could be a feasible renewable electricity source for the island.

*Key words:* Wave energy, grid integration, point absorber, marine energy

## Nomenclature

| | |
|---|---|
| $A$ | wave amplitude |
| $A_j$ | amplitude of the $j$th frequency component in the spectrum |
| $\underline{C}$ | WEC damping matrix |
| $E$ | total energy per unit surface area of a sea-state |
| $E_{dem}$ | total community electrical energy demand [Joules] |
| $E_{wec}$ | total electrical energy delivered by WEC [Joules] |
| $H$ | height of a regular (monochromatic) wave, $H = 2A$ |
| $H(\omega)_{1/2}$ | relative motion transfer function |
| $H_s$ | significant wave height |
| $H_{dir}$ | primary wave direction |
| $J$ | rotational inertia |
| $\underline{K}$ | WEC stiffness matrix |
| $\underline{M}$ | WEC mass matrix |
| $N$ | number of spectral components |
| $\bar{P}(H_s, \omega_p)$ | WEC power capture in irregular seastate defined by $(H_s, \omega_p)$ |
| $P(\omega)$ | WEC power capture in the frequency domain |
| $P_{dem}$ | community electrical power demand [Watts] |

*Corresponding author. Tel: 1-250-472-4903; Fax: 1-250-721-6051.
*Email addresses:* scottb@uvic.ca (Scott J. Beatty)

| | |
|---|---|
| $P_{wec}$ | electrical energy delivered by WEC [Watts] |
| $S(\omega)$ | wave spectral density [$\mathrm{m}^2/\frac{\mathrm{rad}}{\mathrm{s}}$] |
| $S(\omega)_s$ | structural response spectral density |
| $T_e$ | energy period |
| $T_p$ | peak wave period |
| $\Delta\omega$ | frequency bin width |
| $\hat{\xi}_1, \hat{\xi}_2, \hat{\xi}_3$ | complex amplitude displacement of float, spar, slug respectively |
| $\hat{\xi}_{1/2}$ | complex amplitude of float to spar relative displacement |
| $\hat{a}_{01}, \hat{a}_{02}$ | fluid acceleration at depth $z_{P1}$, $z_{P2}$ respectively |
| $\hat{v}_{01}, \hat{v}_{02}$ | fluid velocity at depth $z_{P1}$, $z_{P2}$ respectively |
| $\mu$ | generation efficiency |
| $\omega$ | frequency of a regular (monochromatic) wave |
| $\omega_j$ | frequency of the $j$th component in the wave spectrum |
| $\omega_p$ | peak frequency, $\omega_p = 2\pi/T_p$ |
| $\rho$ | water density $\approx 1020$ [$\mathrm{kg/m}^3$] |
| $\vec{f_e}$ | excitation force vector |
| $\vec{x}$ | vector of body displacements |
| $c_1, c_2, c_3$ | damping coefficient of float, spar, slug respectively |
| $c_g$ | generator damping coefficient |
| $c_g^*(H, \omega)$ | optimal generator damping coefficient |
| $g$ | acceleration due to gravity |
| $h$ | water depth |
| $i$ | imaginary number |
| $j$ | index for spectral components ($j$th component) |
| $k$ | wave number |
| $k_1, k_2, k_3$ | (hydrostatic) stiffness of float, spar, slug respectively |
| $l$ | ballscrew lead in meters per radian |
| $m_1, m_2, m_3$ | mass of float, spar, slug respectively |
| $m_4^*(H, \omega)$ | optimal inertial control parameter |
| $\widehat{m}_n$ | $n$th spectral moment |
| $z_{P1}, z_{P2}$ | reference depth for float, spar resepectively |

## 1. Introduction

St. George Island (population 100) is part of the Pribilof Island group located in the Bering Sea, 350 km North of the Aleutian Islands. This is an extremely isolated location where fishing is the primary commercial activity. The residents of St. George Island, are investigating possible uses of renewable energy to reduce the financial and environmental costs associated with their current dependence on electricity derived from the combustion of diesel fuel. Part of this investigation is focused on the use of the plentiful ocean wave energy resource of the region. Researchers at the University of Victoria and SyncWave Systems Inc. have conducted an initial study of the application of their co-developed wave energy converter (WEC) technology for electricity supply to the St.George Island electrical grid.

Several previous studies have investigated the feasibility of interconnection of wave power devices, mainly with medium-sized communities. Babarit et al [1] investigated the potential synergy of wind energy and wave energy (applying their SeaREV device) with various storage

scenarios. They discuss the potential for improved energy independence through a study of import/export balance of electricity supply for a French island community of 5000 inhabitants. St. Germain [2] simulated the connection of various WEC devices to a coastal community grid in Western Canada with various storage scenarios. The feasibility of wave energy is discussed in terms of grid capacity issues and economics. Dunnet and Wallace [3] provide a general comparative performance evaluation of representative WEC's at various locations on Canada's coasts for which wave buoy is available from the Canadian Marine Environmental Data Service. They indicate the most economical locations using economic analyses of the devices, but do not consider community interconnection issues other than proximity to urban centers.

Many studies have been done on hybrid renewable energy/diesel systems for remote communities. Singal et al [4] investigated the economic feasibility of the replacement of a PV-diesel system with a system with biogas, biomass gasification, and solar PV sources to a group of islands in India. Dalton et al [5] provide a feasibility analysis of using Wind and solar PV sources to offset diesel generation for remotely located tourist accommodations. They use net present cost and payback time as indicators to rate different storage scenarios while reporting sensitivities to carbon taxes and diesel fuel price variation.

Singal et al [4], Dalton et al [5] and numerous other studies show that the integration of well-established renewable energy technologies with small scale loads is not only technically manageable due to the dispatchability of diesel generation, but also is economical due to the high cost of diesel generation.

Currently, wave energy technology is not well-established and the installed cost of electricity from wave energy converters is high in comparison to other renewable sources. Acceleration of wave energy research activity, successful ocean deployments, and convergence to standardized designs are all expected to improve trust in the technology and significantly reduce installed wave energy costs worldwide. However, if progress is to be made, wave energy proponents must deal with the present socio-economic landscape, and identify current financially realistic applications of the technology.

The goal of this study is to assess the technical feasibility of a WEC connection to the island of St. George. Further, this study is intended to lay the foundation for investigations of specific design and control elements required for wave/diesel hybridization of small remote electrical grids. Calculated from a relatively robust estimations of the wave resource and device performance, grid penetration levels and fuel savings estimates are used as metrics for the feasibility analysis.

First, a detailed wave resource assessment is completed for evaluation of wave power capture. The most likely deployment location is chosen in consideration of various constraints, both general and site specific, associated with the offshore WEC. Next, descriptions of the WEC device operation and mechanical systems are presented. The *in situ* performance of the wave energy converter is computed at the deployment location by interpolation of power capture results obtained using previously developed WEC dynamics models [6]. Lastly, time series of the electrical demand and WEC power delivery are compared in terms of grid penetration ratios.

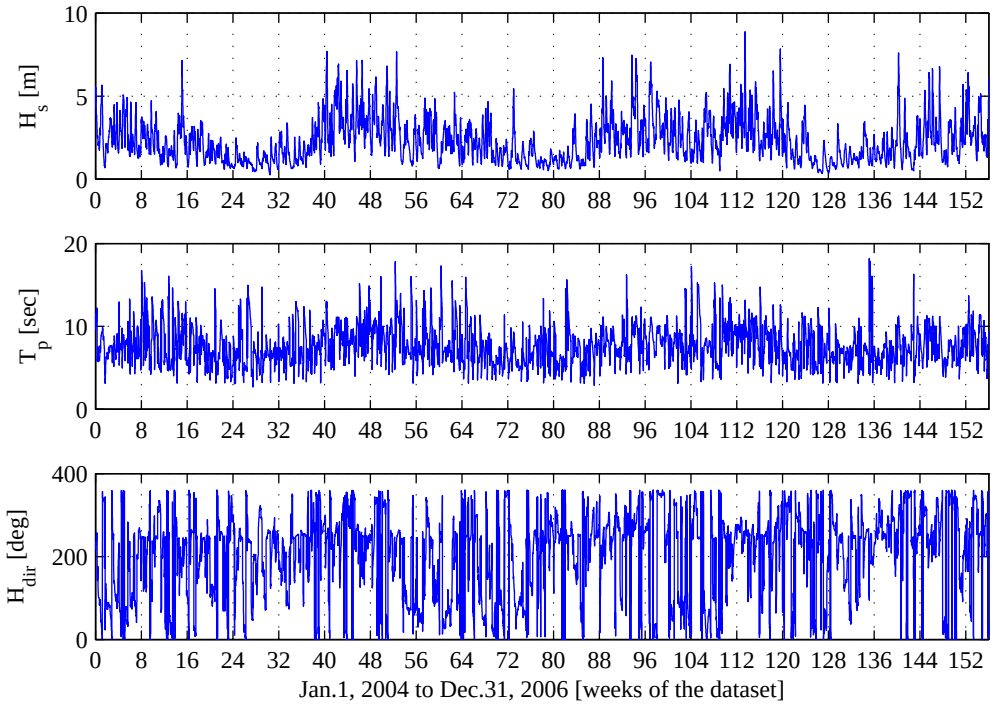


Figure 1: Hourly significant wave height $H_s$, peak period $T_p$, and primary direction $H_{dir}$.

## 2. Wave Resource Assessment

The wave resource assessment was based on data obtained from archived results of the US NOAAs numerical wave forecast model Wavewatch III [7]. The archived dataset, taken from the nearest available grid point to St.George Island, is the hourly time series shown in Figure 1. For each hourly data point in this figure, $H_s$, significant wave height, $T_p$, peak period, and $H_{dir}$, primary direction respectively represent the average of highest one third wave heights, the wave period at which the greatest energy is associated, and the direction from which the greatest energy is associated.

### *2.1. Deployment Location*

The expected deployment site is roughly 3 km to the West-South-West of Zapadni Bay in a water depth of 40 meters (see Figure 2). There are three reasons for the choice of location. First, broken ice-flows are known to arrive from the north once in ten years [8] and the effects of such ice-flows on offshore wave energy converters could be disastrous. Second, since Zapadni Bay is the location of the harbour on St.George Island, significant logistical benefits are expected in terms of distances traveled for deployment, maintenance, and cable laying operations. Third, the electrical grid extends to the harbour in Zapadni Bay, so there would be little on-shore infrastructure requirements to connect a WEC at this location.

### *2.2. Directional Screening*

The Wavewatch III model grid does not resolve small land masses such as the Pribilof Islands. The wave data was, therefore, post-processed to take into account the blockage

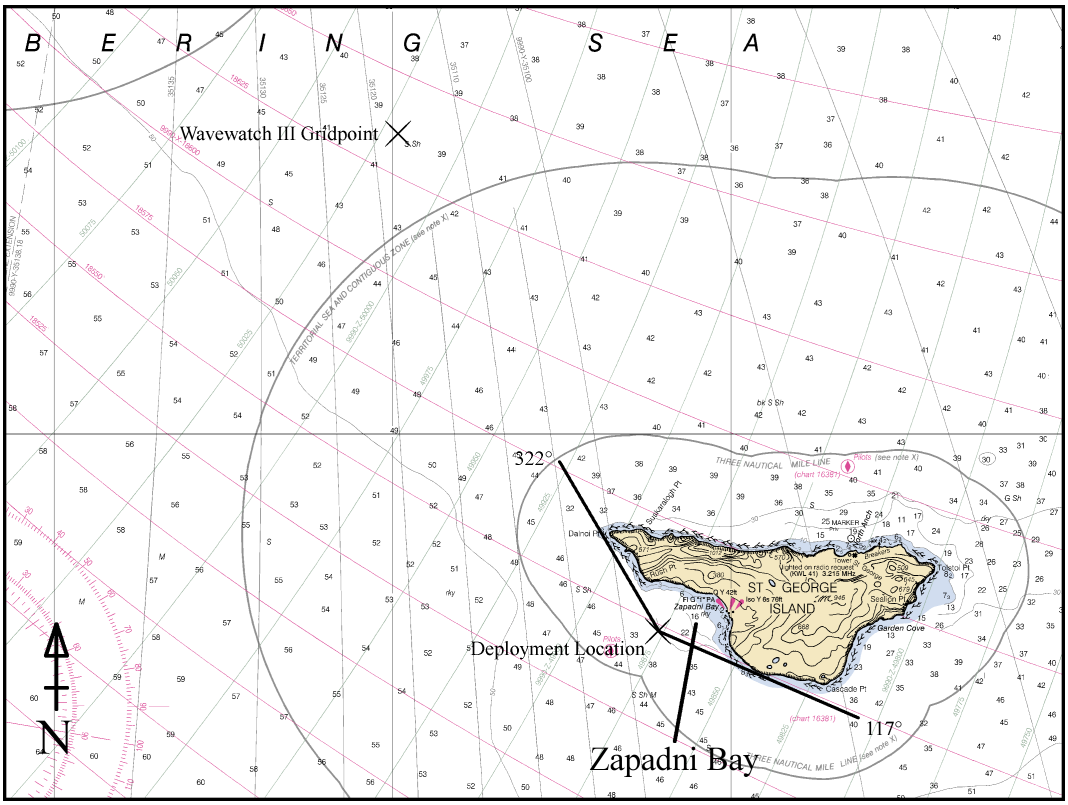


Figure 2: Nautical Chart indicating deployment location and Wavewatch III grid point with respect to St. George Island. Lines outward from deployment location indicate screening directions in degrees relative to true north. Depth soundings are in fathoms. Image Courtesy of the US National Oceanographic and Atmospheric Association(NOAA)[9]. Do not use for navigational purposes.

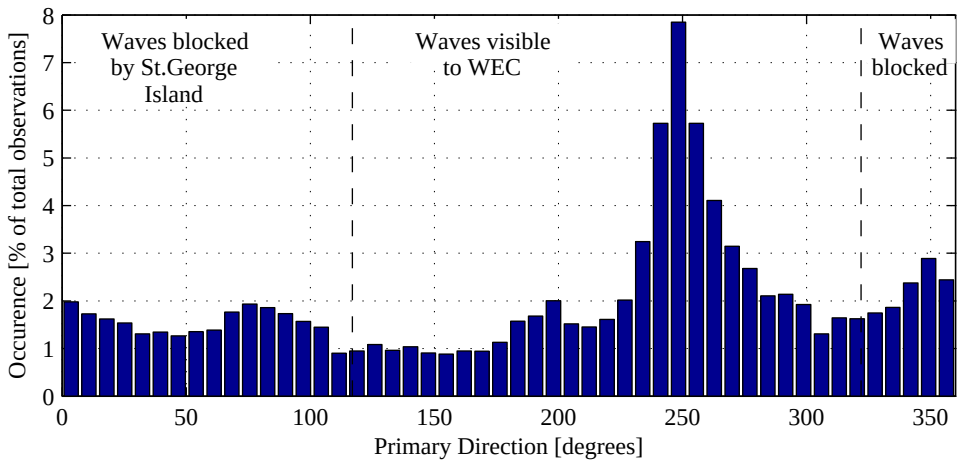


Figure 3: Histogram of primary wave direction observations. Dashed lines indicate the boundaries of WEC range of 'visibility'.

of waves by the island. Neglecting refraction effects, all sea-state records with a primary direction outside the WEC range of 'visibility' (directions indicated with lines projecting outward from the deployment location in Figure 2) were attenuated. Attenuation was done by setting $H_s = 0$ for corresponding wave records. The number of samples that required attenuation comprise 37% of the samples in the raw dataset. Notice from Figure 3, that the most frequently occurring waves approach from approximately 250° and are due to storms to the south west of the island. Although the protected deployment location reduces the overall power capture of the device, the prevailing seas are still available to the WEC. After post-processing for wave direction, the joint probability of sea state parameters $H_s, T_p$ was calculated by creating a two dimensional histogram using a 20x20 matrix of $H_s, T_p$ bins. The joint probability results are shown in the contour plot of Figure 4. The cross in Figure 4 indicates the prevailing (most frequently occurring) sea state is $(H_s, T_p)$ =(1.1 m, 6.1 sec).

### *2.3. Spectral representation*

The spectral density function, also known as the 'wave spectrum' of a sea-state, is a continuous function that represents the instantaneous distribution of variance in water surface elevation across the frequency range. If the physical constants $\rho g$ are applied (i.e. $\rho g S(\omega)$), the spectral density function represents the distribution of wave energy across the frequency range. A wave spectrum that is representative of, or energy equivalent to, a sea-state reported by the parameters $H_s$ and $T_p$, can be synthesized using the parameters $H_s$ and $T_p$ and one of the established semi-empirical relationships. The Pierson–Moscowitz spectral form, given by Eq. (1), which assumes fully developed seas is used in this work.

$$S(\omega) = \frac{5}{32}\frac{\omega_p^4 H_s^2}{\pi\omega^5}\exp\left(\frac{5}{4}\frac{\omega_p^4}{\omega^4}\right) \tag{1}$$

Peak frequency, $\omega_p$, and peak period, $T_p$, are the wave frequency and corresponding period at which $S(\omega)$ is a maximum. The quantities $\omega_p$ and $T_p$ can be used interchangably through a simple conversion $\omega_p = 2\pi/T_p$.

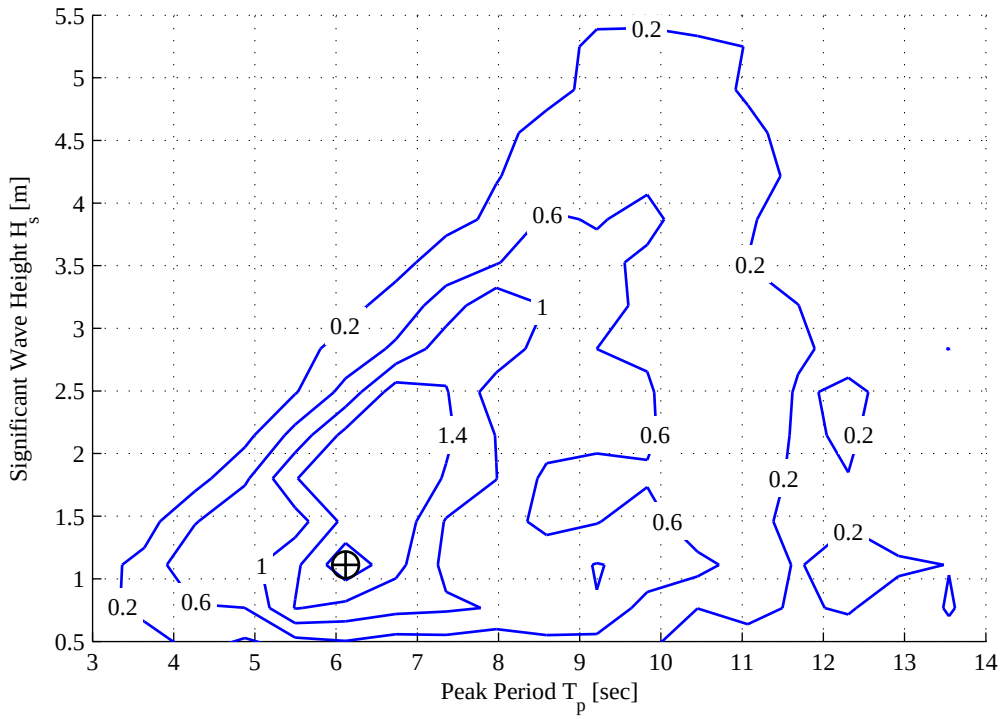


Figure 4: Joint probability of $H_s$ and $T_p$. Contour labels indicate the percent occurrence in the dataset. The cross indicates the prevailing sea state inside the 1.8% contour.

For practical purposes, the continuous spectral density function must be discretized into $N$ frequency components, each of width $\Delta\omega$. To obtain the amplitude of the wave associated with the $j$th frequency component, one must use Eq. (2):

$$\frac{1}{2}A_j^2 = S(\omega_j)\Delta\omega \tag{2}$$

Moments of the spectral density function are used for fitting of spectral forms to discrete wave measurements. The $n$th moment, in continuous and discrete forms [10], is given by Eq. (3).

$$\widehat{m}_n = \int_0^\infty \omega^n S(\omega) d\omega = \sum_{j=1}^{N} \omega_j^n S(\omega_j)\Delta\omega \tag{3}$$

The total energy per unit surface area in the sea-state is directly proportional to the zeroth moment, the area under the spectral density function, as shown in continuous and discrete forms by Eq. (4).

$$E = \rho g \widehat{m}_0 = \rho g \int_0^\infty S(\omega) d\omega = \rho g \sum_{j=1}^{N} S(\omega_j)\Delta\omega \tag{4}$$

The mathematical definition of significant wave height, follows from the zeroth moment of

the continuous and discrete spectral forms given by Eq. (5).

$$H_s \equiv 4\sqrt{\widehat{m}_0} = 4\sqrt{\int_0^\infty S(\omega)d\omega} = 4\sqrt{\sum_{j=1}^{N} S(\omega_j)\Delta\omega} \tag{5}$$

*2.4. Prevailing wave resource*

The 'energy period', $T_e$, represents the period of a sinusoidal wave that would carry the same energy as the seastate. Energy period is defined by the ratio of spectral moments as given in Eq. 6.

$$T_e \equiv 2\pi\frac{\widehat{m}_{-1}}{\widehat{m}_0} \tag{6}$$

In this work, energy period (Eq. (6)) is calculated for each time using an $N = 256$ component Pierson-Moscowitz spectral form. Cornett [11] made the approximation $T_e \approx 0.9T_p$ assuming a JONSWAP spectral form for Canada's coastlines. Applying Eq. (6) for the wave data in this work, calculations of the ratio of energy period to peak period yield the range $0.857 \leq \frac{T_e}{T_p} \leq 0.981$ with the mean of 0.863. Therefore it appears the approximation by Cornett is reasonably valid for the spectral assumptions and wave data in this work.

To estimate the wave power per meter of wave front in a given sea state [10], Eq. (7) can be used.

$$J = \frac{1}{64\pi}\rho g^2 T_e H_s^2 \tag{7}$$

The incident wave power per meter of wave front from Eq. (7) at the prevailing sea state, $(H_s, T_p)$ =(1.1 m, 6.1 sec), is 3.2 kW/m when applying Eq. (6) and 3.3 kW/m when applying the approximation $T_e \approx 0.9T_p$. Finally, the mean incident wave power (over the 3 year data set) is 26 kW/m when applying Eq. (6) and 28 kW/m when applying the approximation $T_e \approx 0.9T_p$. The discrepancy between the incident power at the prevailing sea-state and the mean incident power is because the incident wave power is proportional to the square of significant wave height and extreme sea states dispersed through the data set tend to drive up the annual mean incident wave power.

## 3. WEC Operating concept

The SyncWave WEC, hereafter referred to as 'the WEC', is classified as a self–reacting point absorber. Point absorbers are omni-directional—they respond equally to waves from all directions. The WEC is comprised of the two surface piercing components shown in Figure 5. The first is a central vertical cylinder called a spar and the second is an annular float. In response to wave motion, the two bodies oscillate vertically and out-of-phase with each other. These two bodies are coupled together by hydraulic rams which drive a generator such that the relative motion between the bodies causes the generator to produce electricity. Summary specifications of the WEC device used in this case study are given in Table 1. The mass given in Table 1 includes both the mass of structural components and of the ballast. Electrical generator efficiencies and line losses are approximated in this work by an efficiency factor $\mu = 0.75$ applied across the frequency response of the WEC.

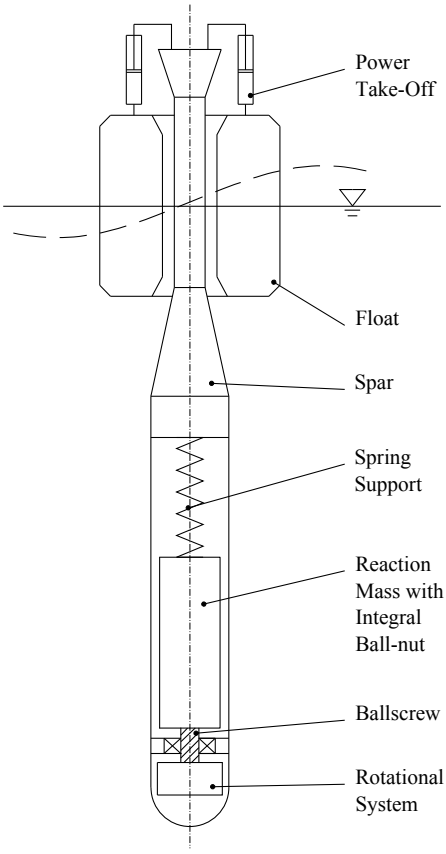


Figure 5: Schematic of the WEC.

Table 1: WEC Design Specifications

| Parameter | Value |
|---|---|
| Mass of structure | 166,000 kg |
| Outer diameter | 5 m |
| Draft | 30 m |
| Capacity | 100 kW |

### *3.1. Frequency Response Tuning*

To maximize power production, the WEC is actively tuned to ensure that its response is approximately optimal over the range of most probable sea-states. The tuning system is also used to ensure device survival in extreme sea-states. If un-controlled during storm events, the relative motion between components could be excessively high, potentially leading to damage to the WEC.

In addition to adjustments made to the generator, mechanical adjustments are made to an inertial tuning system housed within the spar. As shown by Figure 5, an internally housed, spring-supported, reaction mass is coupled to a rotational system using a ballscrew connection. By way of a mechanical linkage, adjustments can be made to the inertia of the rotational system. This, in turn, affects the dynamic behavior of the WEC by changing the inertial resistance to relative motion of the slug within the spar and, consequently, the resistance to extension/compression of the spring support. In terms of the device dynamics model, changes are the $J/l^2$ entries in the mass matrix given by Eq. (10). Further detail on the inertial control system can be found in previous contributions [6, 12].

## 4. Computation of *in situ* WEC performance

In this section, the detailed computations required to estimate the WEC power capture are presented in the following steps.

1. A linear dynamics model in the frequency domain is established for the device.
2. Optimization is used to establish control schedules to maximize power capture.
3. Control schedules are interpolated for calculation of power capture in irregular waves.
4. WEC Power delivery is computed for each hourly sea-state in the wave data.

### *4.1. Dynamics model*

Predictions of the float, spar, and reaction mass responses to incoming waves are made using a heave-constrained, linear dynamics model in the frequency domain. The model yields the resulting motions and power capture in response to a regular wave of amplitude $A$ and frequency $\omega$. The dynamics model represents the three-body system consisting of the float (body 1), spar (body 2), reaction mass (body 3), and the rotational system with moment of inertia, $J$ kgm$^2$ , ballscrew lead, $l$ in meters displacement per radian of rotation. The vector of body displacements is defined as follows.

$$\vec{x} = \begin{Bmatrix} \xi_1(t) \\ \xi_2(t) \\ \xi_3(t) \end{Bmatrix} \tag{8}$$

The governing dynamics equation, Eq. (9), follows:

$$\underline{M}\ddot{\vec{x}} + \underline{C}\dot{\vec{x}} + \underline{K}\vec{x} = \vec{f}_e \tag{9}$$

The mass, stiffness, and damping and matrices, given in Eqs. (10-12), were developed previously in [13].

$$\underline{M} = \begin{bmatrix} m_1 & 0 & 0 \\ 0 & \frac{J}{l^2} + m_2 & -\frac{J}{l^2} \\ 0 & -\frac{J}{l^2} & \frac{J}{l^2} + m_3 \end{bmatrix} \tag{10}$$

$$\underline{K} = \begin{bmatrix} k_1 & 0 & 0 \\ 0 & k_2 + k_3 & -k_3 \\ 0 & -k_3 & k_3 \end{bmatrix} \tag{11}$$

$$\underline{C} = \begin{bmatrix} c_1 + c_g & -c_g & 0 \\ -c_g & c_2 + c_g + c_3 & -c_3 \\ 0 & -c_3 & c_3 \end{bmatrix} \tag{12}$$

The wave excitation force vector for the system is given by Eq. (13). The third row entries (associated with the reaction mass) are zero because it is internally housed within the spar and thereofre has no external wave forcing.

$$\vec{f}_e = \left[ \begin{pmatrix} m_1\hat{a}_{01} \\ m_2\hat{a}_{02} \\ 0 \end{pmatrix} \frac{1}{A} + \begin{pmatrix} c_1\hat{v}_{01} \\ c_2\hat{v}_{02} \\ 0 \end{pmatrix} \frac{1}{A} + \begin{pmatrix} k_1 \\ k_2 \\ 0 \end{pmatrix} \right] A \tag{13}$$

The fluid velocity and accelerations, $\hat{v}_{01}, \hat{v}_{02}$ in Eq. 15 and $\hat{a}_{01}, \hat{a}_{02}$ in Eq. 14 respectively, established from Airy wave theory, are evaluated at "reference depths" $z_{P1}, z_{P2}$ for the float and spar. This is a common approach to the wave excitation force calculation for offshore structures [14, 15]. The wavenumber, $k$, is obtained from an iterative solution to the dispersion relation, calculated for each wave frequency $\omega$ considered.

$$\hat{a}_{01} = -\omega^2 \frac{\sinh(kz_{P1} + kh)}{\sinh(kh)} A, \quad \hat{a}_{02} = -\omega^2 \frac{\sinh(kz_{P2} + kh)}{\sinh(kh)} A \tag{14}$$

$$\hat{v}_{01} = i\omega \frac{\sinh(kz_{P1} + kh)}{\sinh(kh)} A, \quad \hat{v}_{02} = i\omega \frac{\sinh(kz_{P2} + kh)}{\sinh(kh)} A \tag{15}$$

The reference depth for any cylindrical body is assumed to be equal to its draft; However, the reference depth for a composite shape, such as the spar design given by Fig. 5, may be approximated by a weighted average of the protruding areas normal to the heave direction [13]. Assuming all bodies undergo steady state sinusoidal oscillations at the wave frequency $\omega$, Eq. (9) becomes:

$$\begin{gathered} [-\omega^2\underline{M} + i\omega\underline{C} + \underline{K}] \begin{Bmatrix} \hat{\xi}_1 \\ \hat{\xi}_2 \\ \hat{\xi}_3 \end{Bmatrix} = \\ \left[ \begin{pmatrix} m_1\hat{a}_{01} \\ m_2\hat{a}_{02} \\ 0 \end{pmatrix} \frac{1}{A} + \begin{pmatrix} c_1\hat{v}_{01} \\ c_2\hat{v}_{02} \\ 0 \end{pmatrix} \frac{1}{A} + \begin{pmatrix} k_1 \\ k_2 \\ 0 \end{pmatrix} \right] A \end{gathered} \tag{16}$$

An analytical solution, in terms of the complex amplitudes of the heaving displacements is found by matrix inversion of the combined dynamic matrix on the LHS of Eq. (16) multiplied by $\vec{f}_e$. An analytical expression for the relative float-spar displacement is found by Eq. 17.

$$\hat{\xi}_{1/2}(\omega) = \hat{\xi}_1(\omega) - \hat{\xi}_2(\omega) \tag{17}$$

Finally, applying the assumed power-take-off and transmission line efficiency $\mu$, the WEC power delivery in the frequency domain is given by Eq. (18).

$$P(\omega) = \mu \frac{1}{2} \omega^2 c_g |\hat{\xi}_{1/2}(\omega)|^2 \tag{18}$$

*4.2. Frequency domain control optimization*

A Sequential Quadratic Programming algorithm is used maximize power capture as given by Eq. (18). The first control variable is the generator damping coefficient, denoted $c_g$. The second control variable is an inertial control parameter, denoted $m_4$, which is related to the rotational system inertia $J$ and ballscrew lead $l$ by Eq. (19). The inertial control parameter, intuitively expressed in units of kilograms, represents the 'effective mass due to the rotational system.'

$$m_4 \equiv \frac{J}{l^2} \tag{19}$$

The constraints on the optimization consist of range limits on the decision variables and non-linear travel constraints to mitigate excessive relative motion between the WEC components, which could result in catastrophic failures.

The converged solutions of the optimization are used as 'schedules' for operation of the WEC across the domain of wave frequencies. Specifically, the optimal generator intensity and inertial control parameter which are functions of both wave height $H = 2A$ and wave frequency $\omega$ are denoted $c_g^*(H, \omega)$ and $m_4^*(H, \omega)$ respectively. They are plotted as surfaces in Figures 6 and 7 respectively.

*4.3. Application of optimal control results*

To apply the optimal control results from the frequency domain (which assume regular waves), to the irregular wave fields, the surfaces shown in Figures 6 and 7 are interpolated at the $H_s$ and $\omega_p = 2\pi/T_p$ pairing to yield the control decisions $c_g^*(H_s, \omega_p)$ and $m_4^*(H_s, \omega_p)$ for that hour. Note that the $H_s$ and $\omega_p$ pairing are stochastic sea-state parameters taken from an observed or modelled wave spectrum; whereas the horizontal axes of Figures 6 and 7, $H$ and $\omega$, are simple parameters to represent a regular (sinusoidal) wave.

Sea-states often occur that do not fit semi-empirical spectral forms, such as double peaked spectra arising from multiple storms, which would render the above control method non-optimal. However, because single peaked spectra are assumed for this study, the chosen method for control decisions is considered adequate to assess the general *in situ* performance of the WEC. Optimal control of WECs in complex seas-states is an important subject of ongoing research [16, 17] but it outside the scope of this work.

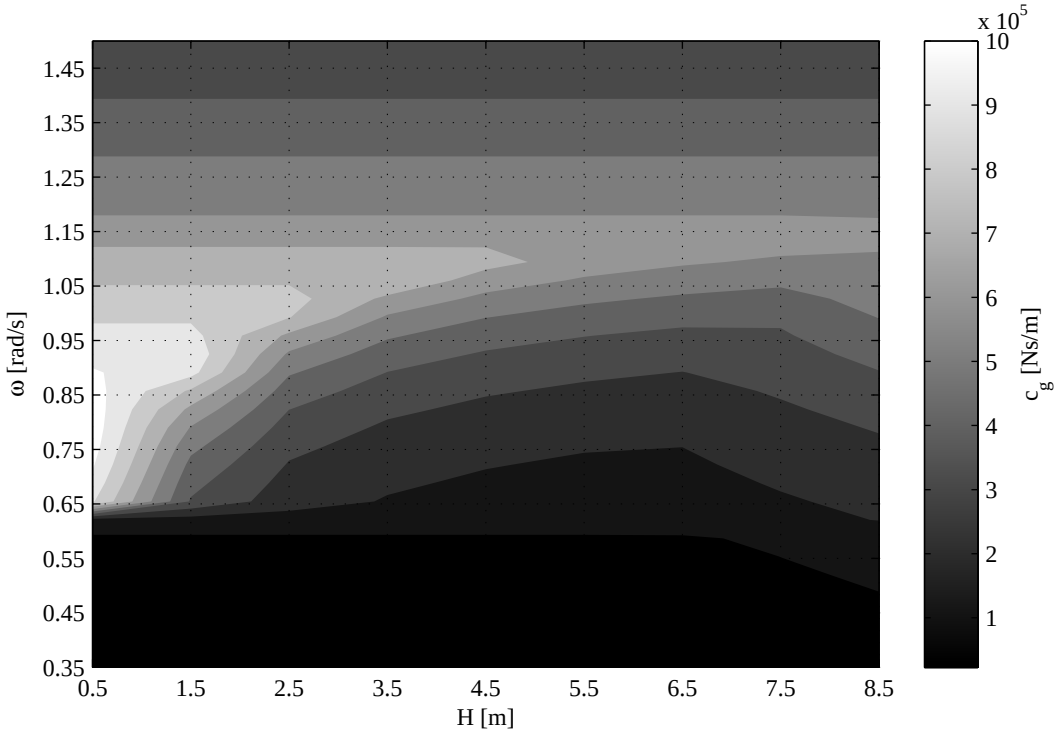


Figure 6: Constrained optimal generator damping schedule

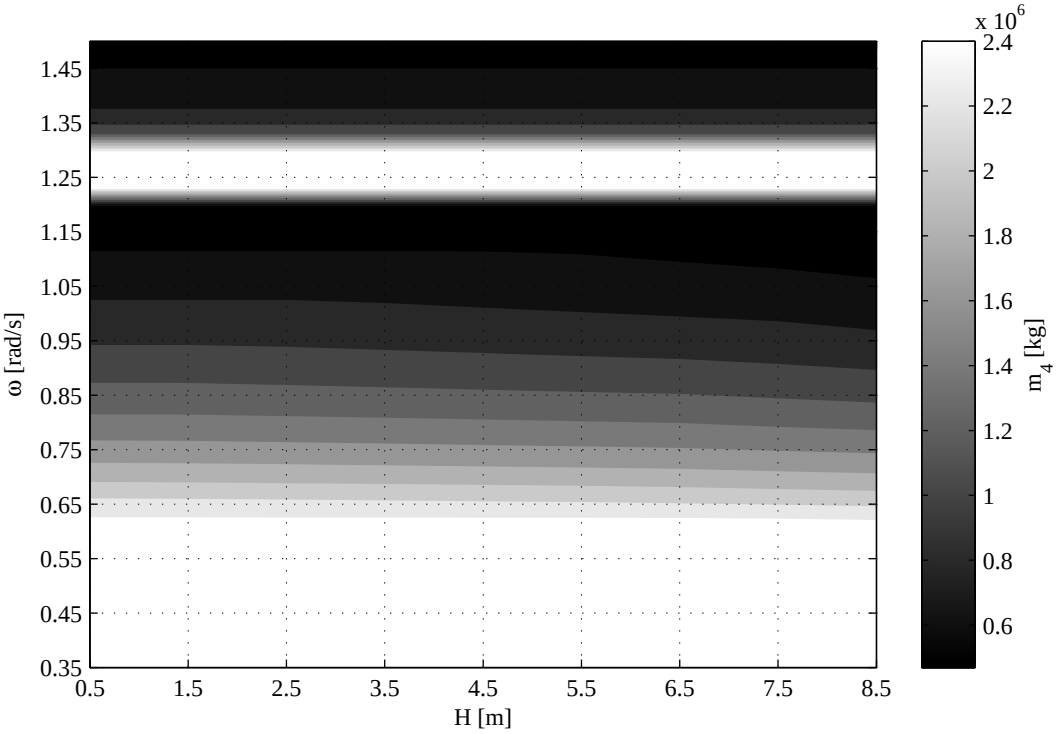


Figure 7: Constrained optimal rotational inertia schedule

*4.4. Performance estimation in irregular waves*

To establish an irregular wave field, a discretized Pierson–Moscowitz spectrum with frequency 256 components ($N = 256$), $S(\omega)$ is obtained for each of the hourly sea-state records $(H_s, T_p)$ by evaluating Eq. (1), as discussed in Section 2.3. The wave frequency range used is the typical range observed in the ocean ($0.2 \leq \omega \leq 2.0$ rad/s).

To estimate the WEC displacements, a normalized transfer function is obtained from Eq. (17), referred to as a response amplitude operator (RAO), by applying $c_g^*(H_s, \omega_p)$ and $m_4^*(H_s, \omega_p)$ in Eq. (9).

$$|H(\omega)_{1/2}| = \frac{\hat{\xi}(\omega)_{1/2}}{A} = \mathrm{RAO}_{1/2} \tag{20}$$

The wave spectral density can be multiplied by the square of the RAO to obtain the WEC response spectrum $S(\omega)_s$.

$$S(\omega)_s = |H(\omega)_{1/2}|^2 S(\omega) \tag{21}$$

The method of Eq. (21) is commonly used in the analysis of floating offshore structures. Further details regarding the usage and implicit assumptions to the equation can be found in [15] and [18]. The power associated with each of the $N$ wave components in a sea-state is a function of the relative motion response. By summing power contributions (each of the form of Eq. (18)) for each wave component, and utilizing Eq. (2), an equation for the mean power capture from the irregular wave field defined by $(H_s, \omega_p)$ is derived.

$$\bar{P}(H_s, \omega_p) = \mu \frac{1}{2} c_g^*(H_s, \omega_p) \sum_{j=1}^{N} \omega_j^2 2 S(\omega_j)_s \Delta\omega \tag{22}$$

If Eq. (21) is substituted into Eq. (22), the final relationship is:

$$\bar{P}(H_s, \omega_p) = \mu \frac{1}{2} c_g^*(H_s, \omega_p) \sum_{j=1}^{N} \omega_j^2 |H(\omega_j)_{1/2}|^2 2 S(\omega_j) \Delta\omega \tag{23}$$

Using the relative motion and optimal power take-off and frequency response control schedules, WEC power capture estimates are made for a range of sea-states, resulting in a WEC production matrix. The normalized production matrix is provided by Fig. 8, which provides power capture in kW, as a function of sea state $(H_s, T_p)$ or $(H_s, \omega_p)$. The production matrix is interpolated using the hourly sea-state data, in the form $(H_s(t), T_p(t))$, as discussed in Section 2 to yield a time series of WEC power delivery (see Fig. 9). The production matrix of Figure 8 has been interpolated over the directionally screened wave data to find the hourly output of the device during the years 2004 through 2007. Figure 9 shows that the maximum output reaches the capacity limit of 100kW and that the average output is 13kW, so the average capacity factor is 0.13.

## 5. St. George Island generating system

St. George Island's electrical power is currently supplied by four generators in total– two 175 kW units, one 350kW unit, and one 200kW unit [8]. In 2007, the diesel fuel cost for the island inhabitants was $US 1.32 per litre ($US 5.00 per US gallon) and the approximate overall fuel efficiency of the diesel generation system is 1.98 kWh per litre (7.5 kWh per US gallon).

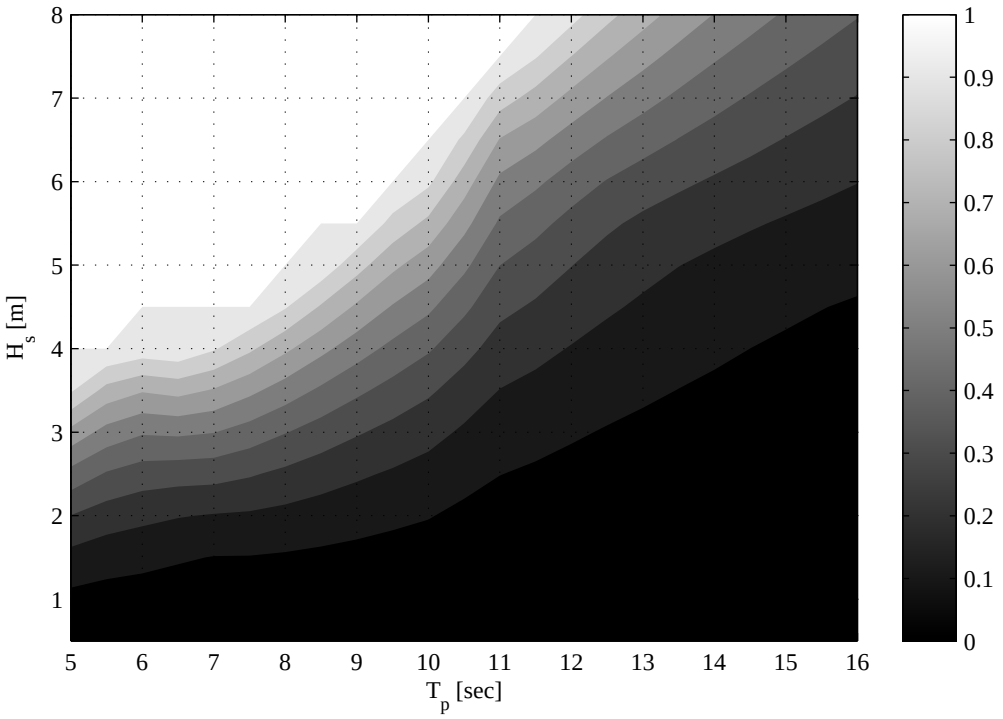


Figure 8: Normalized power capture vs sea-state for the WEC.

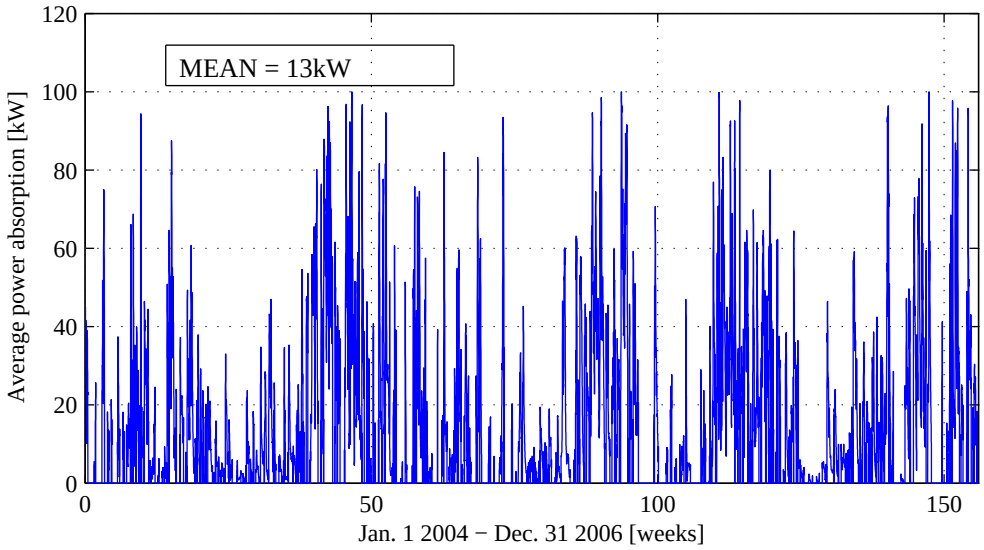


Figure 9: Simulated power capture for a single WEC unit.

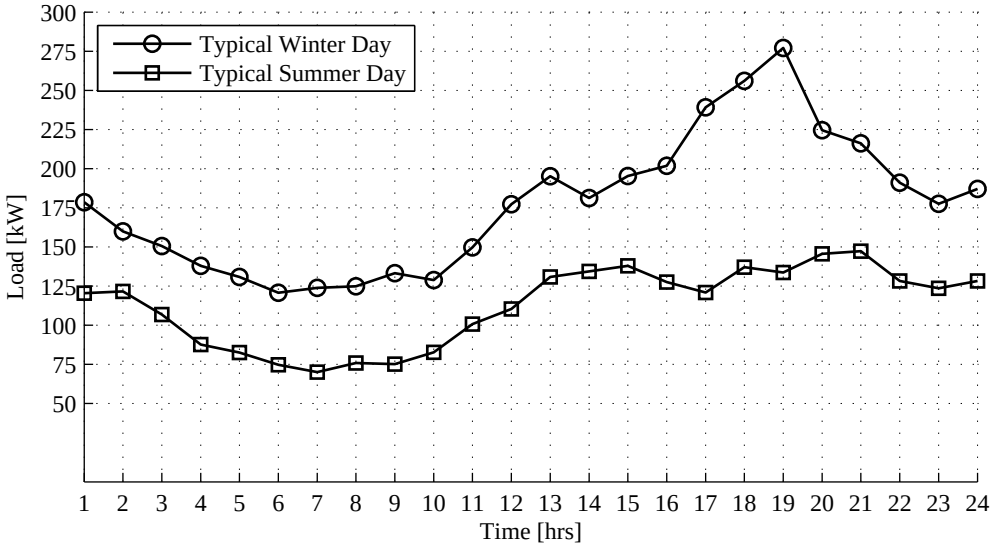


Figure 10: Daily electrical demand profiles derived from [19].

### *5.1. Community electrical load*

A summary of the overall electrical demand, as reported by the Mayor and Public Works manager of St.George during personal communication [8], is given by Table 2. An airstrip on the island intermittently demands up to 150 kW. One or more of the generators is manually ramped up and down by a human operator during aircraft take-off and landing, to power the runway lighting.

Table 2: St. George Island Electrical demand summary

| | Summer | Winter |
|---|---|---|
| Minimum | 70 kW | 150 kW |
| Average | 160 kW | 200 kW |
| Peak | 200 kW | 300 kW |

Because an hourly (rather than seasonal) data source for community load was required, the community load was also synthesized using the Alaska Village Electric Load Calculator, developed by NREL [19], which uses community census data [20] to scale typical Alaskan village load profiles. The output of the calculator is hourly load data for a typical year. For this study, the community load is simply repeated for three years to match the length of the wave data time series. The final result is an approximate set of electrical demand data extending from from Jan.1, 2004 to Dec.31, 2006. The demand profiles in the summer and winter are shown by Figure 10. As a check, the synthesized data reflect fairly closely the summary data provided in Table 2. It is believed that this fabricated time series is a reasonable approximation to the true demand profiles, within 10% error according to [19].

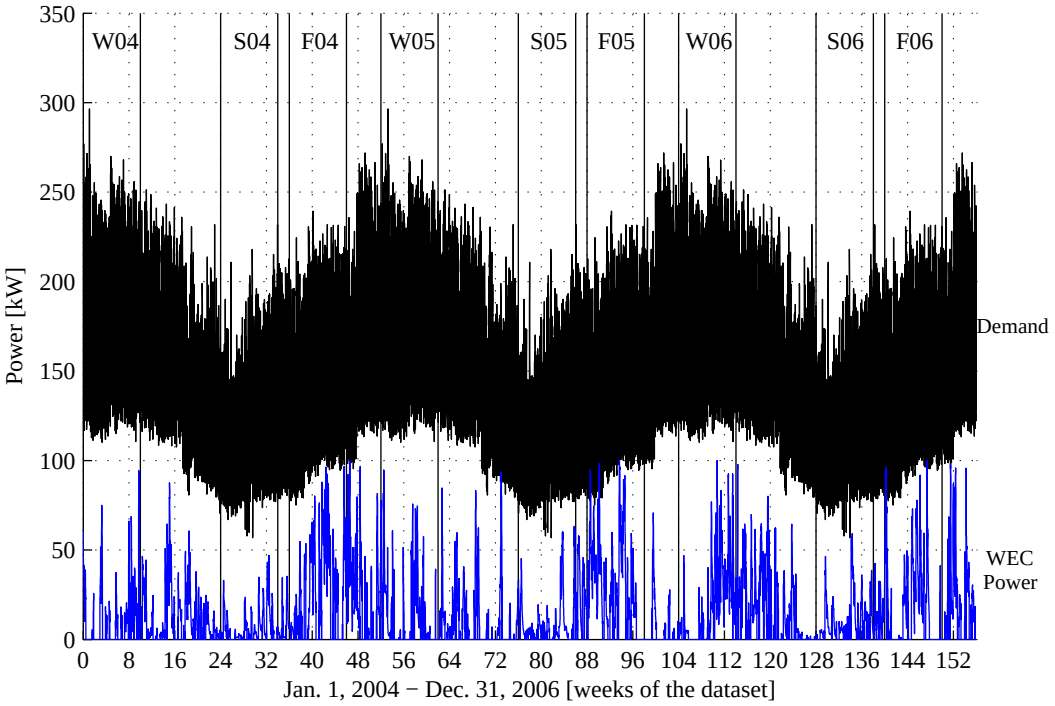


Figure 11: Longterm WEC and Demand comparisons.

## 6. Comparison of WEC power capture to community loads

### *6.1. Time-series*

Community demand is compared directly to the WEC electrical power generation over the entire time series in Figure 11. Note that the wave power follows a similar seasonal variation as the demand–the wave power is at a maximum when the energy is required most. Although the wave power roughly follows the trend of electrical demand, during the fall of each year, wave power ramps up much faster than electrical demand, causing potential for instantaneous power penetration to exceed 100%. During extreme seas, the 100kW capacity limit is reached.

Time series comparisons of WEC power capture to electrical demand are made for ten weeks in the summer, fall, and winter in Figures 12, 13, and 14 respectively. During the summer seasons (labelled S04, S05, S06 in Figures 11 and 12), both electrical demand and wave power capture are at a minimum. Summer maximum penetrations levels are on the order of 60%. During the fall seasons (labelled F04, F05, F06 in 11 and Figures 13), the community electrical demand is at an average level but wave power capture is at a maximum. The resulting maximum instantaneous penetration levels are shown to be 120%. During the winter seasons (labelled W04, W05, W06 in Figures 11 and 14), the community electrical demand is at a maximum, the wave power is at its peak availability, and maximum power penetrations are on the order of 75%.

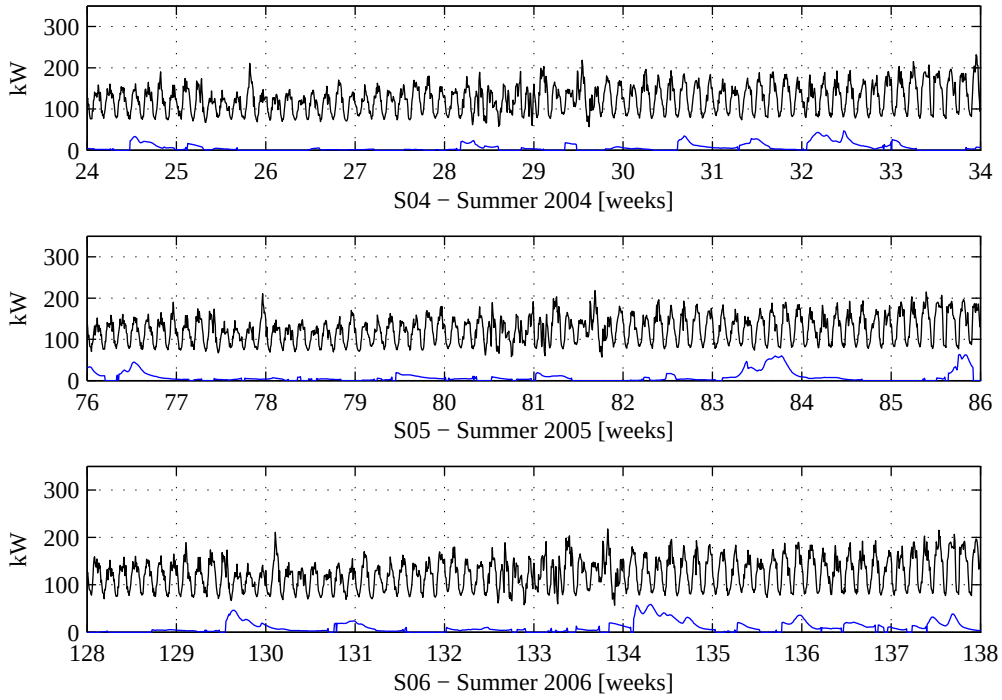


Figure 12: Ten week summer WEC power and demand comparisons

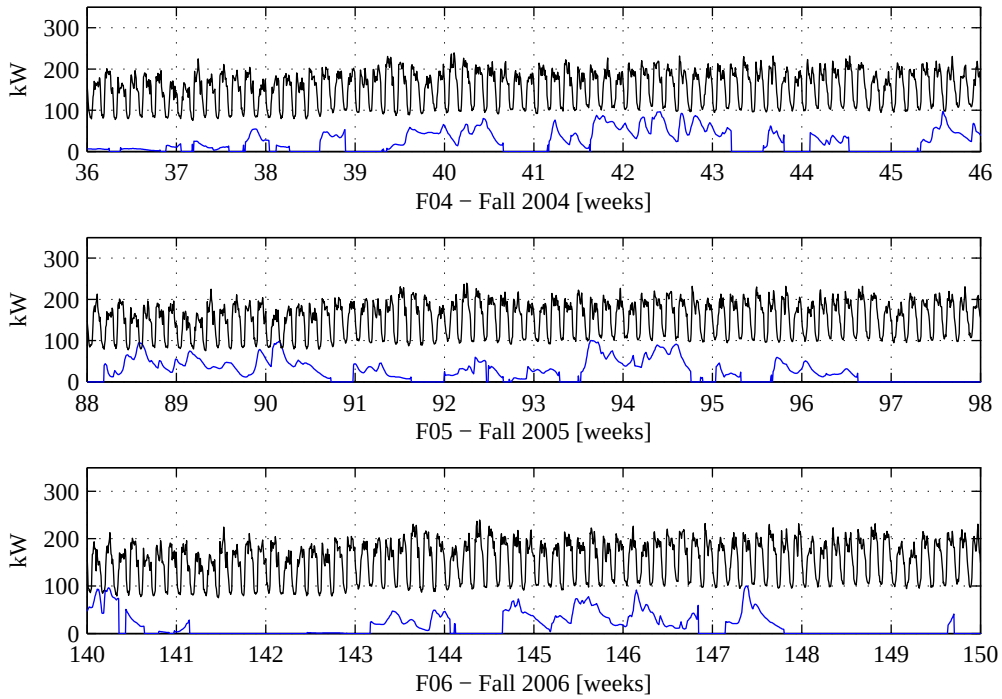


Figure 13: Ten week fall WEC power and demand comparisons.

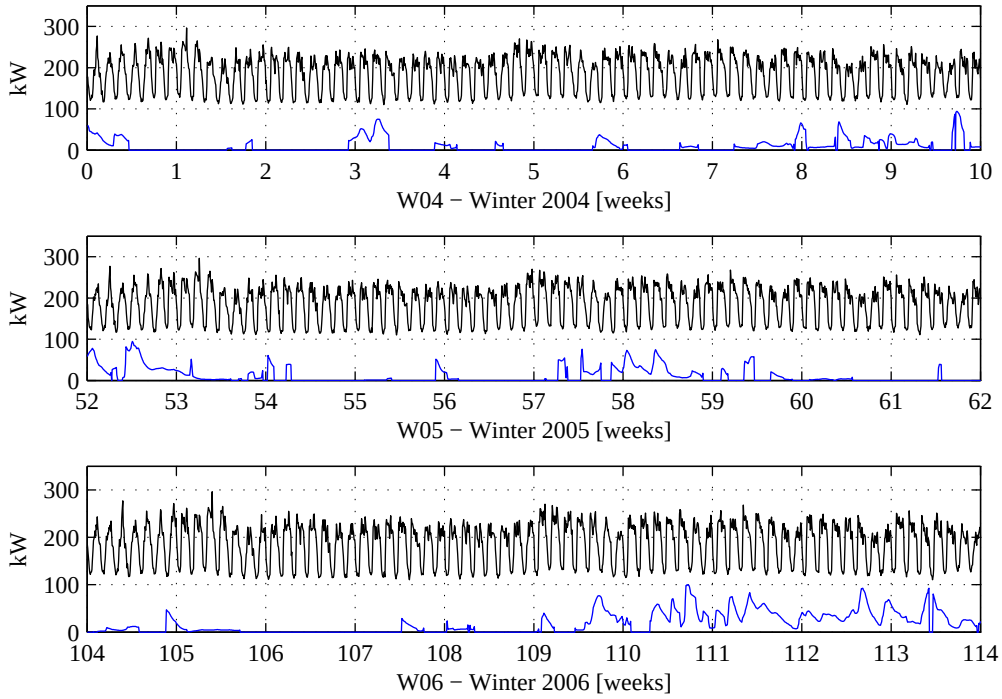


Figure 14: Ten week winter WEC power and demand comparisons.

### *6.2. Grid penetration*

The two definitions of penetration [21, 22] used in this study are:

$$\text{Energy penetration} = \frac{\text{Total energy delivered by WEC [kWh]}}{\text{Total energy demanded [kWh]}} \tag{24}$$

$$\text{Power penetration} = \frac{\text{Instantaneous power delivered by WEC [kW]}}{\text{Instantaneous power demand [kW]}} \tag{25}$$

By applying Eq. (25) at each time series point, a full time series of power penetration has been computed and plotted in Figure 15. The maximum power penetration levels are 90% to 120% and they occur in the fall months of every year. The energy penetration is 9% over the three years.

### *6.3. Discussion*

As penetration levels increase, the cost and complexity of grid integration strategies are known to increase. Gould et al [22] presents three classes (shown in Table 3) of grid penetration for wind-diesel hybridized electrical systems that are distinguished by the complexity and cost of integration. Although peak instantaneous power penetration exceeds 100% in the previous analysis, this occurs rarely enough that WEC generator system could be adjusted to ensure power penetration levels below 100%. As a result, it is viewed that the wave-diesel hybridized system of this study would be classified as a low to medium penetration system. According to Gould et al [22], the best operating strategy for the medium class combines full-time diesel generator operation with the dispatch of secondary loads, such as dissipative elements, when

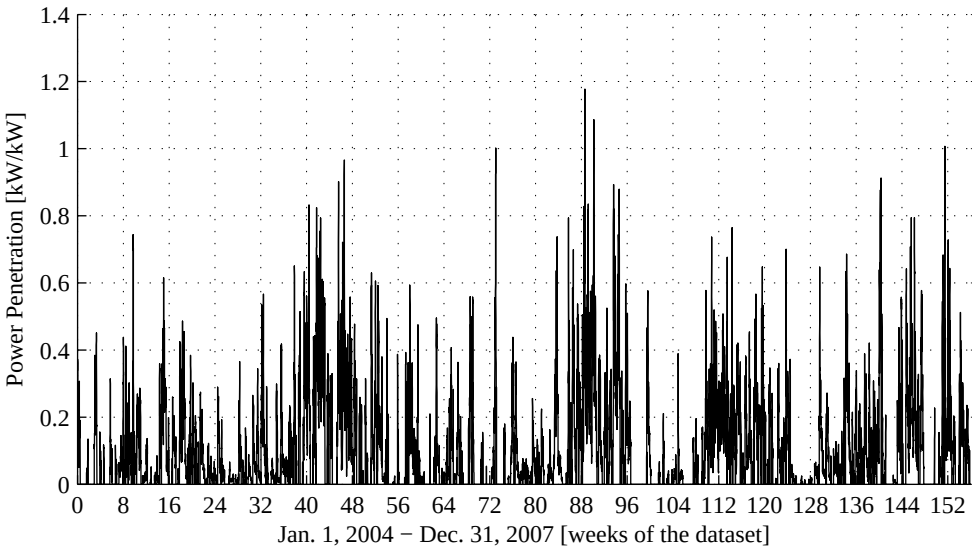


Figure 15: Time series of instantaneous penetration.

Table 3: Grid penetration classes adapted from [22]

| Class | Peak Instantaneous | Annual Average |
|---|---|---|
| Low | <50 % | <50 % |
| Medium | 50%-100% | 20%-50% |
| High | 100%-400% | 50%-150% |

excess wave power exists to ensure a sufficient load on the diesel generators. The following St. George system design options could be investigated to maintain diesel loading:

1. A seasonal specific WEC control strategy be adopted. For example, adjustments to the WEC generator intensity could be made to 'de-tune' the system to mitigate the high power penetration levels.
2. An electrical storage element could be introduced to store excess WEC power during periods of high power penetration.
3. An electrical 'dump load' could be introduced that dissipates excess WEC power, such as the resistive heating of water for residential or municipal buildings.

## 7. Approximate energy and fuel savings

To approximate the energy and fuel savings possible, a simplified analysis of the WEC power capture and community load is performed. Under the assumption that all wave power is utilized to offset diesel generator output, the time series of both wave power and electrical demand are summed. Using the total energy demanded (Eqs. (26-27)) and captured along with the stated diesel generator efficiency, the approximate volume of fuel savings is calculated. The results are summarized in Table 4.

$$E_{dem} = \sum_{t=0}^{26280} P_{dem}(t)\Delta t \tag{26}$$

$$E_{wec} = \sum_{t=0}^{26280} P_{wec}(t)\Delta t \tag{27}$$

In reality, all wave power could not be utilized to offset diesel generator output because there

Table 4: Energy and Fuel Savings Results

| | Units | Total(3yr) | Per year |
|---|---|---|---|
| Hours | hr | 26280 | 8760 |
| Years | yr | 3.00 | 1 |
| Demanded Energy | MWh | 4130 | 1380 |
| Wave Energy | MWh | 367 | 122 |
| Energy Penetration | % | 9% | 9% |
| Fuel Volume burned if all Diesel | L | 2.09E+06 | 6.95E+05 |
| Fuel Volume with Wave-Diesel | L | 1.90E+06 | 6.33E+05 |
| Fuel Savings | L | 1.85E+05 | 6.18E+04 |
| Fuel Cost Savings | $US | $245,000 | $81,600 |

are minimum load requirements and maximum ramp rates of the diesel generation system that need consideration. Therefore, to improve the accuracy of the energy and fuel savings estimates of Table 4, a time simulation of the integrated wave-diesel generation system would be required. This would enable the application of a detailed, time varying, power management strategy.

## Conclusions

The wave energy integration study for St. George Island, Alaska provides a number of interesting and useful results. A wave resource assessment indicates an average wave power per meter wave front of 28 kW/m, taking into account directional screening due to the proposed location of the deployment with respect to the island. The performance of a 100kW capacity WEC device has been estimated at the site. The mean WEC power output is 13kW average and could provide 9% of the island electrical energy demand. The calculation of grid penetration levels has enabled an assessment of the technical feasibility of interconnection to the existing electrical infrastructure. According to precedents set by the established wind-diesel hybridization field, this integration scenario could be classified as low to medium penetration, whereby relatively simple control systems could facilitate integration of wave energy converters to the diesel generation system. In order to evaluate power management strategies and economics in detail, further work involving a time simulation of the proposed wave-diesel electrical system is planned.

## Acknowledgments

This project was funded in part by SyncWave Energy Inc. and the Natural Sciences and Engineering Research Council (NSERC) of Canada. The contribution of Michael Tarbotten of Triton Consulting is gratefully acknowledged. Special thanks are given to Mr. Max Malavansky and Mr. Alvin Merculief on St. George Island for all of their cooperation in providing useful information. It is hoped that this study can be expanded into further collaboration and that wave power will be used on St.George Island in the future.

## References

[1] A. Babarit, H. Ben Ahmed, A. Clément, V. Debusschere, G. Duclos, B. Multon, G. Robin, Simulation of electricity supply of an atlantic island by offshore wind turbines and wave energy converters associated with a medium scale local energy storage, Renewable Energy 31 (2) (2006) 153–160.

[2] L. A. St.Germain, A Case Study of Wave Power Integration into the Ucluelet Area Electrical Grid, Master's thesis, University of Victoria (2005).

[3] D. Dunnett, J. S. Wallace, Electricity generation from wave power in canada, Renewable Energy (2008),In Press.

[4] S. Singal, Varun, R. Singh, Rural electrification of a remote island by renewable energy sources, Renewable Energy 32 (15) (2007) 2491–2501.

[5] G. Dalton, D. Lockington, T. Baldock, Case study feasibility analysis of renewable energy supply options for small to medium-sized tourist accommodations, Renewable Energy In Press (2008) –.

[6] S. J. Beatty, B. Buckham, P. Wild, Frequency response tuning for a two-body heaving wave energy converter, in: Proceedings of the International Society of Offshore and Polar Engineers, ISOPE 2008, Vancouver Canada, 2008.

[7] NOAA–WaveWatchIII, http://polar.ncep.noaa.gov/waves/index2.shtml, Accessed May 5th, 2008.

[8] Alvin Merculief, Mayor, City of St. George, Alaska, Personal Communication (December 2007).

[9] National Oceanic, Atmospheric Administration, St. George Island, Nautical Chart 16381, http://www.charts.noaa.gov/OnLineViewer/16381.shtml (April 2006).

[10] M. Tucker, E. Pitt, Waves in ocean engineering, 1st Edition, Vol. 5 of Elsevier ocean engineering book series, Elsevier, Amsterdam, New York, 2001.

[11] A. Cornett, Inventory of canada's marine renewable energy resources, Tech. Rep. CHC-TR-041, National Research Council - Canadian Hydraulics Centre, Ottawa, K1A 0R6, Canada (April 2006).

[12] N. Protter, S. J. Beatty, B. J. Buckham, PCT Patent No. WO 2007/137426 A1 - Wave Energy Converter, World Intellectual Property Organization (December 2007).

[13] S. J. Beatty, B. Buckham, P. Wild, Modeling, design and testing of a two-body heaving wave energy converter, in: Proceedings of the International Society of Offshore and Polar Engineers, ISOPE 2007, Lisbon Portugal, 2007.

[14] J. Falnes, Ocean Waves and Oscillating Systems: Linear Interactions including Wave Energy Extraction, Cambridge University Press, 2002.

[15] G. Clauss, E. Lehmann, C. Ostergaard, Offshore Structures - Conceptual design and hydromechanics, Vol. 1, Springer-Verlag, 1992.

[16] C. Gilloteaux, Babarit, Influence of wave spectrum spreading on the production of the searev wave energy converter., in: Proceedings of the Sixteenth (2007) International Offshore and Polar Engineering Conference, Lisbon, Portugal, July 1-6, 2007, ISOPE, 2007.

[17] G. Duclos, A. Babarit, A. H. Clement, Optimizing the power take off of a wave energy converter with regard to the wave climate, Transactions of the ASME. Journal of Offshore Mechanics and Arctic Engineering 128 (1) (2006) 56–64.

[18] L. Holthuijsen, Waves in Oceanic and Coastal Waters, Cambridge University Press, 2007.

[19] M. Devine, E. Baring-Gould, The Alaska Village Electric Load Calculator, Tech. Rep. NREL/TP-500-36824, U.S. Department of Energy, National Renewable Energy Laboratory, Golden, Colorado, http://www.nrel.gov/docs/fy05osti/36824.pdf (October 2004).

[20] State of Alaska, Commerce Community and Economic Development, Division of Community and Regional Affairs, Community Database Online, http://www.dced.state.ak.us/dca/commdb/CF_COMDB.htm, Accessed September 2008.

[21] D. Weisser, R. S. Garcia, Instantaneous wind energy penetration in isolated electricity grids: concepts and review, Renewable Energy 30 (8) (2005) 1299–1308.

[22] E. I. Baring-Gould, L. Flowers, P. Lundsager, Worldwide Status of Wind-Diesel Applications, in: DOE/AWEA/CanWEA Wind-Diesel Workshop, 2002, http://www.eere.energy.gov/windandhydro/windpoweringamerica/pdfs/workshops/2004_wind_diesel/101_status.pdf.